NACA TN 3507

NATIONAL ADVISORY COMMITTEE FOR AERONAUTICS

TECHNICAL NOTE 3507

PRACTICAL CONSIDERATIONS IN SPECIFIC APPLICATIONS OF GAS-FLOW INTERFEROMETRY

By Walton L. Howes and Donald R. Buchele

Lewis Flight Propulsion Laboratory
Cleveland, Ohio

Washington
July 1955

TABLE OF CONTENTS

Page

NATIONAL ADVISORY COMMITTEE FOR AERONAUTICS

TECHNICAL NOTE 3507

PRACTICAL CONSIDERATIONS IN SPECIFIC APPLICATIONS OF GAS-FLOW INTERFEROMETRY

By Walton L. Howes and Donald R. Buchele

SUMMARY

Optical refraction, end and corner effects, and spurious interferences may significantly affect interferometric evaluation of gas-density fields. Evaluation equations which account for refraction are derived in a previous report. In the present report these equations are extended to simultaneously include corner effects. The spurious interferences can be used to aline a model with the light beam. A simple method for evaluating the density adjacent to a surface is described.

The random error in measuring fringe shifts is a function of fringe spacing. In a representative experiment this random error was found to be less than the fringe-spacing variation produced by free-stream turbulence and optical imperfections. The latter variation was considerably less than the fringe shifts caused by steady-state density variations associated with boundary layers.

Recomputed laminar-boundary-layer density and velocity profiles associated with supersonic flow along an insulated flat plate are in fairly good agreement with the theory of Chapman and Rubesin. Computed skin-friction coefficients are in fair agreement with theory. The residual disagreement between theory and experiment is attributed to thickening of the boundary layer in the vicinity of the plate midspan plane. Temperature variations within the windows may also be significant.

Interferometric determinations of the density at the wall of a flat plate in subsonic flow are in very good agreement with results given by other methods.

Interferometric determinations of free-convection temperature profiles beneath a heated horizontal cylinder are in very good agreement with the theory of Hermann when the kinematic viscosity of air is based on the cylinder wall temperature, and refraction and corner effects are

accounted for. Agreement is poor, especially for large temperature differences, when the kinematic viscosity is based upon ambient temperature.

According to the experimental results, refraction is generally significant in boundary-layer studies. Corner effects are likely to be important when the model is not bounded by windows, but unimportant when the model is bounded. In determining the free-stream density in a wind tunnel, end effects are usually significant.

In three typical experiments the applicability, apparent-ray-trace crossing, and source-size criteria specified in a previous report were found to be satisfied. Series remainders were generally negligible.

INTRODUCTION

Density evaluation equations for use with optical interferograms of one-dimensional density fields are derived in reference 1. These equations account for optical refraction. However, certain additional sources of error are of interest. The most significant additional sources of error are likely to be

(1) End and corner effects

(2) Measurement of interference-fringe shifts

(3) Model alinement

(4) Spurious fringe shifts in the vicinity of surfaces

(5) Turbulence

All are considered in the present report.

Refraction corrections are described in references 1 to 3. Corrections for end or corner effects are reported in references 4 to 9. However, optical refraction and corner effects have not been analyzed simultaneously, although the two effects are interdependent. In the present report the evaluation equations reported in reference 1 are extended to include simultaneous corrections for corner effects.

In certain instances, the usefulness of interferometry may depend upon the accuracy of interference-fringe-shift measurements. Therefore, the results of an investigation of the random errors in measuring fringe shifts are included in the present report.

In addition, spurious fringe shifts may introduce significant errors in evaluating the density immediately adjacent to a surface. Sources and uses of the spurious fringe shifts are considered. A technique not involving spurious interferences is described for evaluating the density adjacent to a surface. The effect of turbulence is noted.

The significance of the preceding items, as well as other considerations indicated in reference 1, is determined for three representative experimental studies, namely,

(1) The laminar boundary layer associated with supersonic air flow along an insulated flat plate

(2) The boundary-layer density distribution associated with subsonic air flow along a thick flat plate with a blunt leading edge

(3) The temperature distribution associated with free-convective heat transfer from a horizontal cylinder

MEASUREMENT OF FRINGE SHIFTS

Suppose that in a given experiment the density field recorded as an optical interferogram consists of an ambient region having constant density ρ_∞ and a second region in which the density ρ is a function of a single Cartesian coordinate y (and time) which is essentially perpendicular to the path of the interferometer light beam. The interference fringes are, then, usually initially oriented

(1) Parallel to the gradient of ρ

(2) Perpendicular to the gradient of ρ

or

(3) For the infinite-fringe condition

Orientations 1 and 2 are illustrated in figures 1(a) and (b), respectively. Orientation 3 corresponds to constant phase of interference.

The fringe pattern associated with the field $\rho(y)$ differs from that which would exist if $\rho(y)$ were replaced by ρ_∞ (compare corresponding "flow" and "no flow" patterns in fig. 1). At any point on the interferogram the change of phase and order of interference corresponding to the change ρ_∞ to $\rho(y)$ is called the fringe shift at

that point. Thus, fringe shifts, henceforth denoted by N, are expressed in units of fringes, where a unit fringe shift corresponds to a change of 1 order of interference. (All symbols are defined in appendix A.)

Expressions for computing the fringe shifts from measurements of lengths on an interferogram are as follows:

(1) Orientation parallel to gradient of ρ - At a given value of y' (where primed quantities, henceforth, refer to lengths on the interferogram and, thus, take into account magnification),

$$|N| = n + \frac{|x' - x'_0|}{\bar{d}'_\infty} \qquad \left(\begin{array}{l} 0 < |x' - x'_0| < \bar{d}'_\infty \\ n = 0, 1, 2, \ldots \\ n < |N| \end{array} \right)$$

where $x' - x'_0$ (in the image plane) is the displacement in the x' direction of a fringe with respect to the position x'_0 of a given fringe for ambient conditions, and $\bar{d}'_\infty$ is the mean fringe pitch associated with the field ρ_∞. A simple accurate method for determining any value of N is suggested by the preceding formula and will be described subsequently. The random error ΔN in N is given by

$$\left(\frac{\Delta N}{N}\right)^2 = \left[1 + \left(\frac{1 - n}{N}\right)^2\right]\left(\frac{\Delta d'_\infty}{\bar{d}'_\infty}\right)^2 \qquad (N \neq 0)$$

where $\Delta d'_\infty$ is the random error in a single measurement of d'_∞.

(2) Orientation perpendicular to gradient of ρ - At a given value of y',

$$|N| = n - \frac{1}{\bar{d}'_\infty} \sum_{\nu=1}^{n} d'_\nu \qquad (\nu = 1, 2, 3, \ldots, n)$$

where the d'_ν are associated with the field $\rho(y)$ and are summed starting from the value of y at which $\rho(y) = \rho_\infty$. The quantities d'_ν and d'_∞ may represent either fringe pitch or semipitch. Only values d'_ν, $d'_\infty = \frac{1}{2}, 1, 1\frac{1}{2}, \ldots$ are included, because only interference maximums and minimums can be determined reliably by visual observation. The random error in N is given by

$$\left(\frac{\Delta N}{N}\right)^2 = \left(1 - \frac{n}{|N|}\right)^2 \left[\left(\frac{\Delta d'_\infty}{\overline{d}'_\infty}\right)^2 + \left(\frac{\Delta d'_\infty + \Delta d'_n}{2\sum_{\nu=1}^{n} d'_\nu}\right)^2\right] \qquad (N \neq 0)$$

(3) Infinite-fringe adjustment - At a given value of y',

$$|N| = n$$

where $n = \frac{1}{2}, 1, 1\frac{1}{2}, \ldots$. The random error in N is given by

$$\left(\frac{\Delta N}{N}\right)^2 \approx \left(\frac{1}{8N}\right)^2 + \left(\frac{\Delta d'_n}{2\sum_{\nu=1}^{n} d'_\nu}\right)^2 \qquad (N \neq 0)$$

where the error of estimating the phase of the infinite fringe associated with ρ_∞ is estimated to be about 1/8 fringe, and $\Delta d'_n$ corresponds to the value of $\Delta d'_\infty$ when $d'_n = \overline{d}'_\infty$.

The question arises as to which initial fringe adjustment is most desirable. Initial orientation parallel to the gradient of ρ appears to be preferable for the following reasons:

(1) Accurately measurable values of N are not limited to specific values $d' = \frac{1}{2}, 1, 1\frac{1}{2}, \ldots$. This reason can be applied to fringes & grad. also.

(2) It follows from reason 1 that $\rho(y)$ can be determined relatively accurately even if the maximum absolute value of N amounts to less than 1 fringe. (1) and (2) are the same reason.

(3) The possibility of confusing an interference fringe adjacent to a surface with the surface itself is reduced.

(4) The possibility of confusing interference fringes adjacent to a surface with diffraction fringes parallel to the surface is reduced.

Advantage 1 applies specifically to visual measurements on an interferogram. Photoelectric measurements on an interferogram also allow determination of intermediate values of N for the other orientations. However, accurate photoelectric measurements require extremely precise photographic technique because photographic exposure is a nonlinear function of the phase of interference, and photographic density is generally a nonlinear function of photographic exposure.

(5) determination of the boundary between free stream and the boundary layer can be determined more (probably) accurately with this orientation

For initial orientation parallel to the gradient of ρ, the profiles of adjacent fringes are identical. Thus, for each selected value of y' the shift $x' - x'_0$ of a given fringe from its ambient position is measured. The fringe shift is computed from the formula previously given, where $n = 0$. However, when $x' - x'_0$ attains a value such that $\left|x' - x'_0\right| \geq \overline{d}'_\infty$, the x' traverse of the comparator is returned (holding y' fixed) to the adjacent fringe, which has shifted to the vicinity of x'_0. Measurements of $x' - x'_0$ for selected values of y' are made on this new fringe and N is computed with $n = 1$. When again $\left|x' - x'_0\right| \geq \overline{d}'_\infty$ for this fringe, the next adjacent fringe is selected for measurement and N is computed with $n = 2$. The process can be repeated for any number of fringe shifts. The measured quantities are illustrated in figure 1(a). The process is extremely simple, and accurate measurements of arbitrary values of N are obtainable. All measurements are performed between the extensions of two adjacent ambient fringes. Thus, a fairly large x component of grad ρ can be tolerated. Intolerable values of the x component of grad ρ cause discontinuities of the measured fringe-shift profile at integer values of N. In such cases it would be necessary to revert to the method of measurement described in reference 10.

RANDOM ERRORS IN DETERMINING FRINGE SHIFTS AND FRINGE-SHIFT DERIVATIVES

The importance of random errors in measuring fringe shifts is discussed in reference 11. The probable error in measuring fringe shifts was assumed to be 1 fringe ($\Delta N = \pm 1$). The minimum required total fringe shift for accurate determination of a variable density field was estimated to be at least 10 fringes ($N = \pm 10$). However, more recent advances cause the assumed random errors and conclusions reached in reference 11 to appear extremely conservative. For example, the relative error in experimentally measuring N is reported to be ± 0.07 in reference 8 and, from the data given, is about ± 0.04 to ± 0.09 in reference 12. Consequently, the minimum required total fringe shift is considerably less than 10 fringes, and the range of Mach numbers (in the case of flow phenomena) for which the interferometric method is useful is probably considerably greater than the range 0.5 to 3.0 predicted in reference 11.

The error in N is often regarded as the largest random error in gas-flow interferometry. Moreover, according to the methods described in references 1 and 2, measurements of slopes dN/dy_D of the measured fringe-shift profile may also be desirable. It becomes important to determine what the random errors in measuring N and dN/dy_D actually are.

Error in N

The random error in N associated with steady-state measurements of boundary layers and similar phenomena is composed of two types of error, namely,

(1) The random error involved in measuring N

(2) The random error caused by fluctuations of the phenomenon about the steady state

The error in measuring N by visual methods depends upon several factors, among which are

(1) The value of d'_∞ (undisturbed fringe spacing)

(2) The distribution $\rho(y)$

(3) The initial fringe orientation with respect to the gradient of ρ

(4) The photographic properties of the interference-recording medium, for example, contrast, density, resolution, graininess

(5) The magnifying power of the instrument used for viewing the interferograms

The effect of d'_∞ is considered in the following paragraphs. The effect of initial fringe orientation is presented in the preceding section. Items 2, 4, and 5 are discussed in appendix B.

Consider two adjacent parallel interference fringes having a center-to-center separation (pitch) d'_∞. Then, the relative error in a single measurement of N_∞ due to an error $\Delta d'_\infty$ in measuring d'_∞ is given by

$$\Delta N_\infty = \frac{\Delta d'_\infty}{\overline{d}'_\infty}$$

where, as before, $\Delta d'_\infty$ represents the random error in a single measurement of d'_∞, $\overline{d}'_\infty$ represents the mean value of several measurements of d'_∞, and $|N_\infty| = 1$.

The standard deviation in measuring N_∞ was determined from a series of 19 interferograms possessing various values of d'_∞ by means of a commercial optical comparator having the following characteristics:

(1) Readability: 0.001 millimeter (0.00004 in.)

(2) Magnifying power: X22.6

(3) Illumination: Diffused

All measurements were made at one location on each interferogram in order to avoid the random error associated with spatial variation of d'_∞. Additional details are given in appendix B.

The results of determining $\Delta d'_\infty$ and ΔN_∞ as functions of $\bar{d}'_\infty$ are shown in figures 2(a) and (b), respectively. The limiting profile $(\Delta N_\infty)_{min}$ as a function of $\bar{d}'_\infty$, corresponding to the readability of the comparator, is also shown in figure 2(b). The measurements of $\Delta d'$ are represented by the straight lines

$$\Delta d'_\infty \approx 0.003 \text{ mm} \qquad (\bar{d}'_\infty < 1.4 \text{ mm})$$

$$\Delta d'_\infty \approx 0.005 \bar{d}'_\infty \text{ mm} \qquad (\bar{d}'_\infty > 1.4 \text{ mm})$$

so that

$$\Delta N_\infty \approx 0.003/\bar{d}'_\infty \qquad (\bar{d}'_\infty < 1.4 \text{ mm})$$

$$\Delta N_\infty \approx 0.005 \qquad (\bar{d}'_\infty > 1.4 \text{ mm})$$

where $\Delta d'_\infty$ and $\bar{d}'_\infty$ are in millimeters. The pair of profiles associated with each of the above sets of formulas do not coincide at $\bar{d}'_\infty = 1.4$ millimeters. This lack of coincidence is of minor importance, however, because only orders of magnitude are of interest. The minimum value $\Delta N_\infty \approx 0.005$ is 1/200 of the value assumed in reference 11 and about 1/10 of the values indicated in references 8 and 12. However, the values indicated in references 8 and 12 probably include all factors contributing to ΔN, except possibly time.

Because of the smallness of $\Delta d'_\infty$, it is quite likely that space and time variations in d'_∞ caused by turbulence and optical imperfections will be greater than $\Delta d'_\infty$ even over small regions of the field. Space variations of d'_∞ can be determined from a single interferogram. Time variations can be determined for corresponding points on a series of interferograms. Space variations of d'_∞ were determined from single measurements at several locations on a single interferogram. The space variations (standard deviations) associated with free-stream region in the subsonic-flow experiment to be discussed were

$$\Delta d'_{\infty} \approx 0.02 \text{ mm}$$

$$\Delta N_{\infty} \approx 0.01$$

for $\overline{d'_{\infty}} \approx 1.31$ millimeters and within a fixed interval of x'. The latter variations are two or three times greater than the corresponding deviations associated with the measurement process. However, the spatial variation $\Delta N_{\infty} \approx 0.01$ is only about 1 percent of the maximum fringe shift involved in the experiments. Time variations in N are discussed in conjunction with the subsonic-flow experiment later in the present report.

All results were obtained for $|N_{\infty}| = 1$. If the interval of measurement includes n constant pitch fringes, then the relative error in measuring nN_{∞} is inversely proportional to n, because the error is influenced only by the observer's ability to determine the locus of the interference maximums (or minimums) bounding the interval.

Error in dN/dy_D

The slope dN/dy_D of a measured fringe-shift profile N_D, as required by the evaluation procedure presented in reference 1, can be determined by several different methods. The error in determining the slope depends upon the error in the profile N_D as well as the error in measuring the slope. However, by assuming a known profile N_D, tests were made to determine the error in measuring the slope by means of an optical differentiator. The optical differentiator was selected because of its simplicity and the rapidity with which measurements can be performed.

A differentiator based on the principle of that described in reference 13 was constructed with provision for attachment to a drawing machine, thus permitting direct reading of slope angles ω in increments of 5 minutes of arc. Measurements of ω were made from a 7- by 10-inch plot of the profile N_D shown in figure 3(a). This profile was computed in reference 1 from a hypothetical exponential-density profile. The value of dN/dy_D associated with any given abscissa value y_D is given by

$$\frac{dN}{dy_D} = (\text{scale factor}) \tan \omega$$

Comparison of the hypothetical and measured profiles dN_D/dy_D is shown in figure 3(b). The standard deviation of a single measurement of ω

was found to vary from zero to about 10 minutes of arc, the larger error being associated with the greatest curvature of the profile N_D. For the range of values of dN/dy_D considered, the relative error in determining dN/dy_D was less than 10 percent, except when $|\omega|$ approached $\pi/2$, in which case small errors in measuring ω correspond to very large errors in $\tan \omega$.

Error in Density Profile

With some knowledge available regarding random errors in measuring N and dN/dy_D, the random errors in the density ratio ρ^* and distortion D, which determine the density profile $\rho(y)$, can be computed.

Evaluation equations for ρ^* and D are given in reference 1 and are repeated in appendix B. Expressions for the random errors in ρ^* and D also are given in appendix B, where it is shown that the error in measuring N is of prime importance in determining the error in ρ^* when $|N|$ is small but becomes much less significant as $|N|$ increases. Because the absolute magnitude of the refraction term, namely, $\frac{1}{6k\rho_\infty}(2 - 3K)b_1^2L^2$, is much less than that of the primary term $N\frac{\lambda}{k\rho_\infty L}$ in the equation for ρ^*, it follows that relatively large errors in dN/dy_D have only a small effect upon ρ^*. For example, if the refraction term amounts to 10 percent of the primary term, then an error of 10 percent in determining dN/dy_D amounts to an error of less than 2 percent in computing ρ^*. However, a 10-percent error in determining dN/dy_D yields a 10-percent error in computing D. Thus, it is desirable to keep D as small as possible. This can be accomplished by properly choosing the object plane, that is, the value of K. Generally, the previously described method for determining dN/dy_D is adequate.

The preceding paragraphs deal with the errors in evaluating the shape of a profile $\rho(y)$ without regard to its location with respect to material objects. Errors involved in locating the profile are somewhat different from those discussed previously and may best be considered in conjunction with specific experiments.

SURFACE EFFECTS AND MODEL ALINEMENT

Quite often the region immediately adjacent to a model surface is of prime interest in gas-flow experiments. Unfortunately, this region is likely to be the region in which experimental measurements of any

kind are most difficult. In the case of interferometry, the principal deleterious effects are misalinement of the model with respect to the light beam and spurious fringe shifts caused by surface reflections and diffraction.

Assume that the interferometer optical system is alined. Then spurious fringe shifts may be characterized by the angle φ which parallel ray traces make with respect to the surface of a model. The three basic ray-trace configurations with respect to a flat plate are illustrated in figure 4. The corresponding appearance of the surface of the plate for the three characteristic configurations utilizing first the test beam only, and then both beams, is shown in figures 5 and 6, respectively, for the condition of "no flow." Details of the observed fringe patterns are discussed in appendix C. In the presence of flow, as in a wind tunnel, observed spurious interferences would severely complicate the interpretation of the Zehnder-Mach fringes, which are of primary interest.

Although the complicated interferences near the plate surface may be regarded as spurious because they tend to obscure the Zehnder-Mach fringes, nevertheless, they may serve useful purposes, namely,

(1) Their existence provides a rapid and easy method for alining the light beam with the surface of the model.

(2) The reflection fringes might be used to evaluate density distributions in cooled boundary layers, that is, in situations where the light is refracted against the surface of the model.

Methods for alining a light beam with a flat surface are described in references 3, 7, and 14. Alternatively, the alinement can be accomplished by utilizing the spurious fringes, a simple magnifying lens, and a fine wire. As described in appendix C, the prominent surface phenomena are diagonal reflection fringes when $\varphi < 0$ (fig. 6(b)) and diagonal diffraction fringes when $\varphi > 0$ (fig. 6(d)). The two fringe patterns are inclined in opposite directions with respect to the surface of the plate. Alinement of the surface may be accomplished by allowing one end of the wire to touch the surface at the plate midspan plane. The image of the wire and the spurious interferences are observed by using the magnifier with the camera ground glass removed. The interferometer or the model is then rotated about the line formed by the intersection of the object plane and the model surface. Alinement of the plate is indicated by the "picket-fence" appearance of the spurious fringes at the surface (fig. 6(c)). Next, the ground glass is replaced. The fine wire may then be used for locating the ground glass at the desired image plane. Observing the point of wire contact with the plate surface also serves as a check upon the alinement procedure. The entire

procedure is simple, rapid, and possibly somewhat more accurate than the methods described in the references cited, although no data are available for comparing the methods. Residual misalinement resulting from application of the present method would definitely be well within the permissible misalinement limits set in reference 1. A similar alinement procedure may be utilized for any surface which can be made parallel to the light beam.

EVALUATION EQUATIONS FOR ONE-DIMENSIONAL DENSITY FIELDS, INCLUDING REFRACTION, END, AND CORNER CORRECTIONS

In practice it is unlikely that any gas density field will be truly one dimensional. For example, in a wind tunnel the condition of one dimensionality will be violated in the vicinity of the spanwise ends of a model and by boundary layers formed on the wind-tunnel windows. Similar violations of other basic geometries are likely. With regard to interferometry, the optical effects introduced by boundary layers on the windows and at the spanwise ends of the model will be called end effects and corner effects, respectively. The following specific definitions will be adopted:

(1) End effects - The optical effects caused by wind-tunnel-window boundary layers which are involved in determining the free-stream density ρ_∞

(2) Corner effects - The optical effects caused by boundary layers in the vicinity of the spanwise ends of a model which are involved in determining the basic variable density field associated with the assumed geometry ($\rho(y)$ in the present instance)

The model may, or may not, be contained within a wind tunnel. Thus, two cases of corner effects are of interest. If the model is contained within a wind tunnel, the model may, or may not, span the tunnel. If the model spans the tunnel, then the model and end-wall boundary layers will intersect. If the model does not span the tunnel, then the boundary layers may, or may not, intersect, depending upon how close the model is to the spanwise walls and other factors. In the present report the following two cases will be considered:

(1) The model is contained within a wind tunnel and spans the tunnel.

(2) The model is not contained within a wind tunnel.

In many instances evaluation equations which apply to the other situations can be readily obtained by modifying the derivations presented herein.

Consider a basic one-dimensional density field $\rho(y)$. Assume that end and corner effects correspond to minor deviations from the basic assumed geometry. Major deviations would correspond to a different basic geometry. Thus, it would then be appropriate to assume a different basic geometry. An equation for computing the free-stream density ρ_∞ in a wind tunnel and which includes end corrections is derived in appendix D. Evaluation equations for $\rho(y)$ are derived in appendixes E and F. These equations include corner corrections, as well as refraction corrections. The previously listed case 1 is considered in appendix E, whereas case 2 is treated in appendix F. In these two cases evaluation equations are developed by extending the analysis reported in reference 1 to include corner effects.

Free-Stream Density ρ_∞

By means of interferometry it is often possible to determine the free-stream density ρ_∞ within a wind tunnel from measurements performed outside the flow field. The appropriate experimental geometry consists of a wind tunnel of rectangular cross section bounded by windows at its spanwise ends, as shown in figure 7. Two adjacent spanwise reference holes are drilled through the spanwise walls or through a model which spans the tunnel. The hole denoted by r in figure 7 is connected to the external atmosphere, whereas the hole denoted by w is connected to the tunnel gas flow by means of a static tap. Appropriate values of pressure, temperature, and density within each region are noted in figure 7.

It is shown in appendix D that the free-stream density ρ_∞ is given by

$$\rho_\infty = \rho_r + N_{\infty,r}\left(\frac{\lambda}{kL_e}\right) - \frac{2}{n+1} N_{w,r}\left(\frac{\lambda\delta_z}{kLL_e}\right)$$

where the window boundary layers are assumed to be turbulent. The measurable fringe shifts $N_{\infty,r}$ and $N_{w,r}$ are associated with the density differences $\rho_\infty - \rho_r$, and $\rho_w - \rho_r$, respectively, where ρ_r is the density within hole r. The density ρ_w at a wind-tunnel, or model, wall which is parallel to the light path is also of interest and is given by

$$\rho_w = \rho_r + N_{w,r}\left(\frac{\lambda}{kL}\right)$$

Further details concerning appropriate experimental and calculation procedures are given in appendix D.

Density Field $\rho(y)$ (Model Spans Wind Tunnel)

Corner effects associated with a model contained within a wind tunnel are considered in references 6 to 8. The appropriate geometry consists of a wind tunnel of rectangular cross section bounded at its spanwise ends by plane windows. A model whose shape is independent of the spanwise coordinate z completely spans the tunnel. The density field adjacent to the model surface is effectively a function of a single coordinate perpendicular to the surface, except at the spanwise ends, where the model-wall and window boundary layers intersect. A typical ray trace through the test section and relevant geometrical quantities are shown in figure 8.

Evaluation equations corresponding to two particular assumed end-wall density distributions, namely,

(1) An effective-average density

(2) A power-law density distribution

are derived in appendix E. Evaluation equations associated with distribution 1 are useful when the exact end distribution is unknown. However, in wind tunnels the boundary layers on the wind-tunnel windows are usually turbulent at the test section. Then, the end-wall density distribution may be closely approximated by the power-law distribution 2.

The evaluation equations corresponding to the two assumed end density distributions are as follows:

Effective-average density:

One-term approximation: $\mu_\eta = b_0$

$$\rho^* = \frac{\rho_0}{\rho_\infty} = 1 + N \frac{\lambda}{k \rho_\infty L_E} - \left(\frac{\rho_\infty - \rho_{2,w}}{\rho_\infty} \right) \left(\frac{\delta_z - \zeta_1}{L_E} \right)$$

where

$$L_E = L - \frac{1}{2} (\zeta_1 + \zeta_2)$$

$$\zeta_1 = \zeta_2 = \frac{\delta_z}{\delta_y} y_0$$

$$y \equiv y_0 = y_D$$

Two-term approximation: $\mu_\eta = b_0 + b_1\eta$

$$\rho^* = 1 + N\frac{\lambda}{k\rho_\infty L_E} - \frac{1}{12}b_1^2\frac{L_R^2}{k\rho_\infty L_E}(4L_R - 6KL + 9\zeta_2) - \left(\frac{\rho_\infty - \rho_{2,w}}{\rho_\infty}\right)\left(\frac{\delta_z - \zeta_1}{L_E}\right)$$

where

$$L_E = L - \frac{1}{2}(\zeta_1 + \zeta_2)$$

$$L_R = L - (\zeta_1 + \zeta_2)$$

$$\zeta_1 = \frac{\delta_z}{\delta_y}y_0$$

$$\zeta_2 = \zeta_1 \pm \frac{1}{2}b_1L^2\frac{\delta_z}{\delta_y}$$

$$y \equiv y_0 = y_D - D$$

$$D = \pm\frac{1}{2}\left[(1 - 2K)L + \zeta_2 - \zeta_1\right]b_1L_R$$

$$b_1 = \left|\frac{dN}{dy_D}\right|\frac{\lambda}{L_E^{(2)}}$$

where

$$L_E^{(2)} = L - \zeta_1^{(2)}$$

$$\zeta_1^{(2)} = \frac{\delta_z}{\delta_y}y_D$$

The designation of one- and two-term approximations refers to the number of terms of the assumed series expansion for refractive index which are utilized (cf. ref. 1). The superscript (2) associated with L_E and ζ_1 indicates an approximation obtained by setting $\zeta_1 = \zeta_2$ in order to permit computation of the required quantities. Throughout the entire report the convention + or - is associated with $\mu(y)$ increasing or decreasing, respectively.

$\eta = y - y_0$

Power-law distribution:

One-term approximation: $\mu_\eta = b_0$

$$\rho^* = 1 + N\frac{\lambda}{k\rho_\infty L_R} - \frac{2}{L_R}\left(\frac{\rho_\infty - \rho_{2,w}}{\rho_\infty}\right)\left\{\left[1 + n\left(\frac{\zeta_1}{\delta_z}\right)^{\frac{n+1}{n}}\right]\frac{\delta_z}{n+1} - \zeta_1\right\}$$

where

$$L_R = L - (\zeta_1 + \zeta_2)$$

$$\zeta_1 = \zeta_2 = \frac{\delta_z}{\delta_y} y_0$$

$$y \equiv y_0 = y_D$$

Two-term approximation: $\mu_\eta = b_0 + b_1\eta$

$$\rho^* = 1 + N\frac{\lambda}{k\rho_\infty L_R} - \frac{1}{6} b_1^2 \frac{L_R}{k\rho_\infty}\left[2L_R + 3(\zeta_2 - KL)\right] -$$

$$\frac{2}{L_R}\left(\frac{\rho_\infty - \rho_{2,w}}{\rho_\infty}\right)\left(\left\{1 + \frac{n}{2}\left[\left(\frac{\zeta_1}{\delta_z}\right)^{\frac{n+1}{n}} + \left(\frac{\zeta_2}{\delta_z}\right)^{\frac{n+1}{n}}\right]\right\}\frac{\delta_z}{n+1} - \frac{(\zeta_1 + \zeta_2)}{2}\right)$$

where

$$L_R = L - (\zeta_1 + \zeta_2)$$

$$\zeta_1 = \frac{\delta_z}{\delta_y} y_0$$

$$\zeta_2 = \zeta_1 \pm \frac{1}{2} b_1 L^2 \frac{\delta_z}{\delta_y}$$

3378

$$y \equiv y_0 = y_D - D$$

$$D = \pm \frac{1}{2}\left[(1 - 2K)L + \zeta_2 - \zeta_1\right] b_1 L_R$$

$$b_1 = \left|\frac{dN}{dy_D}\right| \frac{\lambda}{L_R^{(2)}}$$

where

$$L_R^{(2)} = L - 2\zeta_1^{(2)}$$

$$\zeta_1^{(2)} = \frac{\delta_z}{\delta_y} y_D$$

The approximations indicated by the superscripts in parentheses are made for the same reason as in the preceding case. Calculation procedures for both cases are similar to that given in reference 1.

In order to include corner effects, additional quantities must be determined, namely, the window boundary-layer thickness δ_z and the relative density-difference $\frac{\rho_\infty - \rho_{2,w}}{\rho_\infty}$ across the window boundary layer. Usually the two quantities can be estimated or, if necessary, measured by some method other than interferometry.

The present evaluation equations are more cumbersome than the corresponding equations presented in reference 1. Thus, in order to minimize computation, it appears advisable to calculate first the extreme magnitudes of the corner-effect contributions associated with the individual terms by comparing them with the corresponding terms in the equations given in reference 1. Quite often, these contributions may be negligible compared with the primary and refraction effects and, therefore, can be neglected, thus reducing the calculation to that indicated in reference 1.

Density Field $\rho(y)$ (Model Not Contained within Wind Tunnel)

Corner effects associated with a model not contained within a wind tunnel are considered in references 4 and 5. The experimental geometry is similar to that for the preceding case except that the wind tunnel is absent. Again, the density field adjacent to the model is effectively a function of a single coordinate perpendicular to the surface, except at the spanwise ends. A typical ray trace through the test section and relevant geometrical quantities are illustrated in figure 9.

Evaluation equations associated with an effective-average end density distribution are derived in appendix F. The resulting evaluation equations are as follows:

Effective-average density:

One-term approximation:

$$\rho^* = \frac{\rho_0}{\rho_\infty} = 1 + N \frac{\lambda}{k\rho_\infty \bar{L}_E}$$

where

$$\bar{L}_E = \bar{L}_R + \frac{1}{2}(\bar{\zeta}_1 + \bar{\zeta}_2)$$

$$\bar{L}_R = L - 2(l_z - \delta_z)$$

$$\bar{\zeta}_1 = \bar{\zeta}_2 = l_z + \frac{a^2}{2(y_0 - \delta_y)}$$

$$y \equiv y_0 = y_D$$

Two-term approximation:

$$\rho^* = 1 + N \frac{\lambda}{k\rho_\infty \bar{L}_E} - \frac{1}{12} b_1^2 \frac{\bar{L}_R^2}{k\rho_\infty \bar{L}_E} \left\{ 4\bar{L}_R + 3\left[(1 - K)L - \bar{L}_e + \frac{1}{2}\bar{\zeta}_2\right]\right\}$$

where

$$\bar{L}_E = \bar{L}_R + \frac{1}{2}(\bar{\zeta}_1 + \bar{\zeta}_2)$$

$$\bar{L}_R = L - 2(l_z - \delta_z)$$

$$\bar{L}_e = L - l_z + \delta_z$$

$$\bar{\zeta}_1 = l_z + \frac{a^2}{2(y_0 - \delta_y)} \qquad \left(y_0 < \delta_y;\ \left|\frac{a^2}{2(y_0 - \delta_y)}\right| \leq l_z\right)$$

$$\bar{\zeta}_2 = l_z + \frac{a^2}{2(y_H - \delta_y)} \qquad \left(y_H < \delta_y;\ \left|\frac{a^2}{2(y_H - \delta_y)}\right| \leq l_z\right)$$

$$y_H = y_O + H$$

$$H = \pm \frac{1}{2} b_1 \bar{L}_R^2$$

$$y \equiv y_O = y_D - D$$

$$D = \pm \frac{1}{2}\left[\bar{L}_R - 2(KL + \delta_z - l_z)\right] b_1 \bar{L}_R$$

$$b_1 = \left|\frac{dN}{dy_D}\right| \frac{\lambda}{\bar{L}_E^{(2)}}$$

where

$$\bar{L}_E^{(2)} = \bar{L}_R + \bar{\zeta}_1^{(2)}$$

$$\bar{\zeta}_1^{(2)} = l_z + \frac{a^2}{2(y_D - \delta_y)} \qquad \left(y_D < \delta_y; \left|\frac{a^2}{2(y_D - \delta_y)}\right| \leq l_z\right)$$

$$y_O^{(2)} = y_D$$

Comments concerning the preceding case also apply in the present instance. The additional quantities which must be determined are δ_y, δ_z, l_z, and a. The model boundary-layer thickness δ_y can be measured directly from the interferogram. Often δ_z, l_z, and a can be measured from a supplementary interferogram obtained with the optical axis reoriented to be mutually perpendicular to the y-coordinate axis and the original optical axis. The quantities $\bar{\zeta}_1$ and $\bar{\zeta}_1^{(2)}$ may be computed or may be measured directly from the supplementary interferogram. Usually ρ_∞ corresponds to atmospheric density.

EXPERIMENTAL APPLICATIONS

Interferometer

Three Zehnder-Mach interferometers possessing 6-inch-diameter mirrors have been utilized at the NACA Lewis laboratory. The geometry of the latest design is shown in figure 10, and a photograph of the interferometer appears in figure 11. In all designs the mirror separation ratio in perpendicular arms is approximately 2:1, thus permitting reorientation of fringes without defocussing. Also, the commonly

practiced (refs. 15 to 17) but undesirable design characteristic, if aberrations are considered, involving passage of the test beam through the final splitter plate is avoided. Optical specifications of the latest model follow:

(1) Collimating lens: 30-Inch focal length, f/5 telescope objective

(2) Full-reflecting mirrors: 6-Inch diameter, 1-inch thick; aluminum-silicon monoxide coated; flat to 0.1λ sodium light (D line)

(3) Semireflecting mirrors: 6-Inch diameter, 3/4-inch thick; titanium dioxide coated; flat to 0.1λ sodium light (D line)

(4) Camera lens: Two of 20-inch focal length, f/4.5 Bausch and Lomb Tessars arranged face-to-face to form an afocal system producing unity magnification

The light-source unit provides for the use of incandescent, sodium, high-pressure mercury arc and magnesium spark light sources by the simple expedient of rotating a mirror inclined at 45° to the plane containing the light sources. The mercury arc lamp is equipped for steady or flash operation. The magnesium spark unit and power supply are very similar to those described in reference 18. The spark unit produces about six times the luminous intensity of the mercury flash in the same exposure time (approx. 14μsec). Sets of interference filters and apertures in sliding inserts are contained in the light-source - collimator unit. The maximum permissible test-section span is 18 inches. A sliding insert in the reference path permits rapid insertion or removal of wind-tunnel-window compensator plates or other desired devices. The camera shutter and, if desired, a knife-edge unit for schlieren photography are located at the afocal point of the camera-lens system. All shutter controls are operated from outside the camera box by means of extension levers. The camera ground glass and film holder are part of a standard 5-by-7 plate-back camera and are adjusted for focussing by means of the camera bellows. A 35-millimeter film-adapter unit is also available.

The afocal camera-lens system was selected to produce unity magnification of all object planes throughout the test-section span. Thus, no correction for image magnification is required. The actual measured magnification as a function of the object plane is listed in the following table, where the entire available test-section span is 18 inches:

Spanwise distance, in.	Magnification
4.5	0.9984
9.5	.9979
14.5	.9985

The interferometer light source and camera subassemblies are quickly removable and replaceable. The interferometer is supported by adjustable-height legs equipped with castered wheels; trunnions permit rotation of the instrument when supported by a yoke. The aforementioned accessories permit movement, installation, and adjustment of the instrument at a new facility all in one day. Moreover, a complete set of boundary-layer data (24 interferograms, four flow conditions) has been obtained in not much more time than that required to obtain the desired wind-tunnel conditions (about 2 hr).

A discussion of three typical experimental applications of gas-flow interferometry follows. Novel explanations for discrepancies between theory and experiment are proposed.

The applications are reported in the sequence in which the experiments were performed in order that successive improvements in technique might be noted.

Supersonic Air Flow Along a Flat Plate

Laminar-boundary-layer density profiles associated with supersonic air flow along an insulated flat plate and reported herein were calculated from data utilized in reference 10. The present density calculations differ from those reported in reference 10 in that the evaluation equations derived in reference 1 and in the present report are applied. Appropriate data for the present calculations were

Blue

$$L = 3.60 \text{ in.}$$

$$\lambda = 2.15 \times 10^{-5} \text{ in. (mercury green line)}$$

$$K = 1/2$$

$$k = 0.117 \text{ cu ft/slug}$$

$$M_\infty \approx 2.04$$

$$0.4 \times 10^6 < Re_x < 1.0 \times 10^6$$

$$x = 2.5 \text{ in.}$$

where M_∞ is the free-stream Mach number, and Re_x is the Reynolds number based on the distance x downstream of the leading edge of the plate.

Following estimation of corner effects, density profiles were computed according to the two-term equation presented in reference 1. The computed profiles are shown in figure 12(a) as a function of the dimensionless distance $\frac{y}{x}\sqrt{Re_x}$. The corresponding theoretical density profile, according to Chapman and Rubesin (ref. 19), is indicated for comparison with the experimental data. Velocity profiles u^* as a function of $\frac{y}{x}\sqrt{Re_x}$, where $u^* = \frac{u}{u_\infty}$, were calculated from the equation

$$u^* = \left\{ \frac{2}{(\gamma - 1)M_\infty^2} \left[T_t^* \left(1 + \frac{\gamma - 1}{2} M_\infty^2 \right) - \frac{1}{\rho^*} \right] \right\}^{1/2}$$

and are shown in figure 12(b) for comparison with the theoretical profile predicted in reference 19. The theoretical total-temperature ratio $T_t^* = T_t/(T_t)_\infty$ indicated in reference 19 was assumed for computing u^* from experimental data. Values of the section skin-friction coefficient C_x were calculated by numerical integration of the modified Kármán momentum equation

$$C_x = \frac{2}{x} \int_0^{\delta_y} \rho^* u^* (1 - u^*) \, dy$$

The computed coefficient C_x as a function of Re_x is shown in figure 12(c) for comparison with theoretically predicted results for laminar flow.

Density profiles were also computed according to the one- and three-term approximations derived in reference 1 and the present two-term approximation, which includes corner effects. The resulting density profiles for the largest Reynolds number are shown in figure 13 in order to illustrate the comparative importance of refraction and corner effects.

The recomputed density profiles shown in figure 12(a) exhibit a greater tendency to collapse into a single profile than do those shown in reference 10. Also, there is a general shift of the profiles so that the value of ρ^* associated with a given value of y is larger than was the case in reference 10. The experimental density and velocity profiles are very similar to those exhibited in reference 8. A systematic disagreement between theory and experiment is evident. The recomputed values of C_x are in better agreement with theory than the results presented in reference 10. The difference between experimental and theoretical values of C_x varies from 0 to 30 percent, with the greatest relative difference associated with the largest Reynolds number.

The maximum refraction correction varied from 4 percent (at $Re_x = 0.483 \times 10^6$) to 10 percent (at $Re_x = 0.989 \times 10^6$) of the relative maximum density difference $(\rho_w - \rho_\infty)/\rho_\infty$. The following additional items are important in determining the validity and error of the computed density profiles (cf. ref. 1):

(1) Applicability criterion: Determines when the two-term approximation equations are valid

(2) Apparent-ray-trace-crossing criterion: Specifies the condition for which the interferogram is free of superimposed imagery

(3) Light-source criterion: Specifies magnitude of misalinement or lateral extension of light source for which the assumption of an axial point source, hence the proposed evaluation equations, remains valid

(4) Series remainders: The errors in ρ^* and D resulting from termination of the series expansion for refractive index

(5) Corner effects

(6) Error in measuring fringe shifts and free-stream density ρ_∞

The computed extreme value associated with each of the preceding items was as follows:

(1) Applicability criterion:

$$-2 \times 10^4 \text{ in.}^{-2} < d^2N/dy_D^2 < 2 \times 10^4 \text{ in.}^{-2} \qquad \text{(criterion)}$$

$$-2 \times 10^4 \text{ in.}^{-2} < d^2N/dy_D^2 < 0 \qquad \text{(experiment)}$$

(2) Apparent-ray-trace-crossing criterion:

$$|dD/dy| < 1.0 \qquad \text{(criterion)}$$

$$|dD/dy| < 0.1 \qquad \text{(experiment)}$$

(3) Light-source criterion:

$$(q/f)^2 \ll 1.0 \qquad \text{(criterion)}$$

$$(q/f)^2 < 4 \times 10^{-9} \qquad \text{(experiment)}$$

$$(p/f)^2 \ll 1.0 \qquad \text{(criterion)}$$

$$(p/f)^2 < 10^{-4} \qquad \text{(experiment)}$$

(Quantities p and q are lateral coordinates of points in the plane of the light source. Coordinate p corresponds to x, and q corresponds to y. The origin $(p,q) \equiv (0,0)$ lies on the optical, or z-, axis.)

(4) Series remainders: Corresponding to the two-term approximation,

$$\left|R_2(\rho^*)\right| \leq 0.002$$

$$\left|R_2(D)\right| \leq 2\times10^{-5} \text{ in.}$$

(5) Corner effects: The errors introduced by neglecting corner effects were found to be

$$\Delta\rho^* < 0.01$$

$$\Delta D < 0.0001 \text{ in.}$$

(6) Error in measuring N and ρ_∞: For the interferograms presented in reference 10, $\bar{d}'_\infty \approx 0.01$ inch. The fringe shifts were carefully measured. Therefore, by assuming that the data in figure 2(b) apply and by utilizing the error expression for orientation parallel to grad ρ, it is estimated that $\left|\Delta N/N\right| \approx 0.02$ in the region (adjacent to free stream) associated with the greatest disagreement between theory and experiment. In the indicated region, $N \approx -0.5$. Thus, the standard deviation of ρ^* caused by the error in measuring N was $\Delta\rho^* \approx 0.001$. The error in measuring ρ_∞ is unknown.

All criteria were satisfied. In fact, it is quite unlikely that the light-source criterion would ever be violated unintentionally. The values given for the series remainders are much less than the values originally computed according to the remainder formulas given in reference 20. The corner effect and random error in ρ^* caused by the error in measuring N were negligible.

The preceding errors are insufficient to account for the systematic disagreement between theory and experiment, especially in the region adjacent to the free stream where refraction corrections are negligible. Remaining sources of possible significant errors are

(1) Error in measuring free-stream density ρ_∞

(2) Flow transition

(3) Transverse contamination

(4) Incorrect assumptions regarding the boundary-layer geometry

(5) Nonuniform heating of the wind-tunnel windows

(1) The disagreement between theory and experiment indicated in figure 12(a) is systematic. The error in measuring ρ_∞ is likely to be random. A systematic error in ρ_∞ corresponds to flapping the profile about the ordinate value $\rho^* = 1$ with the profile at $y = y_\infty$ held fixed and the end of the profile at $y = 0$ free. Agreement between theory and experiment is not attainable by this procedure.

(2) The disagreement with theory is not confined to the present results. A similar disagreement is apparent in the results of interference measurements presented in references 3 and 8. Although the measured density profiles exhibit certain characteristics associated with transition, in that they fall between theoretical laminar and turbulent profiles, the profiles presented in references 3 and 8 tend toward agreement with laminar theory for increasing Reynolds number associated with increasing x. This is contrary to expectations if transition were a factor. Moreover, in reference 8 shadowgraph photographs were used to confirm laminarity. Thus, flow transition is excluded as a cause of the systematic disagreement.

(3) Transverse contamination (refs. 21 and 8) in one sense, at least, does not appear to be the source of the error because the disagreement is similar both for transient (ref. 8) and steady-state (present report) experiments. For transient conditions the temperature in the corners is lower than that of the plate, whereas for steady-state conditions the corner temperature should be higher. Thus, the resulting density profiles should be somewhat different in the two cases. A similar conclusion is indicated in reference 8.

(4) Although the present corner-effect analysis is admittedly crude, it should permit calculation of the effect to, at least, the correct order of magnitude. The interaction of the plate and window boundary layers is not abrupt at right angles, as was assumed in the analysis; but, rather, a smooth fairing together of the boundary layers may be expected. However, if the boundary-layer cross-sectional shape is as shown in figure 14(a) or reference 22, then the resulting correction is opposite to that which would improve agreement between theory and experiment. If the cross-sectional geometry is as shown in figure 14(b), then the disagreement can be completely accounted for. Prevalent flat-plate laminar-boundary-layer theories (e.g., ref. 19) are based upon the assumption that the plate span is infinite. However, transverse bulging of boundary layers on the walls of supersonic wind tunnels has been found (ref. 23), and it appears not unlikely that similar effects may occur in the boundary layer on an interposed flat plate. Ultimately, the bulge, which apparently arises from transverse pressure gradients, might be expected to decay in the constant-area section downstream of the leading edge of the plate. Agreement between theory

and experiment tends to improve with increasing x (refs. 3 and 8) in concordance with this argument. The present results indicate improved agreement between theory and experiment with decreasing free-stream density at a fixed value of x, which corresponds to decreased bulging with decreasing density at fixed x. The effect is confirmed by probe measurements (ref. 10) at three spanwise positions.

(5) Finally, temperature variations throughout the wind-tunnel windows are accompanied by variations of window thickness and refractive index. Temperature variations may exist at the window surface adjacent to the flow, thus causing nonuniform heating of the windows. For example, measured surface-temperature differences of 2° C between adjacent regions of laminar and turbulent flow on a flat plate are reported in reference 8. Section surface-temperature differences on wind-tunnel windows are undoubtedly considerably less than 2° C because the boundary layer is then entirely turbulent. However, from a simplified analysis presented in appendix G, it is found that a transverse temperature variation of only 0.1° C would introduce an absolute error in ρ^* amounting to 0.005, which is on the verge of being appreciable. Further investigation of the magnitudes of such temperature variations is necessary before any definite conclusions regarding their importance can be reached. In any event, the resulting error can be minimized by choosing window glass having the minimum possible effective combination of coefficient of thermal expansion and temperature coefficient of refractive index and by keeping the ratio of window thickness to wind-tunnel span as small as is mechanically feasible. If necessary, a crude correction for the effect can be performed by obtaining an interferogram immediately following termination of flow. In experiments not reported herein the effect of nonuniform window heating has appeared as a false boundary layer following termination of flow.

Subsonic Air Flow Along a Thick Flat Plate with Blunt Leading Edge

Boundary-layer density profiles associated with subsonic air flow along a thick flat plate with blunt leading edge were determined by means of interferometry for comparison with similar profiles obtained by two other methods of measurement, namely, X-rays and a total-pressure probe (ref. 24). A sketch of the model is shown in figure 15. A complete description of the wind tunnel and model is given in reference 24. Data pertinent to the interference calculations were as follows:

$$L = 3.806 \text{ in.}$$

$$\lambda = 2.15 \times 10^{-5} \text{ in.}$$

$$K = 1/2$$

$$k = 0.117 \text{ cu ft/slug}$$

$$0.55 < M_\infty < 0.78$$

$$10^5 < Re_x < 5 \times 10^5$$

$$x = 2.74 \text{ in.}$$

Six interferograms were obtained for each of four Reynolds number - Mach number combinations. Typical interferograms obtained by using unfiltered and filtered mercury light (λ = 5461 Å) are shown in figures 16(a) and (b), respectively. Averaged density profiles for each of the four conditions are shown in figure 17 as functions of the dimensionless distance y/θ, where the momentum thicknesses θ were computed by numerical integration of the Kármán momentum equation. No attempt has been made to compare the experimental results with theory. However, for at least one flow condition ($Re_x = 0.443 \times 10^6$; $M_\infty = 0.55$) all six interferograms indicated densities in the boundary layer adjacent to the free stream which were slightly greater than ρ_∞. This might arise from the fact that the air flow made a 90° turn in proceeding from the plenum chamber to the test section. That such a condition may be possible is shown in reference 25.

In the present experiment the interferometer was used for determining the free-stream density ρ_∞ and the density ρ_w at the surface of the model, as well as the density field $\rho(y)$. Because the plate spanned the wind tunnel, it was possible to drill two 1/4-inch-diameter reference holes spanwise through the plate at the chordwise location (fig. 15) at which boundary-layer measurements were desired. Cross hairs were located within the holes at the wind-tunnel midspan plane, which was the selected object plane. The wall static hole w was connected to the tunnel air flow by means of a 0.005-inch-diameter hole which was drilled perpendicular to the plate surface near the midspan plane. The reference hole r was connected to the external atmosphere by means of a small hole which was drilled through one of the wind-tunnel windows. The procedure outlined earlier in the present report and detailed in appendix D was used for determining ρ_∞ and ρ_w.

The preceding technique possesses several desirable attributes, namely:

(1) The flow is completely undisturbed by measuring instruments.

(2) All aerodynamic pressure-measuring instrumentation can be eliminated.

(3) Additional required instrumentation consists only of a barometer, a thermometer, and a thermocouple for measuring the model temperature.

(4) The entire density field, including free-stream and model wall densities, is recorded instantaneously on a single photographic negative.

(5) Instantaneous density profiles based on simultaneous values of ρ_∞ are obtained.

(6) Because ρ_w is determined from the interference patterns appearing in the reference holes, the problem of spurious fringe shifts caused by the model surface is circumvented.

(7) Temperature gradients within the model are indicated by the interference patterns appearing in the reference holes. Suitable modifications of the basic technique can usually be made in order to account for such gradients.

Three different methods of determining the average wall-to-stream density ratio $\rho_w^* = \rho_w/\rho_\infty$ were compared. The ratio was determined from the interference data by means of the technique already described, from pressure measurements by using the equation

$$\rho_w^* = \frac{1}{1 + 0.2\eta M_\infty^2}$$

where the value of the temperature recovery factor η was assumed to be 0.88, and from the pressure and temperature measurements by using the equation

$$\rho_w^* = \frac{(T_t)_\infty}{T_w} \frac{1}{1 + 0.2M_\infty^2}$$

where $(T_t)_\infty$ was measured in the plenum chamber.

The averaged density ratios corresponding to each of the flow conditions are compared in the following table:

Condition	Re_x	M_∞	ρ_w^* from pressure probe	ρ_w^* from pressure and temperature probes	ρ_w^* from interferometer
1	0.179×10^6	0.72±0.04	0.916±0.011	0.923	0.915±0.016
2	.442	.783±.008	.902±.006	.905	.901±.007
3	.443	.550±.008	.949±.005	.953	.946±.003
4	.952	.782±.008	.902±.006	.906	.905±.002

The maximum disagreement between the values of ρ_w^* is 0.9 percent. Corresponding values of ρ_w^* obtained by the three methods agree to within the standard deviations of ρ_w^*. For the pressure measurements, the pressure fluctuations were of the order of ±0.05 inch mercury for conditions 2 and 3 and ±0.1 inch mercury for conditions 1 and 4. It was apparent from the observed interference patterns and the density profiles computed from them that variations of ρ_w^* resulted principally from flow fluctuations rather than inadequacies of the three methods for steady-state measurements.

The fringe pitch $\bar{d}'_\infty$ was necessarily varied from 0.235 millimeter (condition 1) to 1.45 millimeters (condition 4) in order to obtain the zero-order interference fringe in both holes simultaneously (cf. appendix D). The corresponding error ΔN_∞ varied from about 0.01 to 0.005, respectively. The values of ΔN_∞ are considerably less than that of ΔN, namely, $\Delta N \approx 0.04$ for all flow conditions, where ΔN represents the standard deviation associated with all interferograms corresponding to a given flow condition. The latter value includes the effect of the error (±0.0002 in.) in locating the model surface with respect to the interference pattern. Because ΔN was from four to eight times greater than ΔN_∞, it is concluded that the scatter of the fringe-shift profiles must have been caused primarily by mass-flow fluctuations. In the present instance only steady-state conditions were of interest. In the presence of the minor flow instabilities, steady-state conditions were approximated with sufficient accuracy by averaging six interferograms.

Extreme values associated with the various criteria and errors were as follows:

(1) Applicability criterion:

$$-2 \times 10^4 \text{ in.}^{-2} < d^2N/dy_D^2 < 2 \times 10^4 \text{ in.}^{-2} \qquad \text{(criterion)}$$

$$-0.5 \times 10^4 \text{ in.}^{-2} < d^2N/dy_D^2 < 0 \qquad \text{(experiment)}$$

(2) Apparent-ray-trace-crossing criterion:

$$|dD/dy| < 1.0 \qquad \text{(criterion)}$$

$$|dD/dy| < 0.007 \qquad \text{(experiment)}$$

(3) Series remainders: For the two-term approximation,

$$|R_2(\rho^*)| < 10^{-4}$$

$$|R_2(D)| < 0.0001 \text{ in.}$$

(4) Corner effects: The maximum errors introduced by neglecting corner effects were

$$\Delta\rho^* < 0.002$$

$$\Delta D \approx 0$$

All criteria, including the light-source criterion, were satisfied and the preceding errors were negligible. The maximum refraction correction varied from 1 percent (at $Re_x = 0.179 \times 10^6$) to 3 percent (at $Re_x = 0.952 \times 10^6$) of $(\rho_w - \rho_\infty)/\rho_\infty$. Side-wall boundary-layer density profiles were determined by means of a total-pressure probe and were found to satisfy a 1/9 power-law distribution. Thus, the evaluation equations associated with a power-law end-density distribution (n = 9) were used for computing the corner effects.

Free Convection of Air Around a Heated Horizontal Cylinder

Free convection of air around a horizontal circular cylinder has been investigated theoretically (ref. 26). Experimental measurements (refs. 26 and 5) have given good agreement with theory. Thus, the temperature profile beneath a cylinder can be regarded as known and can, therefore, be used for testing the analysis herein. The cylinder problem

(1) Serves as a test of the evaluation equations for a model not contained within a wind tunnel

(2) Permits comparison of results obtained by treating the temperature distribution as a one-dimensional distribution and as an axially symmetric distribution

(3) Permits comparison of the present experimental results with previous theoretical and experimental results

A Duralumin cylinder 3 inches in diameter and 10 inches long was utilized in the experiments. Further details of the cylinder construction and the experimental procedure are discussed in appendix H.

Sets of interferograms were obtained corresponding to the three optical orientations depicted in figure 18, namely,

(1) Light propagation parallel to the cylinder axis (one-dimensional distribution with corner effects)

(2) Light propagation perpendicular to the cylinder axis at the midlength plane (axially symmetric distribution)

(3) Light propagation perpendicular to the cylinder axis at an end plane (depicts corner distribution for computing corner corrections)

Typical interferograms characteristic of the three optical orientations are shown in figure 19. Orientation 1, shown in figure 19(a), permits evaluation of the vertical temperature distribution beneath the cylinder according to the procedure for a one-dimensional field associated with a model not contained within a wind tunnel. Orientation 2, shown in figure 19(b), permits evaluation of the same field according to the axially symmetric method. Orientation 3, shown in figure 19(c), provides information concerning the density distribution at the ends of the model.

Interferograms were obtained for several wall-to-ambient temperature differences Θ in the interval $24^\circ\ F < \Theta < 450^\circ\ F$ by using orientation 1 with $K = 1/2$ and $1/3$ and, also, by using orientation 2. According to the theory of Hermann (ref. 26) all temperature profiles which satisfy the conditions

$$10^4 < Gr < 10^9$$

$$\delta/r \ll 1$$

where Gr is the Grashof number, δ is the boundary-layer thickness, and r is the cylinder radius, should collapse into a single profile for any given azimuth angle when the dimensionless temperature ratio θ/Θ is plotted as a function of the dimensionless distance $\frac{y}{r}\left(\frac{Gr}{8}\right)^{1/4} g(x)$, where θ is the local-to-ambient temperature difference, and $g(x)$ is an azimuth function which possesses the value 0.760 beneath the cylinder. In the present experiments the quantities Gr and δ/r were found to satisfy the inequalities

$$7.4 \times 10^5 < Gr < 2.3 \times 10^7$$

when the kinematic viscosity ν was based on the cylinder wall temperature, and

$$0.25 < \delta/r < 0.30$$

Therefore, except for the fact that δ/r was comparatively large, the conditions of the experiment satisfied the requirements of the theory.

Dimensionless temperature profiles obtained for orientation 1 with $K = 1/2$ and computed according to the two-term approximation with corner corrections are compared in figure 20(a) with the theoretical profile predicted in reference 26. (Incidentally, the dimensionless coordinates of the theoretical profile are not given in ref. 26 but can be obtained from table I of ref. 27.) Profiles obtained for $K = 1/3$ and computed, first, according to the Wachtell-DeFrate method (refs. 2 and 3), which neglects corner effects, and then according to the present two-term approximation are compared with the theoretical profile in figures 20(b) and (c), respectively. Profiles obtained by using orientation 2 and computed according to Wachtell's simplification (ref. 28) of Von Voorhis' evaluation procedure (ref. 29) for axially symmetric distributions are compared in figure 20(d) with the theoretical profile.

The kinematic viscosity ν, which is required for computing the Grashof number, $Gr = \frac{r^3 g}{8\nu^2}(T_w^* - 1)$, where g is the gravitational acceleration and T_w^* is the wall-to-ambient temperature ratio, was in all cases based on the cylinder wall temperature T_w. The effect of basing ν on the ambient temperature T_∞, rather than T_w, is shown in figure 21.

Agreement between the experimental and theoretical temperature profiles is generally very good and somewhat better than that indicated in reference 5. This should be expected because, in the experiments reported in reference 5, δ/r was somewhat greater ($\delta/r \approx 0.5$) than in the present experiment and refraction was apparently neglected. In reference 5, the kinematic viscosity ν was based on $(T_w + T_\infty)/2$, which was assumed to be constant for all values of Θ. By comparing the temperature profiles in figures 20(a) and 21 with those in reference 5, it is apparent that basing ν on $(T_w + T_\infty)/2$ is not the cause of the discrepancy between theory and experiment which was obtained in reference 5.

The maximum refraction correction varied from 0.2 percent (for $\Theta = 24^\circ$) to 2 percent (for $\Theta = 450^\circ$) of $(\rho_w - \rho_\infty)/\rho_\infty$. The corresponding maximum corner corrections were found to vary from 0.8 percent (for $\Theta = 24^\circ$) to 8 percent (for $\Theta = 450^\circ$). Therefore, refraction and corner corrections were included in computing the temperature profiles.

Extreme values associated with the various criteria and remainders were as follows:

(1) Applicability criterion:

$$-0.8\times10^{4}\ \text{in.}^{-2} < d^2N/dy_D^2 < 0.8\times10^{4}\ \text{in.}^{-2} \qquad \text{(criterion)}$$

$$-1.2\times10^{4}\ \text{in.}^{-2} < d^2N/dy_D^2 < 0 \qquad \text{(experiment)}$$

for $K = 1/2$ and $\Theta = 450.1^{\circ}$ F;

$$-4\times10^{4}\ \text{in.}^{-2} < d^2N/dy_D^2 < 7\times10^{4}\ \text{in.}^{-2} \qquad \text{(criterion)}$$

$$-0.1\times10^{4}\ \text{in.}^{-2} < d^2N/dy_D^2 < 0 \qquad \text{(experiment)}$$

for $K = 1/3$ and $\Theta = 202.0^{\circ}$ F.

(2) Apparent-ray-trace-crossing criterion:

$$\left|dD/dy\right| < 1.0 \qquad \text{(criterion)}$$

$$\left|dD/dy\right| < 0.006 \qquad \text{(experiment)}$$

for $K = 1/2$ and $\Theta = 450.1^{\circ}$ F;

$$\left|dD/dy\right| < 1.0 \qquad \text{(criterion)}$$

$$\left|dD/dy\right| < 0.0006 \qquad \text{(experiment)}$$

for $K = 1/3$ and $\Theta = 202.0^{\circ}$ F.

(3) Series remainders: For the two-term approximation,

$$\left.\begin{aligned} R_2(\rho^*) &\leqq 0.008 \\ R_2(D) &\leqq 0.003\ \text{in.} \end{aligned}\right\} \quad \text{for } K = 1/2$$

$$\left.\begin{aligned} R_2(\rho^*) &\leqq 0.8\times10^{-4} \\ R_2(D) &\leqq 0.8\times10^{-4}\ \text{in.} \end{aligned}\right\} \quad \text{for } K = 1/3$$

The light-source criterion was easily satisfied. The applicability criterion was violated at the largest values of Θ for $K = 1/2$. The criterion, therefore, must be conservative, as was indicated in reference 1, because the corresponding temperature profiles in figures 20(a)

and (c) are all in good agreement with theory. The distortion remainder of 0.003 inch for $K = 1/2$ is only about 0.7 percent of the boundary-layer thickness and, of course, represents the maximum possible value attainable by $R_2(D)$.

CONCLUDING REMARKS

In the three experiments, the ratio of wind-tunnel-wall boundary-layer thickness to wind-tunnel span possessed the following maximum values:

Supersonic flow: $2\delta_z/L \approx 0.06$

Subsonic flow: $2\delta_z/L \approx 0.16$

Free convection: $2\delta_z/L \approx 0.025$

Corner effects were negligible in the supersonic- and subsonic-flow experiments but were quite large in the free-convection experiment, especially for large values of Θ. From these results, it is concluded that relatively thick wind-tunnel-wall boundary layers are likely to introduce negligible or small corner effects (although end effects are usually significant), whereas relatively thin end boundary layers are likely to introduce relatively large corner effects when the model is not contained in a wind tunnel. Therefore, the existence or nonexistence of windows bounding the model is far more important in determining the significance of corner effects than is the relative end-wall-boundary-layer thickness.

The applicability and especially the ray-crossing and light-source criteria were effectively satisfied in all three experiments. Only the distortion remainder in the free-convection experiment appeared to be a possible significant residual error among the systematic errors which were evaluated.

Knowledge of the random error ΔN_∞ as a function of $\bar{d}'_\infty$ (fig. 2(b)) should prove useful in determining the error in measuring time fluctuations of N in turbulence studies (refs. 6 and 30) because ΔN_∞ is exactly that error which would be of interest.

In reference 31 it is shown that the usefulness of interferometry in studies of cooled boundary layers is theoretically limited by refraction of light against the model surface. However, if the model surface is a reflecting surface, then light is reflected from the surface rather than absorbed by the surface as is assumed in reference 31. A typical interferogram shown in figure 22 and obtained by using the

hot-plate model described in reference 1 illustrates the reflection effect. At the cool surface (the lower surface in the interferogram) the interference fringes do not terminate but, rather, are continuous, appearing as reflection fringes below the surface. The surface is indicated, approximately, by the horizontal line passing through the vertices of the "parabolic" portion of the fringes. A method for evaluating the temperature distribution adjacent to the cool surface (in the example presented) might be developed by extending the analysis presented in reference 1 to include reflection and the phase shift accompanying reflection (ref. 32). Success of the method would obviate the difficulties described in reference 31. The method might also be applicable when the light is refracted away from the surface by employing an off-axis light source expressly for the purpose of obtaining reflection fringes. Consideration of off-axis light sources is included in the analysis contained in reference 1.

Although the interference method permits a vast amount of data to be obtained in a very short time, conversion of the data contained in the interferogram into numerical data is at present a time-consuming process. The usefulness of the interference method could probably be increased most significantly by the development of an automatic, or semiautomatic, instrument for converting the data contained in the interference pattern into numerical data.

Lewis Flight Propulsion Laboratory
National Advisory Committee for Aeronautics
Cleveland, Ohio, May 13, 1955

APPENDIX A

SYMBOLS

The following symbols are used in this report:

a perpendicular distance from outer hyperbolic-shaped extremity of corner boundary layer to intersection of hyperbola asymptotes (fig. 9)

b_0 value of refractive index associated with $\eta = 0$ and $y = y_0$ for any given ray trace

b_1 refractive-index gradient associated with $\eta = 0$ and $y = y_0$ for any given ray trace

b_ν refractive-index coefficient associated with $\eta = 0$ and $y = y_0$ for any given ray trace

C_x section skin-friction coefficient

c_σ light-path coefficients (ref. 1)

c_σ^* light-path coefficients (ref. 1)

$c_{\sigma,\nu}$ fringe-shift coefficients (ref. 1)

D optical distortion

d interference-fringe pitch

Gr Grashof number

H final refraction displacement perpendicular to z-axis and within density field $\rho(y)$

K fraction of test-section span, $K = 1 - \frac{z_R}{L}$

k specific refractivity

L model span

L_E effective model span in wind tunnel, $L_E = L - \frac{1}{2}(\zeta_1 + \zeta_2)$

$L_E^{(2)}$ approximation of L_E, $L_E^{(2)} = L - \zeta_1^{(2)}$

$\bar{L}_E$ effective span of model not contained in wind tunnel, $\bar{L}_E = \bar{L}_R + \frac{1}{2}(\bar{\zeta}_1 + \bar{\zeta}_2)$

$\bar{L}_E^{(2)}$ approximation of $\bar{L}_E$, $\bar{L}_E^{(2)} = \bar{L}_R + \bar{\zeta}_1^{(2)}$

L_e effective wind-tunnel span in determining end correction, $L_e = L - \frac{2}{n+1}\delta_z$

$\bar{L}_e$ effective span of model not contained in wind tunnel, $\bar{L}_e = L - l_z + \delta_z$

L_R reduced model span in wind tunnel, $L_R = L - (\zeta_1 + \zeta_2)$

$L_R^{(2)}$ approximation of L_R, $L_R^{(2)} = L - 2\zeta_1^{(2)}$

$\bar{L}_R$ reduced span of model not contained in wind tunnel, $\bar{L}_R = L - 2(l_z - \delta_z)$

l_z extent of corner boundary layer in z-direction

M Mach number

m lateral magnification

N interference-fringe shift in units of fringes

N_D observed interference-fringe-shift profile, $N_D = N_D(y_D)$

$N_{w,r}$ interference-fringe shift associated with density difference $\rho_w - \rho_r$

$N_{\infty,r}$ interference-fringe shift associated with density difference $\rho_\infty - \rho_r$

n integer

n exponent of power-law density distribution

p absolute pressure

R gas constant

R_2 remainder associated with power-series expansion of μ_η to two terms

Re_x	Reynolds number based on length x
s	physical length
T	static temperature
T_t	total temperature
t	window thickness
u	velocity
u^*	velocity ratio, $u^* = u/u_\infty$
x	coordinate perpendicular to optical axis
x_0	value of x associated with $\zeta \equiv z = 0$ for any given ray trace
y	coordinate perpendicular to optical axis
y_D	y-coordinate value of measured fringe shift
y_H	y-coordinate value of ray trace when $\eta = H$
y_0	y-coordinate value of ray trace when $\eta = 0$
$y_0^{(2)}$	approximation of y_0, $y_0^{(2)} = y_D$
z	coordinate parallel to optical axis
z_R	distance from origin of z to selected object plane
β	projected angle formed by ray trace and optical axis in yz-plane
β	temperature coefficient of refractive index
γ	ratio of specific heat at constant pressure to specific heat at constant volume
Δ	error
Δ	increment
δ	boundary-layer thickness
δ_y	boundary-layer thickness associated with density distribution $\rho = \rho(y)$

δ_z boundary-layer thickness associated with refractive index distribution μ_2

ζ ray-trace coordinate parallel to optical axis, $\zeta \equiv z$

ζ_1 assumed z component of ray trace in corner adjacent to initial boundary $z = 0$ (fig. 8) (model contained in wind tunnel)

$\zeta_1^{(2)}$ approximation of ζ_1, $\zeta_1^{(2)} = \frac{\delta_z}{\delta_y} y_D$

$\overline{\zeta}_1$ assumed z component of ray trace in corner adjacent to initial boundary $z = 0$ (fig. 9) (model not contained in wind tunnel),

$$\overline{\zeta}_1 = l_z + \frac{a^2}{2(y_0 - \delta_y)}$$

ζ_2 assumed z component of ray trace in corner adjacent to final boundary $z = L$ (fig. 8) (model contained in wind tunnel)

$\overline{\zeta}_2$ assumed z component of ray trace in corner adjacent to final boundary $z = L$ (fig. 9) (model not contained in wind tunnel),

$$\overline{\zeta}_2 = l_z + \frac{a^2}{2(y_H - \delta_y)}$$

η ray-trace coordinate parallel to y-coordinate, $\eta \equiv |y - y_0|$

Θ absolute temperature difference, $\Theta = T_w - T_\infty$

θ absolute temperature difference, $\theta = T - T_\infty$

λ wave length of light

μ refractive index

μ refractive-index distribution adjacent to model, $\mu = \mu(y)$

μ_g refractive index of wind-tunnel windows

μ_η refractive-index distribution adjacent to model as function of coordinate η

μ_0 value of refractive index associated with $\eta = 0$ and $y = y_0$ for any given ray trace

μ_2 refractive-index distribution adjacent to wind-tunnel windows, $\mu_2 = \mu_2(z)$

μ_3 refractive-index distribution in vicinity of corners of model, $\mu_3 = \mu_3(y,z)$

ν kinematic viscosity

ν integer

ξ ray-trace coordinate parallel to x-coordinate, $\xi \equiv |x - x_0|$

ρ density

ρ_0 value of density associated with $\eta = 0$ and $y = y_0$ for any given ray trace

ρ^* density ratio, $\rho^* = \rho_0/\rho_\infty$

ρ_w^* value of density ratio at model surface, $\rho_w^* = \rho_w/\rho_\infty$

σ integer

φ angle formed by ray trace and surface of flat plate

ψ optical-path length

Subscripts:

a atmosphere

n integer

r reference value within hole spanning wind tunnel and connected to external atmosphere

w model surface or wind-tunnel wall parallel to model surface

ν integer

σ integer

2,w wind-tunnel window surface

∞ ambient, or free-stream, value

Superscripts:

$\bar{}$ mean value

$'$ refers to image space associated with camera lens

APPENDIX B

RANDOM ERRORS IN FRINGE-SHIFT MEASUREMENTS

Random errors in measuring N were determined from interferograms obtained with monochromatic light (λ = 5461 Å). Two observers performed the measurements. The pitch of two adjacent interference maximums or minimums was measured five or 10 times, as noted in figure 2. Scatter of the results in figure 2 proved to be independent of the observer and independent of whether the measurements involved interference maximums or minimums. However, contrast variations influenced the scatter, the computed values of $\Delta d'_\infty$ being appreciably less for high-contrast interferograms than for low-contrast interferograms. The effect of the ratio of widths of interference maximums to minimums was not explicitly investigated, although the ratio varied from about 0.4 to 0.8.

It should be noted that the experimental results are based upon measurements made perpendicular to straight parallel fringes. When ρ is an arbitrary function of y, the fringe-shift measurements are made diagonal to curved fringes. Because the effective pitch in the x'-direction is the same when $\rho = \rho_\infty$ or $\rho = \rho(y)$, the value of $\Delta d'$ associated with measurements between the inclined fringes may be somewhat greater than the values presently reported because of the difficulty of exactly locating maximums and minimums along a diagonal path of approach. In addition, if the second derivative of ρ is large, then interference maximums and minimums will be displaced from the centerline of the bright and dark fringes, respectively, thus making settings on maximums and minimums indefinite. However, the fact that the normal pitch of the inclined bright and dark fringes is reduced may provide a compensating factor which tends to reduce $\Delta d'$.

The two-term approximation ($\mu_\eta = b_0 + b_1\eta$) equations for ρ^* and D are, neglecting corner effects,

$$\rho^* = 1 + \frac{1}{k\rho_\infty}\left[N\frac{\lambda}{L} - \frac{1}{6}(2 - 3K)b_1^2L^2\right]$$

$$D = \pm\frac{1}{2}(1 - 2K)b_1L^2$$

where

$$b_1 = \left|\frac{dN}{dy_D}\right|\frac{\lambda}{L}$$

The preceding equations are derived in reference 1. The corresponding primary maximum random errors of ρ^* and D are given by

$$\Delta\rho^* = (1 - \rho^*)\left(\frac{\Delta N}{N} + \frac{\Delta\rho_\infty}{\rho_\infty} + \frac{\Delta L}{L} + \frac{\Delta\lambda}{\lambda} + \frac{\Delta k}{k}\right)$$

$$\frac{\Delta D}{D} = \frac{\Delta(dN/dy_D)}{dN/dy_D} + 2\frac{\Delta K}{(1 - 2K)} + 3\frac{\Delta L}{L} + \frac{\Delta\lambda}{\lambda}$$

The importance of the error $\Delta N/N$ is of interest. Thus, as $\rho^* \to 1$, $1 - \rho^* \to 0$, and $\Delta N/N \to \infty$. Therefore, $\Delta N/N$ is the primary error. However, as $\rho^* \to 0$, $1 - \rho^* \to 1$, and $\Delta N/N \to 0$. Then $\Delta N/N$ becomes less significant and, in particular, may be insignificant compared with $\Delta\rho_\infty/\rho_\infty$.

APPENDIX C

SURFACE INTERFERENCE EFFECTS

The primary Zehnder-Mach interference pattern results from the superposition of the test beam, which traverses the test section containing the model, and the reference beam, which circumvents the test section. The observable forms of interference induced by a flat plate contained within the test section and oriented nominally parallel to the light beam appear to be primarily comprised as follows:

(1) Test beam plus reference beam (Zehnder-Mach interference)

(2) Diffraction by plate edge nearest light source

(3) Reference beam plus reflected beam

(4) Reference beam plus light diffracted by plate edge nearest image plane

Other sources of interference are not vital to the present discussion. The first two mentioned forms of interference are quite common. The third form is similar to Lloyd's mirror interference. No mention of the fourth form has been found in the literature.

Sources of the various forms of interference may be studied by

(1) Varying the angle φ

(2) Utilizing both light beams or the test beam only

(3) Varying the object plane of focus

(4) Utilizing a monochromatic or a white (incandescent) light source

(5) Varying the lateral extent of the light source

(6) Varying the orientation and pitch of the Zehnder-Mach interference fringes

Figures 5 and 6 were obtained with monochromatic light at grazing incidence to an optically flat aluminized front-surface mirror 7 inches in length. Additional experimental conditions associated with the photographs were as follows:

(1) Object plane was at the mirror midspan plane.

(2) Photographs in order a, b, c, . . . correspond to increasing φ, where photograph a corresponds to $\varphi \ll 0$.

(3) Figure 5 involves only the test beam and figure 6 includes both the test beam and the reference beam.

The wire appearing in the figures served to locate the surface at the object plane, and the irregularities (insulation) along the wire served to permit more critical focussing. In figure 5 the weak vertical bands were caused by glass striations in the camera lenses and are irrelevant to the present discussion.

In figure 6(a), for $\varphi \ll 0$, narrow reflection fringes similar to Lloyd's mirror fringes are visible. They are produced by the interaction of the reference beam and the reflected beam (rather than the test beam and the reflected beam, which corresponds to Lloyd's interference) because the fringes are inclined to the surface. As φ is increased ($\varphi < 0$), a second pattern of fringes (fig. 6(b)) gradually replaces the first pattern. The initial stage of formation of the second pattern is apparent in figure 6(a). The second pattern is inclined to the surface at a considerably greater angle than the first pattern. The second pattern is probably caused by interaction of the first pattern with light diffracted by the plate edge nearest the camera because the fringes are curved (rather than straight, as would be expected if interference were the sole cause). As φ is further increased until $\varphi > 0$, the second pattern disappears and a third pattern appears inclined oppositely to the second pattern (figs. 6(d) and (e)). The third pattern is apparently caused by the interaction of light diffracted by the plate edge nearest the light source with the reference beam. The fringes are diagonal and curved and are absent when the reference beam is eliminated. When $\varphi = 0$, the spurious pattern, except for the diffraction pattern produced by the plate edge nearest the light source, should disappear if the light source is a geometrical point source. In practice, the light source is always of finite lateral extent. Thus, the diagonal fringes do not disappear completely, but, rather, a "picket-fence" effect caused by the combination of the two opposed patterns of diagonal fringes is observed (fig. 6(c)) when the light beam and the surface are alined.

APPENDIX D

END CORRECTIONS

The free-stream density ρ_∞ within a wind tunnel can be determined from interference measurements if the boundary layers formed by gas flow along the wind-tunnel windows are taken into account.

The basic equations for optical-path difference $\Delta\psi$ and fringe shift N are, respectively,

$$\psi = \int_0^S \mu \, ds \tag{D1}$$

$$N\lambda = \Delta\psi \tag{D2}$$

where s is a physical length measured along a ray trace, and ψ is an optical-path length.

For the present, consider a coordinate z that is parallel to the interferometer optical axis and has its origin at the wind-tunnel wall which is initially traversed by the light. Let z increase positively in the direction of light propagation, as shown in figure 7. Let a second coordinate $\zeta \equiv z$ be associated with an individual ray trace. Also, let $\mu_2 = \mu_2(z)$ represent the refractive-index distribution in the boundary layers adjacent to the wind-tunnel windows. For a ray trace which traverses the free stream and the window boundary layers,

$$\psi_\infty = \mu_\infty(L - 2\delta_z) + 2\int_0^{\delta_z} \mu_2 d\zeta$$

where δ_z is the window boundary-layer thickness, and the flow is assumed to be symmetrical about the wind-tunnel midspan plane. For a ray trace through the reference hole r, which is connected to the external atmosphere,

$$\psi_r = \mu_r L$$

Therefore,

$$N_{\infty,r}\lambda = \psi_\infty - \psi_r = \mu_\infty(L - 2\delta_z) + 2\int_0^{\delta_z} \mu_2 d\zeta - \mu_r L$$

Boundary layers formed on wind-tunnel windows are usually turbulent. Thus, assume that μ_2 is of the form

$$\mu_2 = \mu(0) + [\mu_\infty - \mu(0)] \left(\frac{z}{\delta_z}\right)^{1/n} \quad \text{in the vicinity of} \quad z = 0$$

$$\mu_2 = \mu(L) + [\mu_\infty - \mu(L)] \left(\frac{L - z}{\delta_z}\right)^{1/n} \quad \text{in the vicinity of} \quad z = L$$

where $\mu(y = 0) \equiv \mu(0)$; and, because of symmetry, $\mu(0) = \mu(L)$. Then,

$$\int_0^{\delta_z} \mu_2 d\zeta = \int_0^{\delta_z} \left[\mu_{2,w} + (\mu_\infty - \mu_{2,w}) \left(\frac{\zeta}{\delta_z}\right)^{1/n}\right] d\zeta$$

$$= \mu_{2,w}\delta_z + (\mu_\infty - \mu_{2,w}) \frac{n}{n + 1} \delta_z$$

where

$\mu_{2,w} \equiv \mu(0) = \mu(L)$

It follows that

$$N_{\infty,r}\lambda = \mu_\infty(L - 2\delta_z) - \mu_r L + 2\delta_z \left[\mu_{2,w}\left(\frac{1}{n + 1}\right) + \mu_\infty\left(\frac{n}{n + 1}\right)\right]$$

$$= (\mu_\infty - \mu_r) \left(L - \frac{2}{n + 1} \delta_z\right) + (\mu_{2,w} - \mu_r) \frac{2}{n + 1} \delta_z$$

However,

$$\mu = 1 + k\rho \tag{D3}$$

and the optical-path difference in hole w with respect to hole r is, according to equations (D1) and (D2),

$$N_{w,r}\lambda = (\mu_w - \mu_r)L$$

Therefore,

$$\rho_w - \rho_r = N_{w,r} \frac{\lambda}{KL} \tag{D4}$$

Assume that the densities at the windows and the other tunnel walls or model surface are equal, that is, that $\rho_{2,w} = \rho_w$. Then, substituting expressions (D3) and (D4) in the previous equations for $N_{\infty,r}\lambda$ and solving for ρ_∞ yield

$$\rho_\infty = \rho_r + N_{\infty,r}\frac{\lambda}{kL_e} - \frac{2}{n+1}N_{w,r}\frac{\lambda\delta_z}{kLL_e} \tag{D5}$$

where

$$L_e = L - \frac{2}{n+1}\delta_z$$

The method for determining ρ_∞ and ρ_w is as follows:

(1) "White-light" interference fringes are oriented perpendicular to the wind-tunnel wall or model surface. Flow is then initiated in the wind tunnel. When equilibrium conditions are attained, the pressure, temperature, and density within holes w and r are, respectively, denoted by

(a) Static hole w: p_w, T_w, ρ_w

(b) Reference hole r: p_r, T_w, ρ_r

where the wall or model temperature is assumed to be constant in the region of interest.

(2) The fringe pitch is adjusted until the zero-order fringe appears centered in both holes simultaneously. This is always possible except when the flow is transient, as occurs in blow-down tunnels. If $p_w = p_r$, the infinite-fringe adjustment results.

(3) Alternate interferograms are obtained by using the desired monochromatic light and a white-light source. The white-light interferograms are used for locating the zero-order fringes in the interferograms obtained by using the monochromatic source when minor flow instabilities exist. Simultaneously, measurements of p_a, T_a, and T_w are made by using a barometer, a thermometer, and a thermocouple installed at the surface in the region of interest, respectively.

The values of the densities ρ_∞ and ρ_w can be computed in the following manner:

(1) The atmospheric density ρ_a is calculated from

$$\rho_a = \frac{p_a}{RT_a}$$

where R is a gas constant, and p_a and T_a are given by the barometer and thermometer, respectively.

(2) Then, ρ_r is given by

$$\rho_r = \frac{T_a}{T_w} \rho_a$$

where T_w is obtained from the thermocouple.

(3) The density ρ_w at the surface of the model is then calculated from

$$\rho_w = \rho_r + N_{w,r} \frac{\lambda}{kL}$$

where $N_{w,r}$, the number of fringes in the x' interval between the zero-order fringes in holes w and r, may be determined readily because the fringe pitch d' may be measured and is independent of the magnitude of ρ in the two holes.

(4) The free-stream density ρ_∞ is given by

$$\rho_\infty = \rho_r + N_{\infty,r} \frac{\lambda}{kL_e} - \frac{2}{n+1} N_{w,r} \frac{\lambda \delta_z}{kLL_e}$$

where

$$L_e = L - \frac{2}{n+1} \delta_z$$

and $N_{\infty,r}$ is the number of fringes in the x'-interval between the zero-order fringe in the reference hole and the zero-order fringe in the region corresponding to the free stream.

APPENDIX E

REFRACTION AND CORNER CORRECTIONS (MODEL SPANS WIND TUNNEL)

Evaluation equations which include corner, as well as refraction, corrections can be derived by extending the analysis contained in reference 1.

Assume that Cartesian coordinates x,y,z form a right-handed system having its origin at the intersection of the leading edge of the model with the wind-tunnel wall which is initially traversed by the interferometer light beam. Coordinate z is taken essentially parallel to the light path, as shown in figure 8, and coordinates x and y are essentially perpendicular to the light path. A system of conjugate coordinates x',y',z' are determined in the camera-image space by the relations

$$x' = -mx$$

$$y' = -my$$

$$z' = m^2 z$$

where m is the lateral magnification produced by the camera lens. A third set of Cartesian coordinates ξ,η,ζ is associated with each individual ray trace such that

$$\xi \equiv |x - x_0|$$

$$\eta \equiv |y - y_0|$$

$$\zeta \equiv z$$

where the initial coordinates of any given ray trace entering the wind tunnel are $(x,y,z) \equiv (x_0,y_0,0)$, or $(\xi,\eta,\zeta) \equiv (0,0,0)$. Consider boundary-layer refractive-index distributions:

$\mu = \mu(y)$ adjacent to the model surface

$\mu_2 = \mu_2(z)$ adjacent to the wind-tunnel walls

Let δ_y and δ_z denote the boundary-layer thicknesses associated with μ and μ_2, respectively. The quantities δ_y and δ_z will always be regarded as positive. Although the geometry of the corner boundary layers may be similar to the geometries shown in reference 22, for

simplicity of the subsequent analysis the isopycnic lines will be assumed to form right angles in the corners. Thus, μ and μ_2 extend into the corners and intersect along the diagonal surfaces

$$y/z = \delta_y/\delta_z \qquad (0 \leq z \leq \delta_z)$$

$$y/(L - z) = \delta_y/\delta_z \qquad (L - z \leq z \leq L)$$

(round corner)

Note that the fillet adjacent to the ambient region is thereby neglected. The preceding assumption should be reasonably valid because Kennard (ref. 4) has shown by example that a measured distribution $\rho(y)$ is relatively insensitive to variations of the assumed corner geometry. The resulting geometry and representive ray traces are shown in figure 8. As in appendix D, symmetry of the boundary layers is assumed.

As in reference 1, μ is assumed to be monotonic and representable for each ray trace in terms of η as

$$\mu_\eta \equiv \mu_0 + \Delta\mu_\eta \equiv \sum_{\nu=0}^{\infty} b_\nu \eta^\nu \equiv \sum_{\nu=0}^{\infty} b_\nu |y - y_0|^\nu$$

in an interval $y_H - y_0$, where $y = y_H$ when $\eta = H$, $\mu = \mu_0$ at $\eta = 0$, and $\Delta\mu_\eta << 1$ because $\mu \approx 1$. The subscript notation is used for η in order to differentiate between μ as a function of y and μ as a function of η. The coefficient b_ν is defined by

$$b_\nu \equiv \frac{1}{\nu!}\left(\frac{d^\nu \mu}{d\eta^\nu}\right)_0 \equiv \pm \frac{1}{\nu!}\left(\frac{d^\nu \mu}{dy^\nu}\right)_{y_0}$$

where the choice of the + or - sign depends upon whether μ is an increasing or decreasing function of y, respectively.

Light Path

The ray traces are straight lines, except in the field μ, where, as in reference 1, it is assumed that each ray trace can be represented by the power series

$$\eta = \sum_{\sigma=0}^{\infty} c_\sigma^* \zeta^\sigma$$

where, by definition,

$$c_\sigma^* \equiv \frac{1}{\sigma!}\left(\frac{d^\sigma \eta}{d\zeta^\sigma}\right)_0 \equiv \pm \frac{1}{\sigma!}\left(\frac{d^\sigma y}{dz^\sigma}\right)_0$$

If the light source is an axial-point source, the limiting ray-trace displacement $\eta = H$ in the field μ is given by

$$H = \sum_{\sigma=2,4,6,\ldots}^{\infty} c_\sigma^* L_R^\sigma$$

where

$$c_2^* = \frac{1}{2} b_1$$

$$c_4^* = \frac{1}{12} b_1 b_2, \ldots$$

and the reduced model span L_R is given by

$$L_R = L - (\zeta_1 + \zeta_2)$$

where, by virtue of the boundary conditions,

$$\zeta_1 = \frac{\delta_z}{\delta_y} y_0$$

$$\zeta_2 = \frac{\delta_z}{\delta_y} y_H$$

The ultimate displacement at $\zeta = L$ is, approximately,

$$H + \zeta_2 \left(\frac{d\eta}{d\zeta}\right)_L$$

Distortion

In closed form the distortion is given by

$$D = H + (\zeta_2 - KL)\left(\frac{d\eta}{d\zeta}\right)_L$$

where

$$K = 1 - \frac{z_R}{L}$$

and z_R is the real locus of points which are imaged at the selected image plane. By virtue of the ray-trace series and the corresponding expansion

$$\left(\frac{d\eta}{d\zeta}\right)_L = \sum_{\sigma=2,4,6,\ldots}^{\infty} \sigma c_\sigma^* L_R^{\sigma-1}$$

for its derivative, the distortion is given in series form by

$$D = \pm \sum_{\sigma=2,4,6,\ldots}^{\infty} \left[L_R - \sigma(KL - \zeta_2)\right] c_\sigma^* L_R^{\sigma-1}$$

Fringe Shift

In the present instance the measured fringe shift serves to associate the boundary-layer density distribution $\rho(y)$ with the free-stream density ρ_∞. By applying equations (D1) and (D2), the optical length ψ_1 of a ray trace through the plate and window boundary layers is given by

$$\psi_1 = \int_0^{\zeta_1} \mu_2 d\zeta + \int_{\zeta_1}^{L_R+\zeta_1} \mu_\eta ds + \int_{L_R+\zeta_1}^{L} \mu_2 ds$$

whereas for a ray trace through the free stream and window boundary layers,

$$\psi_\infty = \mu_\infty(L - 2\delta_z) + 2\int_0^{\delta_z} \mu_2 d\zeta + \mu_a KL(\sec \beta_L - 1)$$

where

$$ds = \sqrt{1 + \left(\frac{d\eta}{d\zeta}\right)^2}\, d\zeta$$

$$\tan \beta = d\eta/d\zeta$$

$\beta = \beta_L$ at $\zeta = L$, and the last term in the expression for ψ_∞ results from refraction (ref. 20). Ray traces through the field μ are given in terms of the auxiliary coordinates ξ, η, ζ by the differential equation (ref. 20)

$$1 + \left(\frac{d\eta}{d\zeta}\right)^2 = \left(\frac{\mu_\eta}{\mu_0}\right)^2$$

It follows that

$$\sec \beta = \frac{\mu_\eta}{\mu_0}$$

Thus, $N\lambda = \psi_1 - \psi_\infty$, or

$$N\lambda = \int_0^{\zeta_1} \mu_2 d\zeta + \mu_0 L_R + 2\int_{\zeta_1}^{L_R+\zeta_1} \Delta\mu_\eta d\zeta + \frac{\mu_H}{\mu_0}\int_{L_R+\zeta_1}^{L} \mu_2 d\zeta - \mu_\infty(L - 2\delta_z) - 2\int_0^{\delta_z} \mu_2 d\zeta - \frac{\mu_a}{\mu_0} KL\,\Delta\mu_H \tag{E1}$$

which results by substituting the right sides of the four preceding expressions into the expressions for ψ_1 and ψ_∞, and then expanding μ_η^2/μ_0 in the form

$$\frac{\mu_\eta^2}{\mu_0} = \mu_0 + 2\Delta\mu_\eta + \ldots$$

where terms in $\Delta\mu_\eta^2 \ldots$ are infinitesimals of higher order.

Algebraic expressions for those integrals which involve μ_2 depend upon the functional form of μ_2. However, the integral involving $\Delta\mu_\eta$ can be evaluated in series form, as in reference 20.

Solution for an effective-average window-boundary-layer density distribution. - Assume that $\int \mu_2 d\zeta$ is of the form

$$\int_A^B \mu_2 d\zeta = \frac{1}{2}\left[\mu_2(B) - \mu_2(A)\right](B - A)$$

which is strictly not an average density assumption although it, henceforth, will be referred to as such. Because of symmetry, $\mu(0) = \mu(L) = \mu_{2,w}$, and equation (E1), therefore, becomes

$$N\lambda = \frac{1}{2}(\mu_{2,w} - \mu_0)\zeta_1 + \mu_0 L_R + 2\int_{\zeta_1}^{L_R+\zeta_1} \Delta\mu_\eta d\zeta +$$

$$\frac{\mu_H}{2\mu_0}(\mu_H + \mu_{2,w})\zeta_2 - \mu_\infty(L - 2\delta_z) - (\mu_{2,w} + \mu_\infty)\delta_z - \frac{\mu_a}{\mu_0} KL\,\Delta\mu_H$$

The fourth term on the right side of the preceding equation can be expanded as follows:

$$\frac{\mu_H}{2\mu_0}(\mu_H + \mu_{2,w})\zeta_2 = \frac{1}{2}\left(\mu_0 + 2\Delta\mu_H + \mu_{2,w} + \frac{\mu_{2,w}}{\mu_0}\Delta\mu_H\right)\zeta_2$$

However,

$$\frac{\mu_{2,w}}{\mu_0},\ \frac{\mu_a}{\mu_0} \approx 1$$

Thus, letting

$$L_E = L_R + \frac{1}{2}(\zeta_1 + \zeta_2) = L - \frac{1}{2}(\zeta_1 + \zeta_2)$$

there results, following rearrangement of terms,

$$N\lambda = (\mu_0 - \mu_\infty)L_E + (\mu_\infty - \mu_{2,w})\left[\delta_z - \frac{1}{2}(\zeta_1 + \zeta_2)\right] +$$

$$2\int_{\zeta_1}^{L_R+\zeta_1} \Delta\mu_\eta d\zeta + \frac{1}{2}(3\zeta_2 - 2KL)\Delta\mu_H$$

By utilizing the series expansions for μ and η, and by translating the coordinates of the integral in order to give a lower limit of zero, the preceding equation becomes in series form

$$N\lambda = (\mu_0 - \mu_\infty)L_E + (\mu_\infty - \mu_{2,w})\left[\delta_z - \frac{1}{2}(\zeta_1 + \zeta_2)\right] +$$

$$2\sum_{\nu=1}^{\infty}\sum_{\sigma=2,4,6,\ldots}^{\infty}\frac{b_\nu c_{\sigma,\nu}}{\sigma+1}L_R^{\sigma+1} +$$

$$\frac{1}{2}(3\zeta_2 - 2KL)\sum_{\nu=1}^{\infty}\sum_{\sigma=2,4,6,\ldots}^{\infty} b_\nu c_{\sigma,\nu} L_R^{\sigma} \qquad \text{(E2)}$$

where the coefficients $c_{\sigma,\nu}$ are given by (ref. 20)

$$c_{2,1} = \frac{1}{2}b_1 \qquad c_{2,2} = 0 \qquad \ldots$$

$$c_{4,1} = \frac{1}{12}b_1 b_2 \qquad c_{4,2} = \frac{1}{4}b_1^2 \qquad \ldots$$

$$\vdots \qquad \vdots \qquad \vdots$$

Solution for power-law window-boundary-layer density distribution. - Assume that

$$\mu_2 = \mu(0) + \left[\mu_\infty - \mu(0)\right]\left(\frac{\zeta}{\delta_z}\right)^{1/n} \qquad (0 \leqq \zeta \leqq \delta_z)$$

$$\mu_2 = \mu(L) + \left[\mu_\infty - \mu(L)\right]\left(\frac{L-\zeta}{\delta_z}\right)^{1/n} \qquad (L - \delta_z \leqq \zeta \leqq L)$$

Because of symmetry, $\mu(0) = \mu(L) = \mu_{2,w}$, as before. Following integration of those integrals which involve μ_2 (in the same manner as in appendix D) and the collection, whenever possible, of like terms in μ, equation (E1) becomes

$$N\lambda = (\mu_0-\mu_\infty)L_R-(\mu_\infty-\mu_{2,w})\left\{\zeta_1+\zeta_2-2\delta_z-\frac{n}{n+1}\delta_z\left[\left(\frac{\zeta_1}{\delta_z}\right)^{\frac{n+1}{n}}+\left(\frac{\zeta_2}{\delta_z}\right)^{\frac{n+1}{n}}-2\right]\right\}+$$

$$2\int_{\zeta_1}^{L_R+\zeta_1}\Delta\mu_\eta\,d\zeta+\left[\frac{\mu_{2,w}}{\mu_0}\zeta_2-\frac{\mu_a}{\mu_0}KL+\frac{n}{n+1}\frac{\mu_\infty-\mu_{2,w}}{\mu_0}\left(\frac{\zeta_2}{\delta_z}\right)^{\frac{n+1}{n}}\delta_z\right]\Delta\mu_H$$

However, because

$$\frac{\mu_{2,w}}{\mu_0}, \frac{\mu_a}{\mu_0} \approx 1$$

and the term $\frac{n}{n+1}\frac{\mu_\infty - \mu_{2,w}}{\mu_0}\left(\frac{\zeta_2}{\delta_z}\right)^{\frac{n+1}{n}}\delta_z$ is of smaller order than the adjacent terms, it follows that

$$N\lambda = (\mu_0 - \mu_\infty)L_R +$$

$$(\mu_\infty - \mu_{2,w})\left\{\frac{2}{n+1}\delta_z - (\zeta_1 + \zeta_2) + \frac{n}{n+1}\delta_z\left[\left(\frac{\zeta_1}{\delta_z}\right)^{\frac{n+1}{n}} + \left(\frac{\zeta_2}{\delta_z}\right)^{\frac{n+1}{n}}\right]\right\} +$$

$$2\int_{\zeta_1}^{L_R+\zeta_1} \Delta\mu_\eta d\zeta + (\zeta_2 - KL)\Delta\mu_H$$

which becomes in series form

$$N\lambda = (\mu_0 - \mu_\infty)L_R +$$

$$(\mu_\infty - \mu_{2,w})\left\{\frac{2}{n+1}\delta_z - (\zeta_1 + \zeta_2) + \frac{n}{n+1}\delta_z\left[\left(\frac{\zeta_1}{\delta_z}\right)^{\frac{n+1}{n}} + \left(\frac{\zeta_2}{\delta_z}\right)^{\frac{n+1}{n}}\right]\right\} +$$

$$2\sum_{\nu=1}^{\infty}\sum_{\sigma=2,4,6,\ldots}^{\infty}\frac{b_\nu c_{\sigma,\nu}}{\sigma+1}L_R^{\sigma+1} + (\zeta_2 - KL)\sum_{\nu=1}^{\infty}\sum_{\sigma=2,4,6,\ldots}^{\infty} b_\nu c_{\sigma,\nu} L_R^\sigma \qquad \text{(E3)}$$

Evaluation Equations

The final evaluation equations can be derived by applying the preceding results in the same manner as in reference 1. The procedure is as follows: After $1 + k\rho$ is substituted for μ (with the appropriate subscript retained), equation (E2), or (E3), is solved for $\rho^* = \rho_0/\rho_\infty$, the choice of equation depending upon the choice of the window-boundary-layer assumption. The quantity ρ_0 represents the density associated with the profile $\rho(y)$ at the ordinate value y_0. The expansion

$$\mu_\eta = \sum_{\nu=0}^{\infty} b_\nu \eta^\nu$$

determines the final form of the evaluation equations. Thus, the final equations are denoted according to the number of terms of the preceding series which are utilized. Only the one- or two-term approximations appear to be of practical use when corner corrections are to be made. By considering only two terms of the series, all coefficients b_ν $(\nu > 1)$ are assumed to be zero; hence all coefficients c^*_σ and $c_{\sigma,\nu}$ which involve b_ν $(\nu > 1)$ are also zero. If only the first term $b_0 \equiv \mu_0$ of the series expansion for μ_η is considered, then all the Σ sums are zero. Because $\rho^* = \rho_0/\rho_\infty$ at $y = y_0$, whereas the corresponding measured value of N is associated with $y = y_D$, the indicated distortion correction must be performed in order to determine the value of y_0. If the preceding operations are performed, the evaluation equations (with the exception of b_1) presented in the section Density Field $\rho(y)$ (Model Spans Wind Tunnel) are obtained. The derivation of expressions for b_1 is considerably more complicated. First, equation (E2), or (E3), is differentiated with respect to y. An expression for dN/dy at $y = y_0$ is, thereby, obtained. However, by measurements on an interferogram a distorted value dN/dy_D at $y = y_D$ is obtained. It is shown in reference 1 that the two quantities are related by

$$\left(\frac{dN}{dy_D}\right)_{y_D} = \frac{\left(\frac{dN}{dy}\right)_{y_0}}{1 + \frac{dD}{dy}}$$

Therefore, the series expansion for D must also be differentiated with respect to y. When the expressions for dN/dy and dD/dy are substituted in the preceding equation, three additional assumptions, namely,

(1) $b_1 L \ll 1$

(2) δ_z/δ_y is of the order of unity

(3) $b_1 L \delta_z/\delta_y \ll 1$

permit reduction of the equation to a form which is linear with respect to b_1. Because $(d\eta/d\zeta)_L = b_1 L$ is the maximum slope of any given ray

trace with respect to the optical axis, assumption 1 is certainly valid in practice. Moreover, if the window-boundary-layer thickness does not exceed the model-boundary-layer thickness by an order of magnitude, then assumptions 2 and 3 are satisfied. The intermediate equations are

$$\pm b_1 = \frac{dN}{dy_D}\frac{\lambda}{L_E} + \frac{1}{L_E}\frac{\delta_z}{\delta_y}\left[N\frac{\lambda}{L_E} + k\rho_\infty\left(\frac{\rho_\infty - \rho_{2,w}}{\rho_\infty}\right)\left(1 + \frac{\delta_z - \zeta_1}{L_E}\right)\right]$$

for the effective-average density assumption, or

$$\pm b_1 = \frac{dN}{dy_D}\frac{\lambda}{L_R} + \frac{2}{L_R^2}\frac{\delta_z}{\delta_y}\left(N\lambda - 2k\rho_\infty\left(\frac{\rho_\infty - \rho_{2,w}}{\rho_\infty}\right)\left\{\frac{\delta_z}{n+1}\left[1 + n\left(\frac{\zeta_1}{\delta_z}\right)^{\frac{n+1}{n}}\right] - \zeta_1\right\}\right) +$$

$$\frac{2}{L_R}k\rho_\infty\left(\frac{\rho_\infty - \rho_{2,w}}{\rho_\infty}\right)\left[1 - \frac{\delta_z}{\delta_y}\left(\frac{\zeta_1}{\delta_z}\right)^{1/n}\right]$$

for the power-law density assumption. In practice all terms in each expression for b_1 are usually small compared with the first term (say less than 10 percent of the first term) and, also, will tend to cancel when algebraic signs are considered. The final expressions for b_1 are then, respectively,

$$b_1 = \left|\frac{dN}{dy_D}\right|\frac{\lambda}{L_E}$$

or

$$b_1 = \left|\frac{dN}{dy_D}\right|\frac{\lambda}{L_R}$$

In any given experiment the maximum values of the neglected terms should be estimated in order to confirm the validity of the final solutions. Unless the resultant magnitude of the neglected terms is considerably greater than 5 or 10 percent of the first term, they can still be neglected because the error in determining dN/dy_D alone can cause an error of 5 or 10 percent in determining b_1.

APPENDIX F

REFRACTION AND CORNER CORRECTIONS (MODEL NOT CONTAINED WITHIN WIND TUNNEL)

If the model is not contained within a wind tunnel, then the function μ, the coordinate systems, and the quantities δ_y and δ_z can be defined as in appendix E. The additional function $\mu_3 = \mu_3(y,z)$ is introduced to represent the refractive-index distribution at the corners and l_z defines the extent of the corner boundary layers in the z-direction. The appropriate geometry and representative ray traces are shown in figure 9. The assumed geometry of the corner boundary layers is likely to be more critical than in appendix E because the radii of the isopycnic lines around the ends of the model are relatively larger. However, Kennard's results (cf. appendix E) apply specifically to the present case. It will be assumed that the outline of the boundary layer in the vicinity of the spanwise ends of the model is representable by the hyperbolas

$$(y - \delta_y)(\delta_z + z) = -a^2/2$$

in the vicinity of $z = 0$, and

$$(y - \delta_y)(z - L - \delta_z) = a^2/2$$

in the vicinity of $z = L$, where a is the perpendicular distance from the isopyncnic line bounding the ambient fluid to the intersection of the asymptotes of the hyperbola.

Light Path

In the field μ,

$$H = \sum_{\sigma=2,4,6,\ldots}^{\infty} c_\sigma \bar{L}_R^\sigma$$

where the reduced model span is given by

$$\bar{L}_R = L - 2(l_z - \delta_z)$$

The ultimate displacement in the space-variant field is, approximately,

$$H + \overline{\zeta}_2 \left(\frac{d\eta}{d\zeta}\right)_{\overline{L}_R}$$

Distortion

In closed form the distortion is given by

$$D = H - (KL + \delta_z - l_z)\left(\frac{d\eta}{d\zeta}\right)_{\overline{L}_R}$$

or, in series form,

$$D = \pm \sum_{\sigma=2,4,6,\ldots}^{\infty} \left[\overline{L}_R - \sigma(KL + \delta_z - l_z)\right] c_\sigma^* \overline{L}_R^{\sigma-1}$$

Fringe Shift

The determination of the boundary-layer distribution $\rho(y)$ with respect to the ambient density is of interest. Thus,

$$\psi_1 = \int_{l_z-\delta_z-\overline{\zeta}_1}^{l_z-\delta_z} \mu_3 d\zeta + \int_{l_z-\delta_z}^{L+\delta_z-l_z} \mu \, ds + \int_{L+\delta_z-l_z}^{L+\delta_z-l_z+\overline{\zeta}_2} \mu_3 ds$$

$$\psi_\infty = \mu_\infty \left[(L - 2l_z + 2\delta_z + \overline{\zeta}_1 + \overline{\zeta}_2) + (KL + \overline{\zeta}_2 + \delta_z - l_z)(\sec \beta_L - 1)\right]$$

The upper limit of $\int \mu_3 ds$ is only approximate. However, because

(1) The exact profile of the boundary-layer outline is indefinite

(2) The exact corner density distribution is unknown

the assumed upper limit appears to be sufficiently accurate for practical purposes. Performing the operations indicated in appendix E yields

$$N\lambda = \psi_1 - \psi_\infty = \mu_0\bar{L}_R + 2\int_{L-\bar{L}_e}^{\bar{L}_e} \Delta\mu_\eta ds + \int_{L-\bar{L}_e-\bar{\zeta}_1}^{L-\bar{L}_e} \mu_3 d\zeta + \frac{\mu_H}{\mu_0}\int_{\bar{L}_e}^{\bar{L}_e+\bar{\zeta}_2} \mu_3 d\zeta -$$

$$\mu_\infty(\bar{L}_R + \bar{\zeta}_1 + \bar{\zeta}_2) - \frac{\mu_\infty}{\mu_0}\left[(K - 1)L + \bar{L}_e + \bar{\zeta}_2\right]\Delta\mu_H \qquad (F1)$$

where

$$\bar{L}_e = L - l_z + \delta_z$$

Assuming an effective-average end density distribution corresponds to assuming that

$$\int_{L-\bar{L}_e-\bar{\zeta}_1}^{L-\bar{L}_e} \mu_3 d\zeta = \frac{1}{2}(\mu_\infty + \mu_0)\bar{\zeta}_1$$

$$\int_{\bar{L}_e}^{\bar{L}_e+\bar{\zeta}_2} \mu_3 d\zeta = \frac{1}{2}(\mu_H + \mu_\infty)\bar{\zeta}_2$$

Then equation (F1) reduces to

$$N\lambda = (\mu_0 - \mu_\infty)\bar{L}_E + 2\int_{L-\bar{L}_e}^{\bar{L}_e} \Delta\mu_\eta d\zeta - \left[(K - 1)L + \bar{L}_e - \frac{1}{2}\bar{\zeta}_2\right]\Delta\mu_H$$

where the effective-test-section span is

$$\bar{L}_E = \bar{L}_R + \frac{1}{2}(\bar{\zeta}_1 + \bar{\zeta}_2)$$

In series form the result is

$$N\lambda = (\mu_0 - \mu_\infty)\bar{L}_E + 2\sum_{\nu=1}^{\infty}\sum_{\sigma=2,4,6,\ldots}^{\infty} \frac{b_\nu c_{\sigma,\nu}}{\sigma + 1}\bar{L}_R^{\sigma+1} -$$

$$\left[(K - 1)L + \bar{L}_e - \frac{1}{2}\bar{\zeta}_2\right]\sum_{\nu=1}^{\infty}\sum_{\sigma=2,4,6,\ldots}^{\infty} b_\nu c_{\sigma,\nu}\bar{L}_R^{\sigma}$$

Evaluation Equations

The final evaluation equations are obtained in the same manner as in appendix E. If, as in appendix E, it is assumed that $b_1 L \ll 1$, then

$$\pm b_1 = \frac{dN}{dy_D}\frac{\lambda}{\overline{L}_E} + \frac{1}{4}\frac{k\rho_\infty}{\overline{L}_E}\left(\frac{\rho_O - \rho_\infty}{\rho_\infty}\right)a^2\left[\frac{1}{(y_O - \delta_y)^2} + \frac{1}{(y_H - \delta_y)^2}\right]$$

which reduces to

$$b_1 \doteq \left|\frac{dN}{dy_D}\right|\frac{\lambda}{\overline{L}_E}$$

when the second term is small compared with the first term. The second term is usually small compared with the first term because, by assumption, $\frac{a^2}{2(y_O - \delta_y)^2}, \frac{a^2}{2(y_H - \delta_y)^2} \leq 1_z$. This assumption is required by the fact that the isopycnic lines are assumed to be hyperbolic at the corners. It can only be violated when $y_O, y_H \to \delta_y$. However, in the vicinity of $y = \delta_y$, $\rho(y) \to \rho_\infty$ and the entire corner correction is then known to be negligible from physical considerations.

APPENDIX G

EFFECT OF NONUNIFORM HEATING OF WIND-TUNNEL WINDOWS

Consider two ray traces which traverse a test section bounded by windows. Assume that the traces are parallel to the optical, or z-, axis and that refraction is negligible. Let $\tau(z)$ represent the temperature difference at any given value of z along the two paths within each window, where by symmetry $\tau(z)$ possesses the same distribution throughout both windows. Then, neglecting possible effects of thermal stresses within the glass,

$$\Delta\psi = 2(\alpha\mu_g + \beta)\int_0^t \tau(z)dz$$

within the two windows, where t is the window thickness. The coefficient of thermal expansion α and the temperature coefficient of refractive index β possess, for ordinary crown glass ($\mu_g \approx 1.52$), the respective values

$$\alpha \approx 8\times10^{-6}/^{\circ}C$$

$$\beta \approx 1.5\times10^{-6}/^{\circ}C$$

at 20° C for $\lambda = 5893$ Å (sodium D-lines). In terms of the error $\Delta\rho^*$ in ρ^*, the preceding expression becomes

$$\Delta\rho^* = \frac{2(\alpha\mu_g + \beta)}{k\rho_\infty L}\int_0^t \tau(z)dz$$

Usually $\tau(z) \ll |T_{2,w} - T_a|$, so that $\tau(z)$ can be regarded as a linear function of z, corresponding to heat conduction through a plane wall of infinite lateral extent. Thus,

$$\Delta\rho^* = \frac{2(\alpha\mu_g + \beta)}{k\rho_\infty}\frac{t}{L}\tau(0)$$

where $\tau(0)$ represents the temperature difference at the internal surfaces of the windows. The preceding values of the required constants were used to compute the value of $\Delta\rho^*$ reported in the section Supersonic Air Flow Along a Flat Plate.

APPENDIX H

CYLINDRICAL MODEL

The cylindrical model consists of a 3-inch-diameter, 8-inch-long Duralumin tube with 1-inch-thick walls and is bounded on both ends by 1-inch-thick removable end caps. The end caps support a 3/4-inch-diameter alundum tube wound with nichrome resistance wire within the outer cylinder. The resistance-wire leads were passed out through the centers of the end caps (one lead through each cap) and insulated from the caps by Fiberglas sleeving. The spacing of the resistance wire was reduced near the ends of the tube in an attempt to produce uniform heating of the exterior surface of the outer cylinder. Iron-constantan thermocouples were located at 11 points on the exterior surface of the Duralumin cylinder. Temperatures indicated by the thermocouples were recorded automatically.

For experimental purposes the heater was suspended from an adjustable horizontal supporting rod by piano wire. Thus, the heater was, effectively, freely suspended in space. Air conditioning in the large room in which the experiment was performed was shut off, and the cylinder was shielded from stray air currents. The heater current was controllable by means of an autotransformer, thus permitting attainment of a virtual steady-state condition while obtaining an interferogram and simultaneously recording the surface temperatures.

A small ambient temperature rise (approximately 1° F) was recorded in the shielded region during each run by means of a thermometer. The effect of the ambient temperature rise was included in the calculation of the temperature profiles. The temperature variation over the exterior surface of the cylinder was found to be less than 2° F throughout the range $24^\circ \text{ F} < \Theta < 450^\circ \text{ F}$.

REFERENCES

1. Howes, Walton L., and Buchele, Donald R.: Generalization of Gas-Flow-Interferometry Theory and Interferogram Evaluation Equations for One-Dimensional Density Fields. NACA TN 3340, 1955.

2. Wachtell, G. P.: The Refraction Problem. Pt. VIII in Optical Studies of Boundary Layer Phenomena on a Flat Plate at Mach Number 2.35 by R. Ladenburg and D. Bershader. Final Tech. Rep. NR061-020, Palmer Phys. Lab., Princeton Univ., Dec. 15, 1952, pp. 81-124. (Contract N6ori-105, Task II.)

3. DeFrate, Louis A.: Application of the Interferometer to the Study of Boundary Layers. Sc. D. Thesis, M.I.T., 1950.

4. Kennard, R. B.: An Optical Method for Measuring Temperature Distribution and Convective Heat Transfer. Jour. Res. Nat. Bur. Standards, vol. 8, no. 5, May 1932, pp. 787-805.

5. Eckert, E. R. G., and Soehngen, E. E.: Studies on Heat Transfer in Laminar Free Convection with the Zehnder-Mach Interferometer. Tech. Rep. 5747, A.T.I. No. 44580, Air Materiel Command, Wright-Patterson Air Force Base, Dec. 27, 1948.

6. Bershader, Daniel: An Interferometric Study of Supersonic Channel Flow. Rev. Sci. Instr., vol. 20, no. 4, Apr. 1949, pp. 260-275.

7. Wachtell, George Peter: Refraction Error in Interferometry of Boundary Layer in Supersonic Flow Along a Flat Plate. Ph. D. Thesis, Princeton Univ., 1951.

8. Ladenburg, R., and Bershader, D.: Optical Studies of Boundary Layer Phenomena on a Flat Plate at Mach Number 2.35. Palmer Phys. Lab., Princeton Univ., Dec. 15, 1952. (Contract N6ori-105, Task II.)

9. Lange, A. H.: Temperature Measurements in the Wake of Bodies in Supersonic Flow. Heat Transfer and Fluid Mech. Inst., Stanford Univ. Press, 1953, pp. 57-70.

10. Blue, Robert E.: Interferometer Corrections and Measurements of Laminar Boundary Layers in Supersonic Stream. NACA TN 2110, 1950.

11. Groth, E.: Sensitivity and Accuracy of the Interference Method Applied to Pressure Measurements in Wind Tunnels. Appendix to Investigation of the Flow past Finite Wedges of 20 deg. and 40 deg. Apex Angle at Subsonic and Supersonic Speeds, using a Mach-Zehnder Interferometer by D. C. Pack. R. & M. No. 2321, British A.R.C., May 1946.

12. Bennett, F. D., Carter, W. C., and Bergdolt, V. E.: Interferometric Analysis of Airflow About Projectiles in Free Flight. Rep. No. 797, Ballistic Res. Lab., Aberdeen Proving Ground (Md.), Mar. 1952. (Proj. TB3-0108 of Res. and Dev. Div., Ord. Corps.)

13. Ladenburg, R., Van Voorhis, C. C., and Winckler, J.: Interferometric Study of Supersonic Phenomena. Pt. II. The Gas Flow Around Various Objects in a Free Homogeneous Supersonic Air Stream. Navord Rep. 93-46, Bur. Ord., Navy Dept., Sept 2, 1946.

14. Habell, K. J., and Cox, Arthur: Engineering Optics. Sir Isaac Pitman & Sons (London), 1948, pp. 294-297.

15. DeFrate, L. A., Barry, F. W., and Bailey, D. Z.: A Portable Mach-Zehnder Interferometer. Meteor Rep. No. 51, Guided Missiles Program, M.I.T., Feb. 1950. (Bur. Ord. Contract NOrd 9661.)

16. Ashkenas, Harry I., and Bryson, Arthur E.: Design and Performance of a Simple Interferometer for Wind-Tunnel Measurements. Jour. Aero. Sci., vol. 18, no. 2, Feb. 1951, pp. 82-90.

17. Hall, J. G.: The Design and Performance of a 9-Inch Plate Mach-Zehnder Interferometer. UTIA Rep. No. 27, Inst. Aerophys., Univ. Toronto, Mar. 1954.

18. Young, Allen E., McCullough, Stuart, and Smith, Richard L.: Power Unit for High-Intensity Light Source. NACA RM E50K27, 1951.

19. Chapman, Dean R., and Rubesin, Morris W.: Temperature and Velocity Profiles in the Compressible Laminar Boundary Layer with Arbitrary Distribution of Surface Temperature. Jour. Aero. Sci., vol. 16, no. 9, Sept. 1949, pp. 547-565.

20. Howes, Walton L., and Buchele, Donald R.: A Theory and Method for Applying Interferometry to the Measurement of Certain Two-Dimensional Gaseous Density Fields. NACA TN 2693, 1952.

21. Charters, Alex C., Jr.: Transition Between Laminar and Turbulent Flow by Transverse Contamination. NACA TN 891, 1943.

22. Carrier, G. F.: The Boundary Layer in a Corner. Quart. Appl. Math., vol. IV, no. 4, Jan. 1947, pp. 367-370.

23. Haefeli, Rudolph C.: Use of Fences to Increase Uniformity of Boundary Layer on Side Walls of Supersonic Wind Tunnels. NACA RM E52E19, 1952.

24. Weltmann, Ruth N., and Kuhns, Perry W.: Density Profiles of Subsonic Boundary Layers on a Flat Plate Determined by X-Ray and Pressure Measurements. NACA TN 3098, 1954.

25. Loos, Henk G.: A Simple Laminar Boundary Layer with Secondary Flow. Jour. Aero. Sci., vol. 22, no. 1, Jan. 1955, pp. 35-40.

26. Hermann, R.: Heat Transfer by Free Convection from Horizontal Cylinders in Diatomic Gases. NACA TM 1366, 1954.

27. Ostrach, Simon: An Analysis of Laminar Free-Convection Flow and Heat Transfer About a Flat Plate Parallel to the Direction of the Generating Body Force. NACA Rep. 1111, 1953. (Supersedes NACA TN 2635.)

28. Wachtell, G. P.: An Evaluation Procedure for Interferometry of Density Fields with Cylindrical Symmetry. Appendix to Optical Studies of Boundary Layer Phenomena on a Flat Plate at Mach Number 2.35 by R. Ladenburg and D. Bershader. Palmer Phys. Lab., Princeton Univ., Dec. 15, 1952. (Contract N6ori-105, Task II.)

29. Weyl, F. Joachim: Analytical Methods in Optical Examination of Supersonic Flow. Navord Rep. 211-45, Dept. Navy, Bur. Ord., Dec. 11, 1945.

30. Kovasznay, Leslie S. G., and Clarken, Patricia C.: Experimental Investigation of Optical Methods for Measuring Turbulence. Tech. Rep. No. 42, Proj. Squid, Johns Hopkins Univ., Jan. 1, 1952. (Office Naval Res., Dept. Navy, Res. and Dev. Command, Dept. Air Force Contract N6ori-105, Task Order III, NR-098-038.)

31. Kinsler, Martin R.: Influence of Refraction on the Applicability of the Zehnder-Mach Interferometer to Studies of Cooled Boundary Layers. NACA TN 2462, 1951.

32. Jenkins, Francis A., and White, Harvey E.: Fundamentals of Physical Optics. First ed., McGraw-Hill Book Co., Inc., 1937, pp. 401-405.

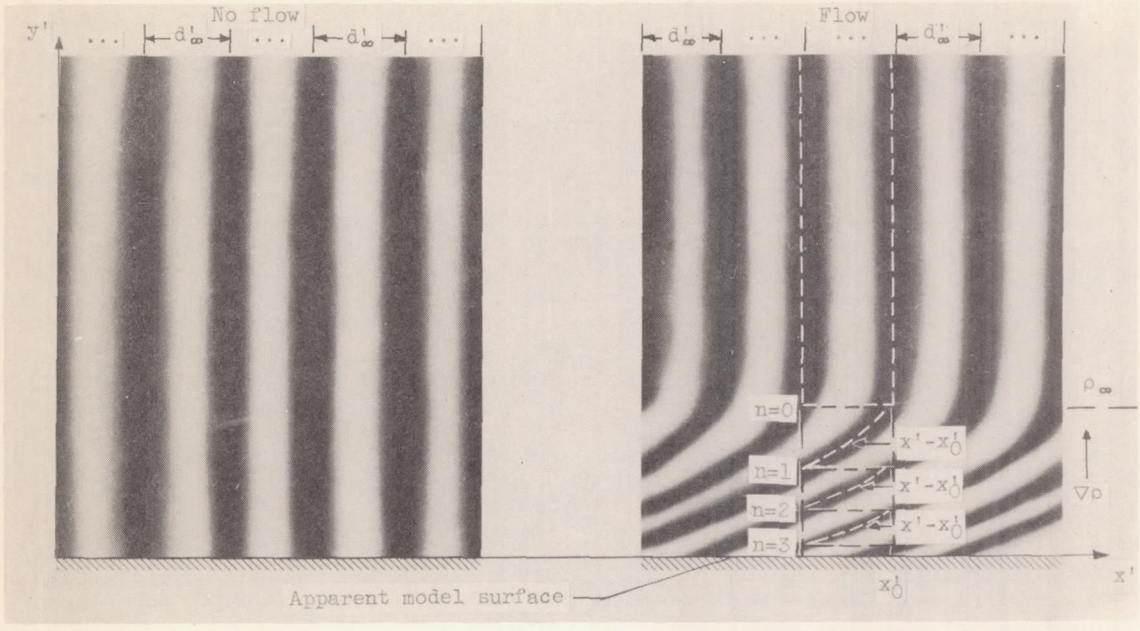

(a) Orientation of fringes parallel to grad ρ.

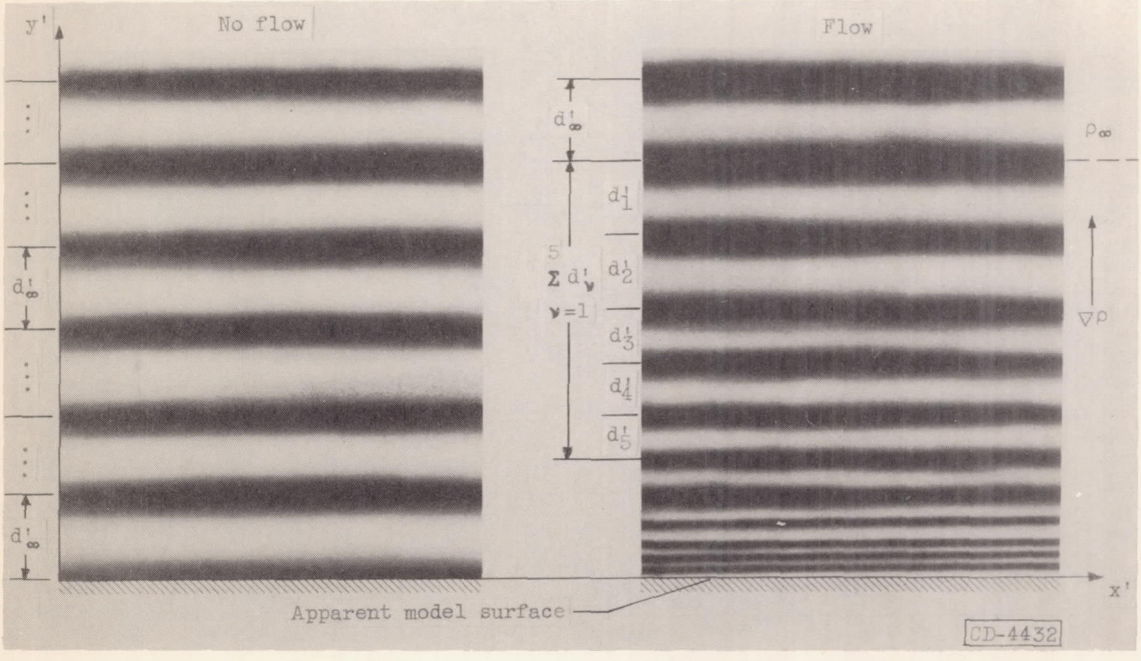

(b) Orientation of fringes perpendicular to grad ρ.

Figure 1. - Interference-fringe orientation.

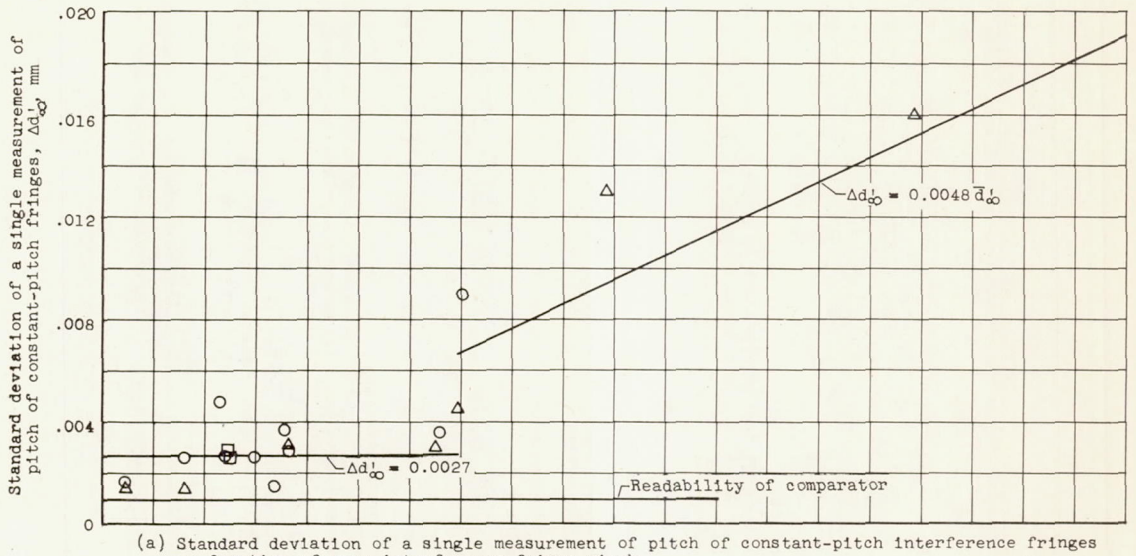

(a) Standard deviation of a single measurement of pitch of constant-pitch interference fringes as a function of mean interference-fringe pitch.

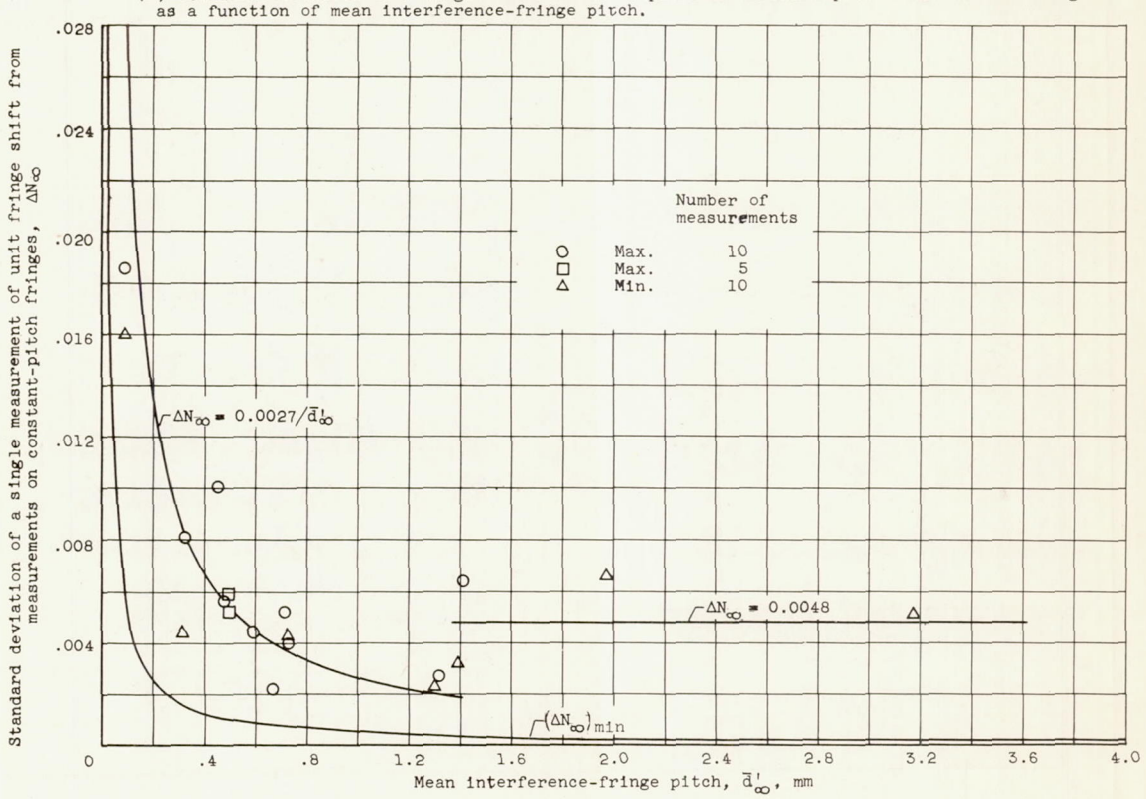

(b) Standard deviation of a single measurement of unit fringe shift from measurements on constant-pitch interference fringes as function of mean interference-fringe pitch.

Figure 2. - Error in measuring fringe shift.

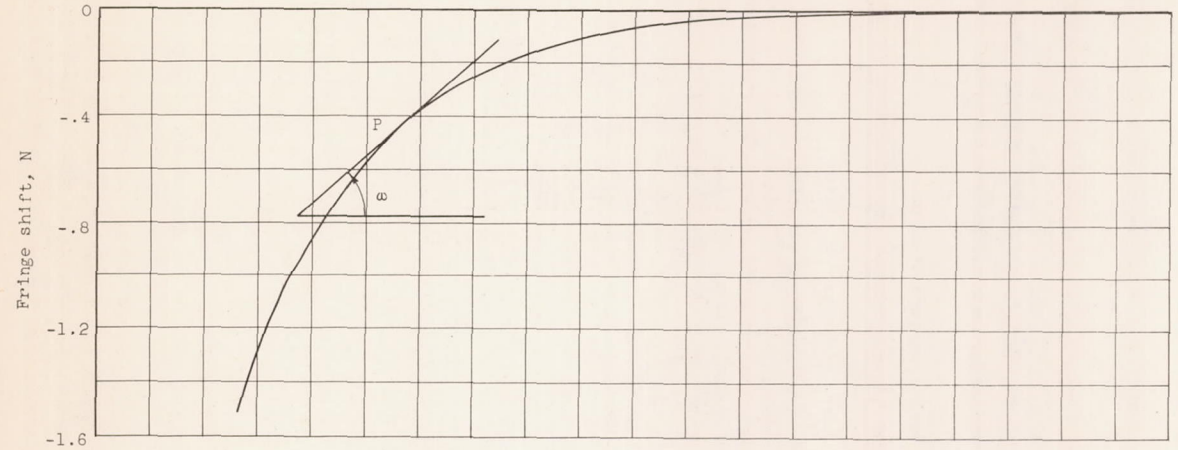

(a) Hypothetical fringe-shift profile N_D (ref. 1).

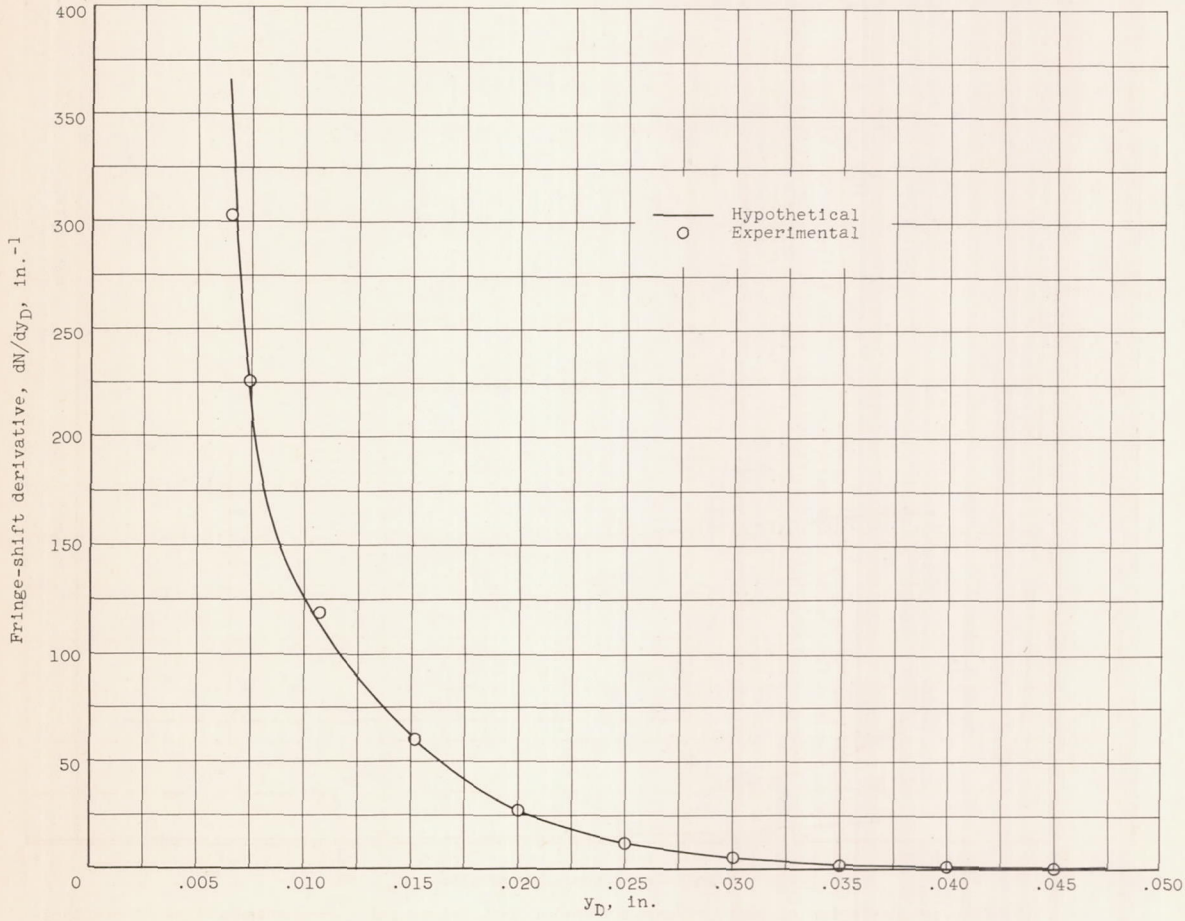

(b) Comparison of hypothetical (ref. 1) and optically measured profiles dN_D/dy_D.

Figure 3. - Comparison of hypothetical and measured profiles dN_D/dy_D.

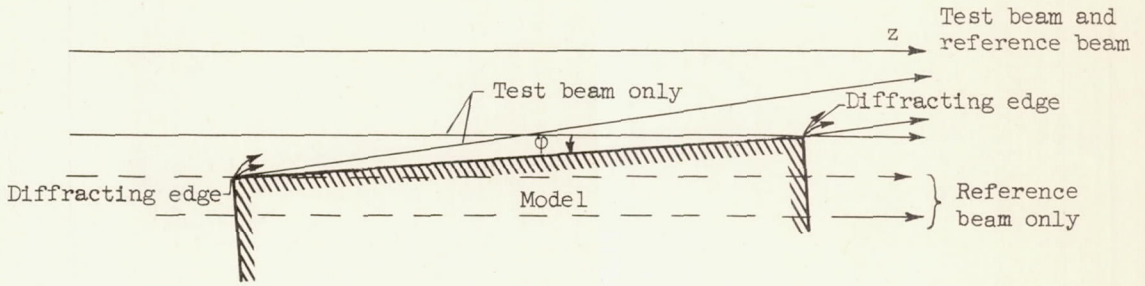

(a) $\varphi < 0$.

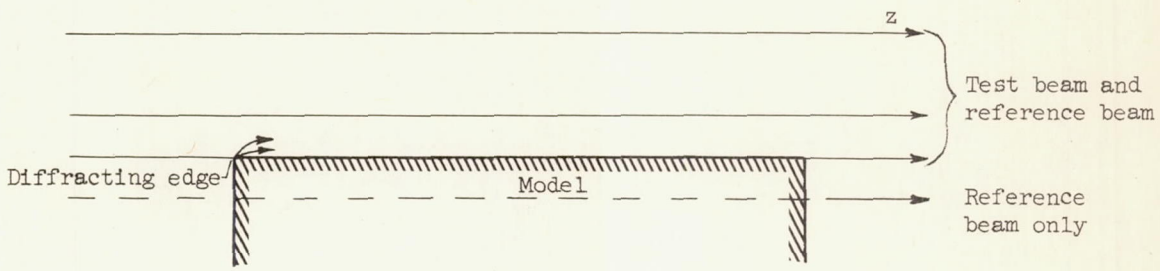

(b) $\varphi = 0$.

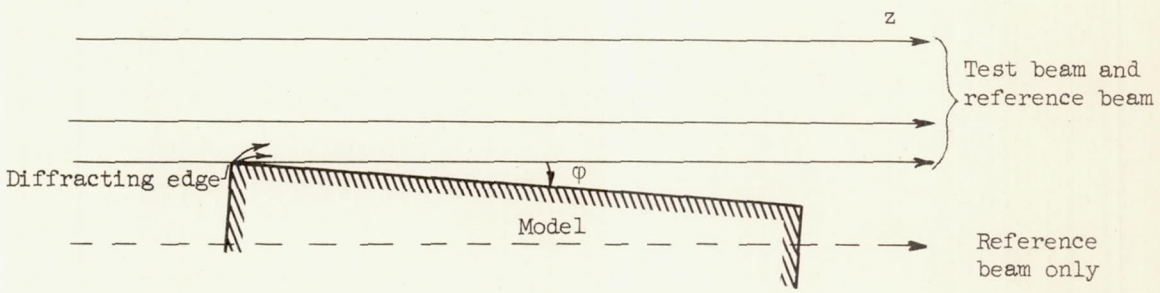

(c) $\varphi > 0$.

Figure 4. - Ray-trace orientations.

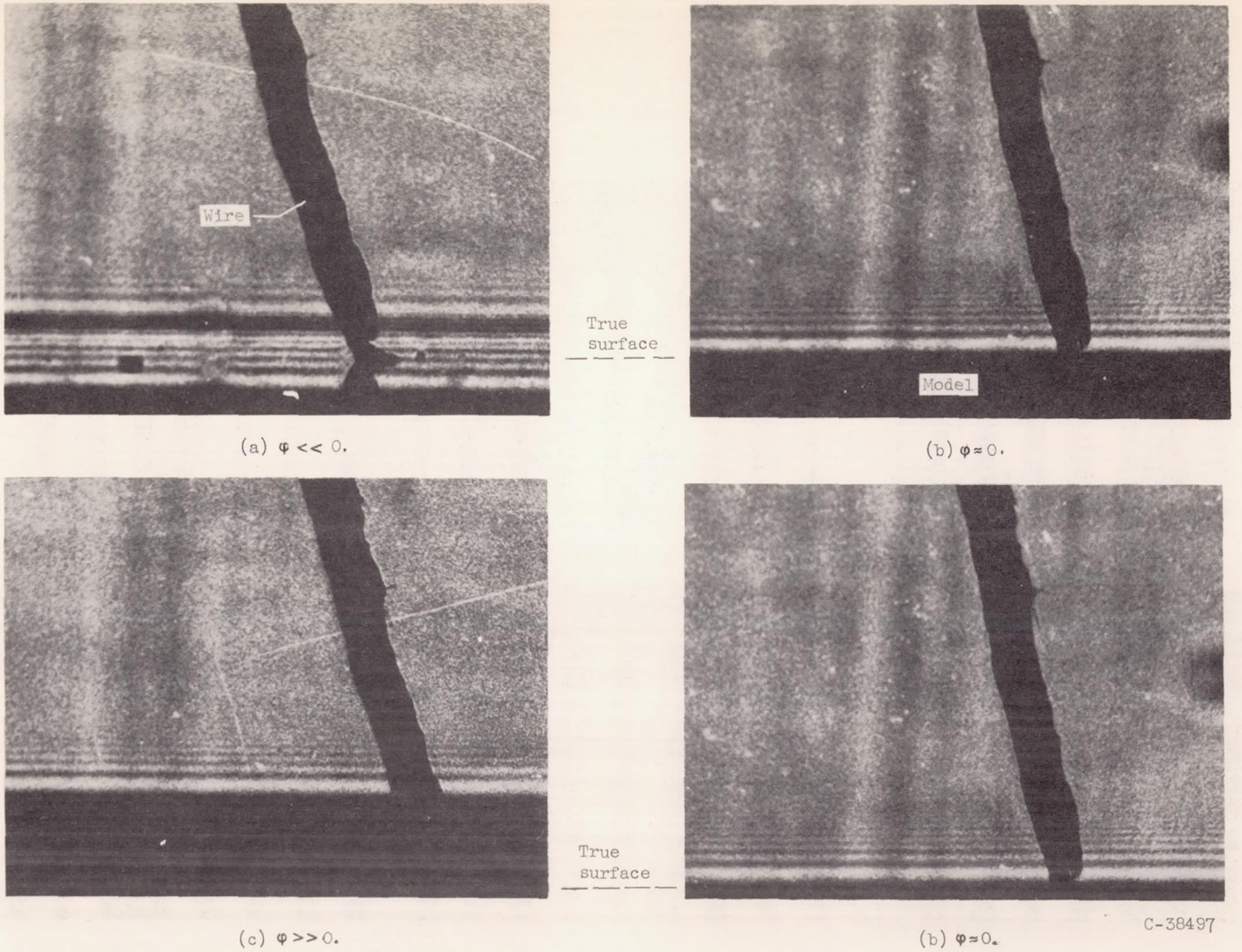

(a) $\varphi << 0$.

(b) $\varphi \approx 0$.

(c) $\varphi >> 0$.

(b) $\varphi \approx 0$.

C-38497

Figure 5. - Surface effects, test beam only. Fraction or test-section span K, 1/2; magnification, X28.

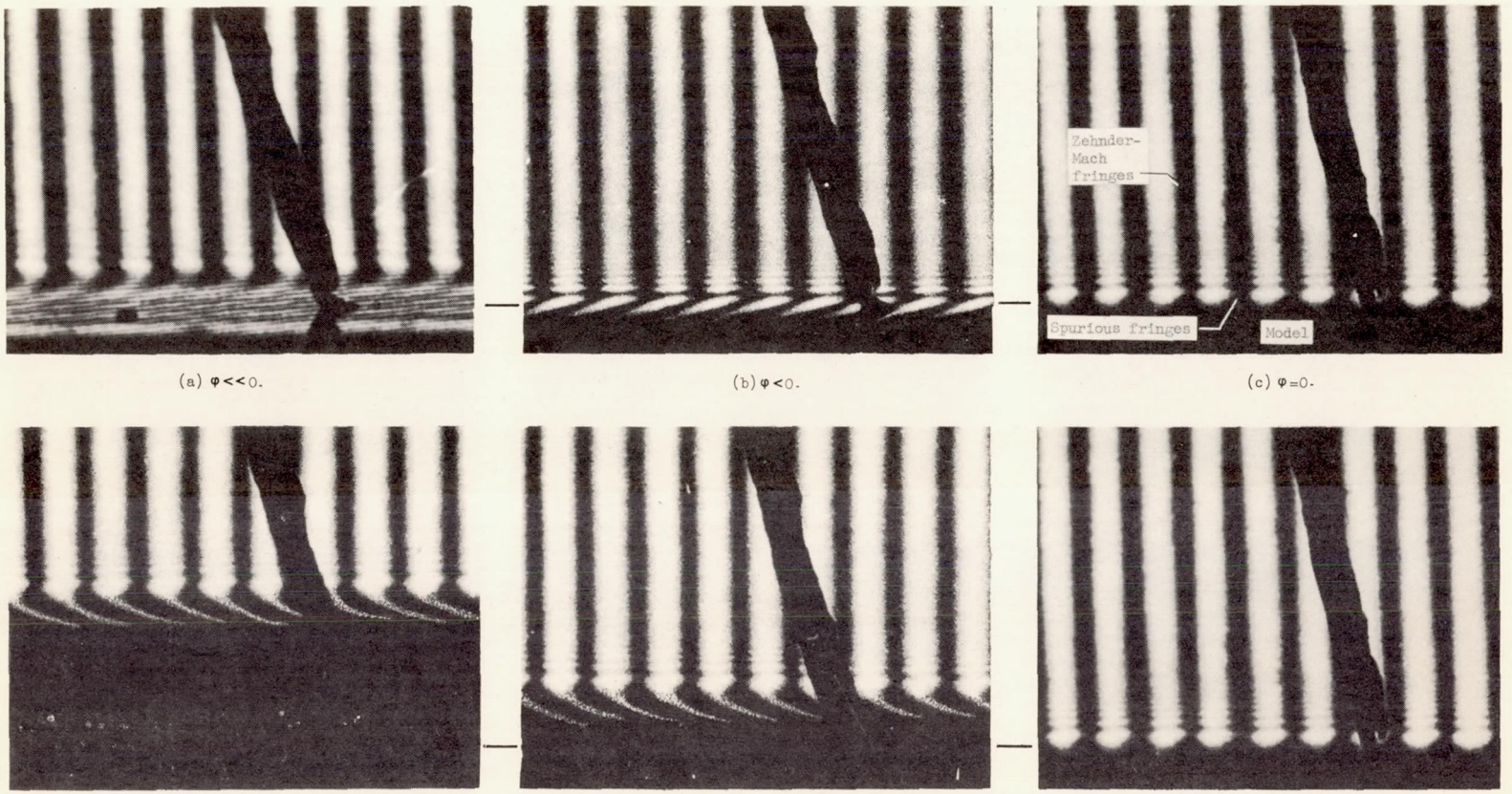

Figure 6. - Spurious fringes, both beams. Fraction of test-section span K, 1/2; magnification, X19.

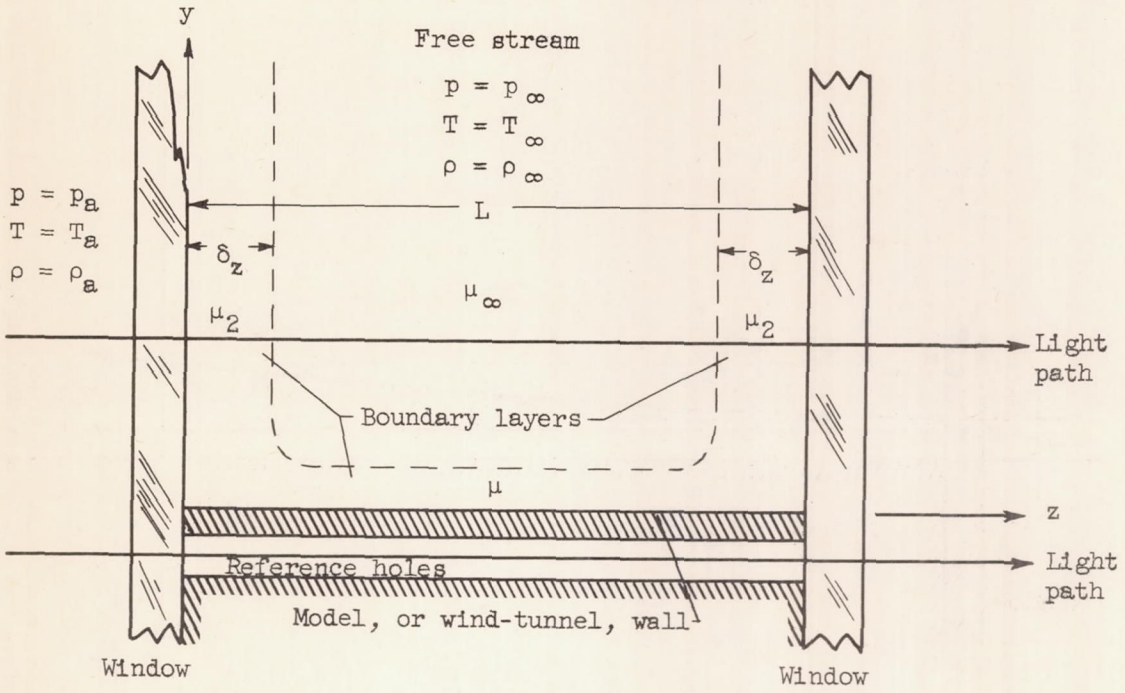

(a) Cross section.

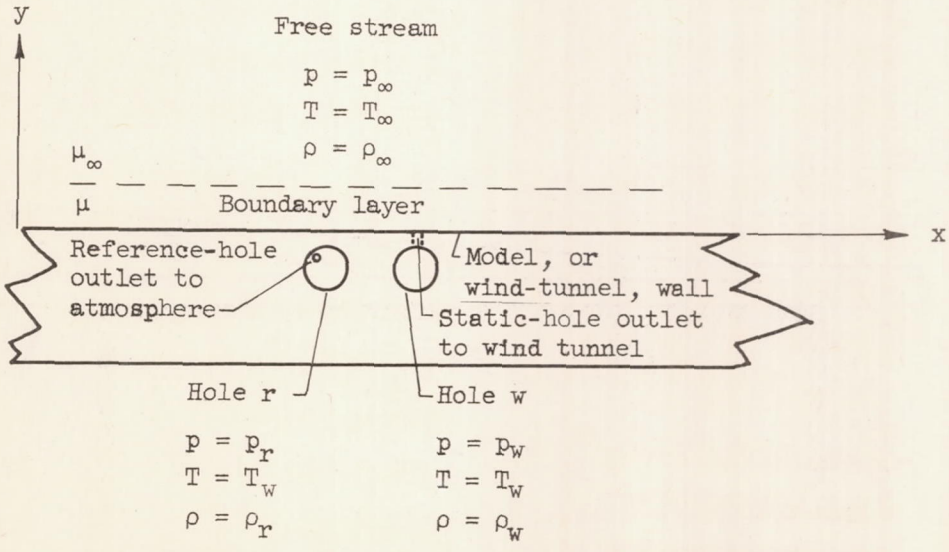

(b) Longitudinal section.

Figure 7. - Wind-tunnel geometry for determining end corrections.

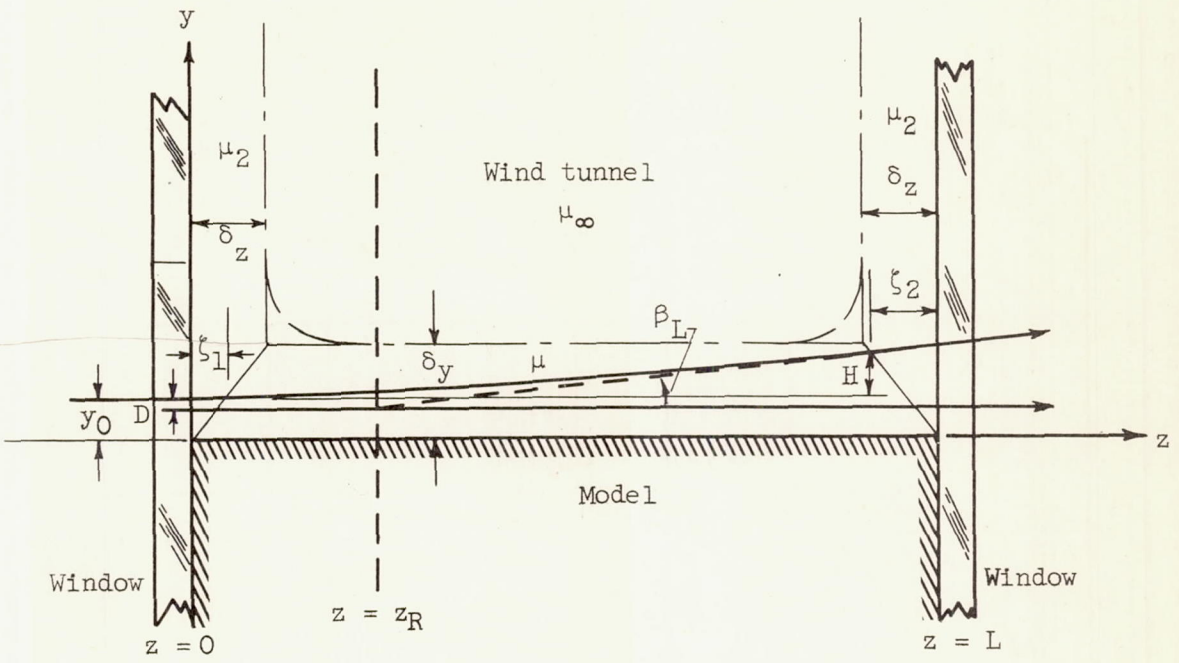

Figure 8. - Ray traces in proximity to model contained in wind tunnel.

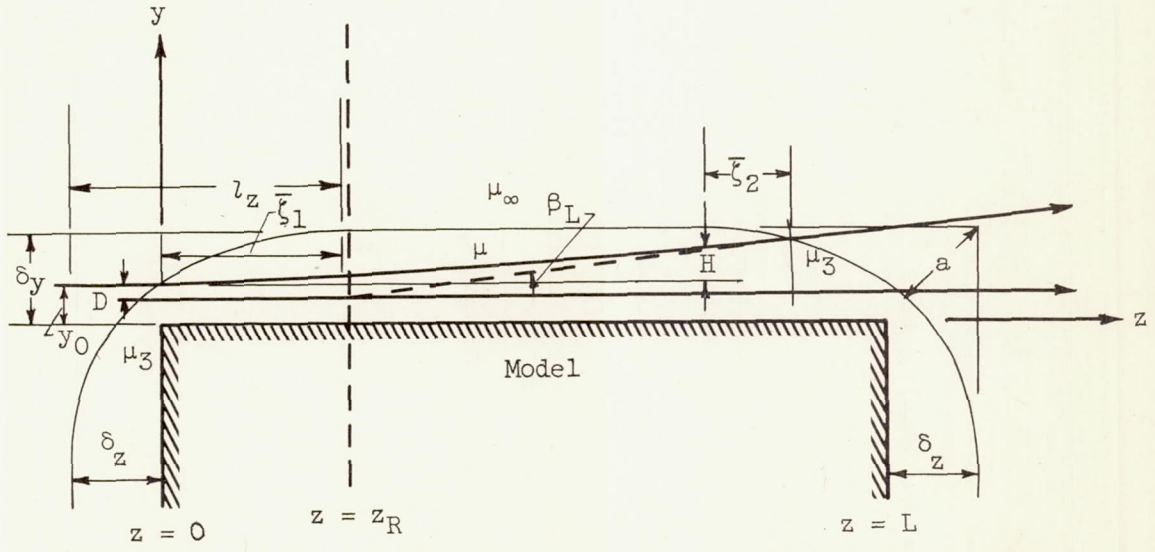

Figure 9. - Ray traces in proximity to model not contained in wind tunnel.

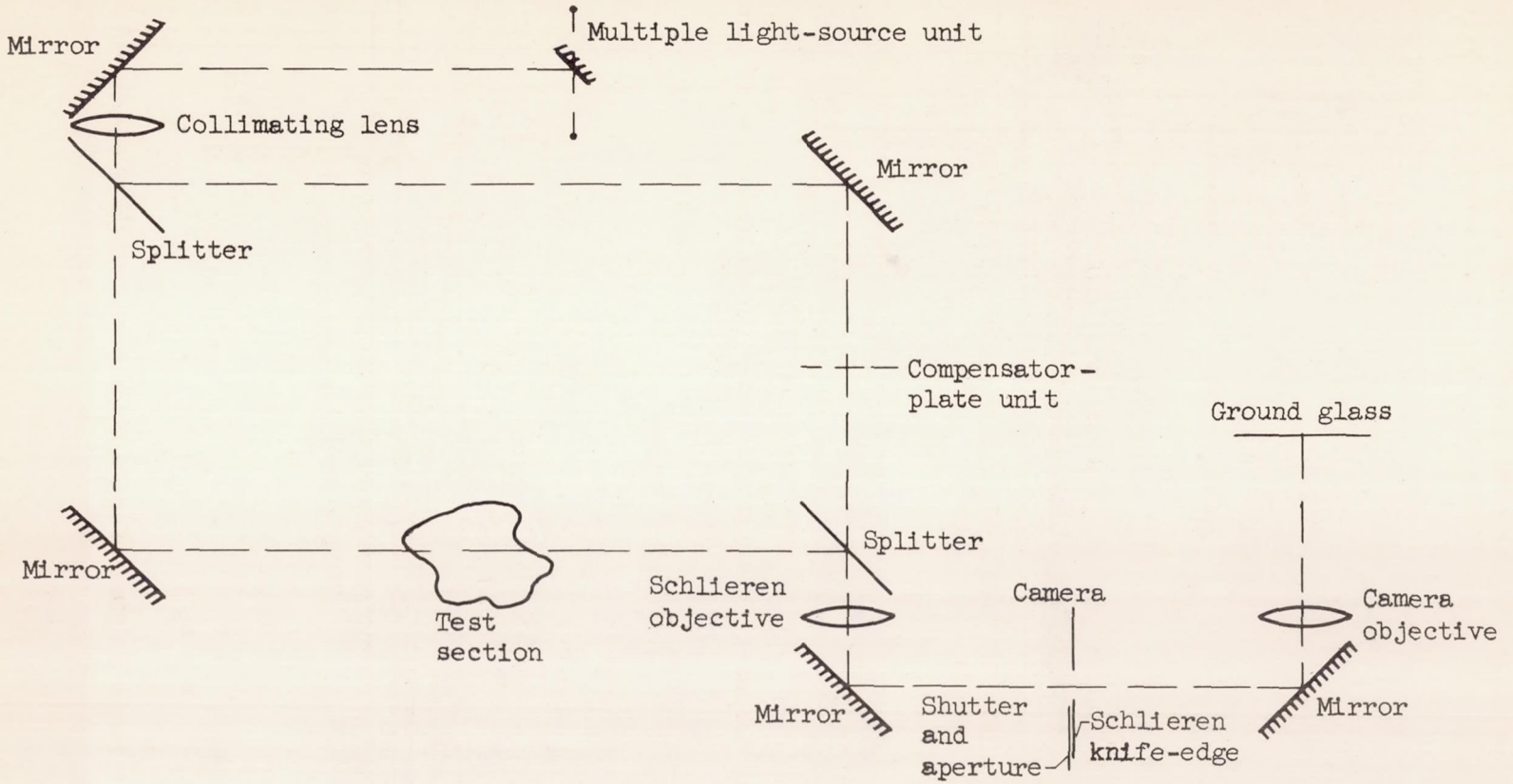

Figure 10. - NACA 6-inch Zehnder-Mach interferometer with schlieren provision and afocal camera-lens system.

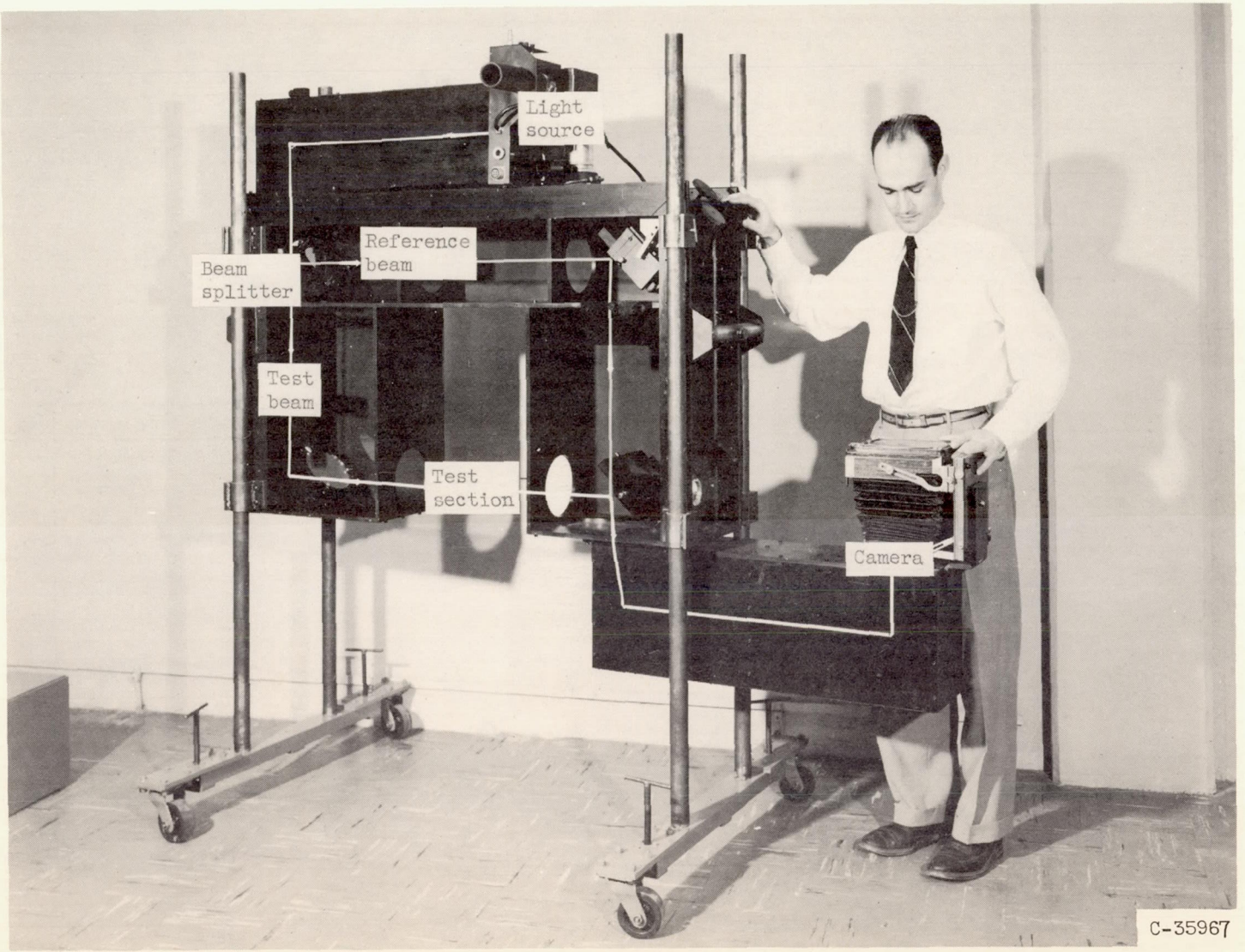

Figure 11. - NACA 6-inch Zehnder-Mach interferometer (side plate removed).

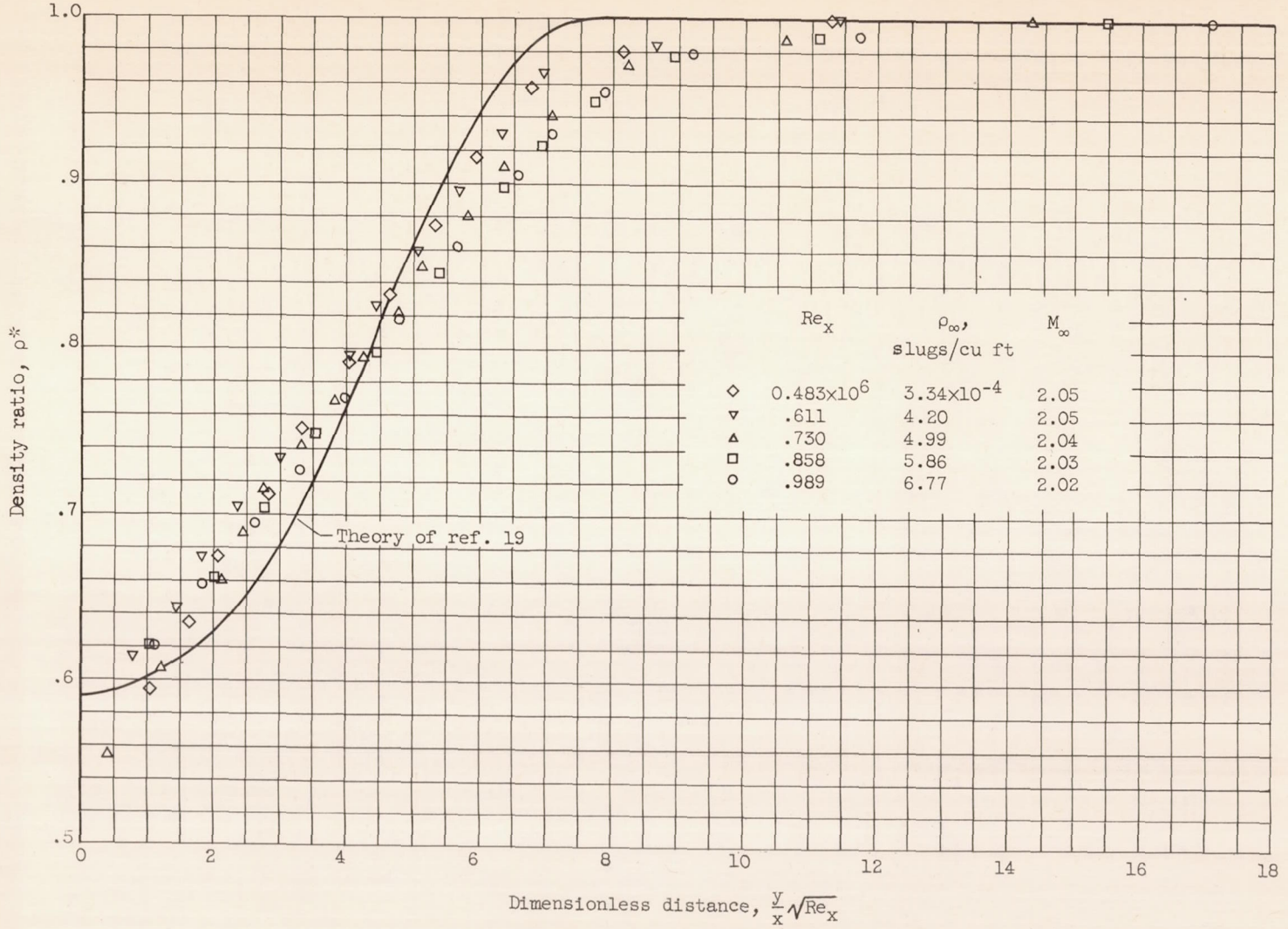

(a) Density profiles; x = 2.5 inches.

Figure 12. - Measurements of laminar boundary layer associated with supersonic flow along an insulated flat plate.

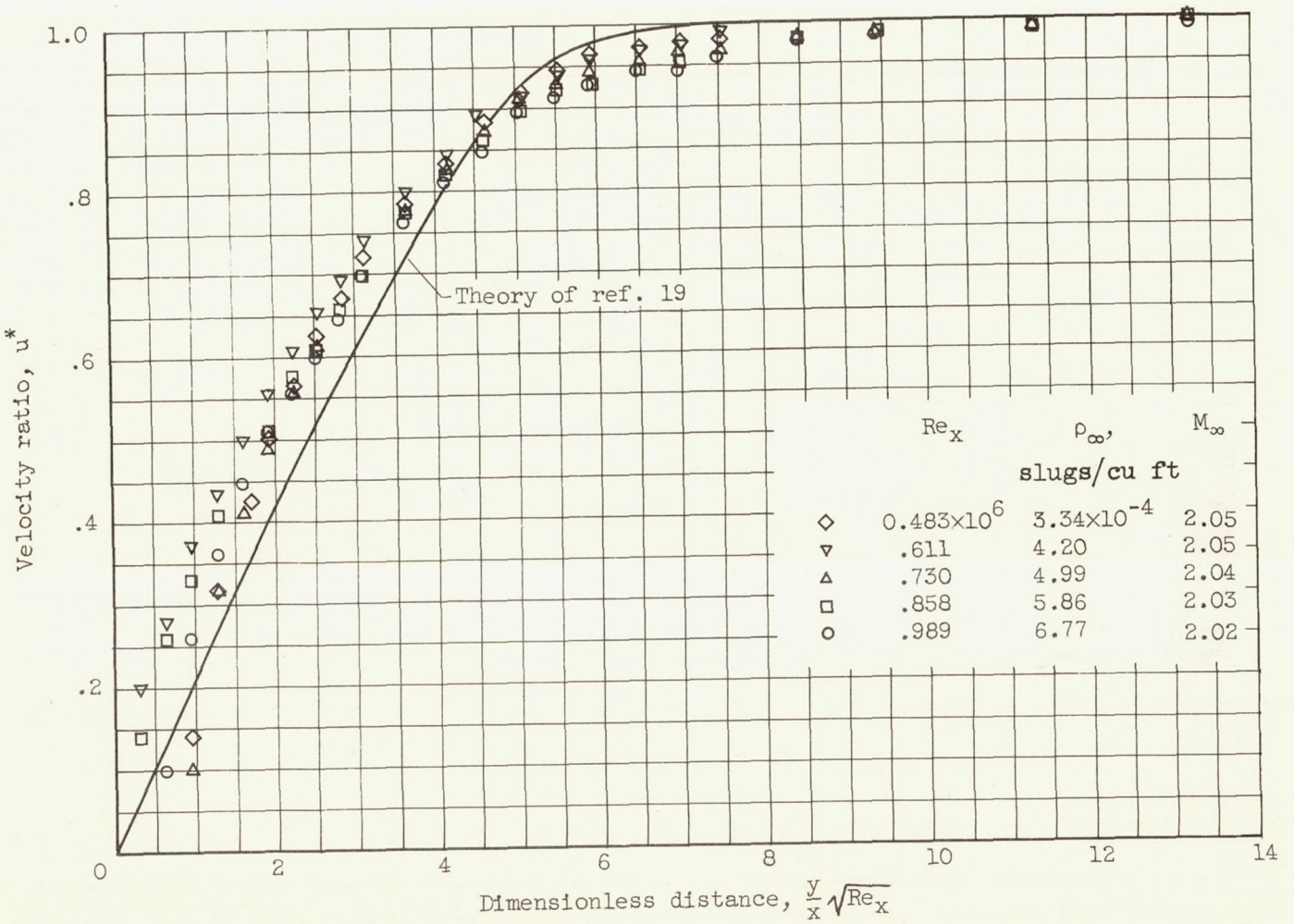

(b) Velocity profiles; x = 2.5 inches.

Figure 12. - Continued. Measurements of laminar boundary layer associated with supersonic flow along an insulated flat plate.

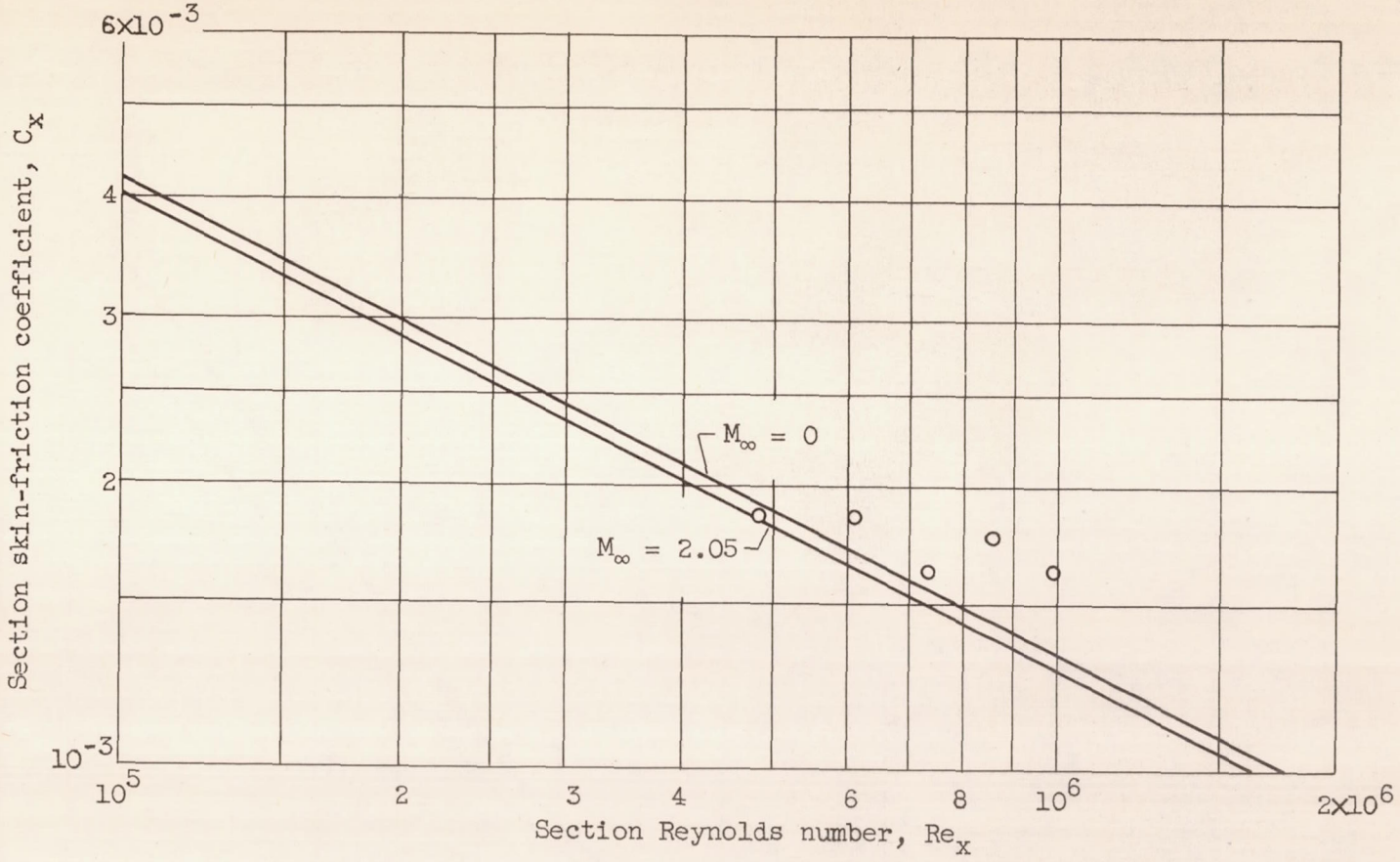

(c) Section skin-friction coefficient as function of section Reynolds number.

Figure 12. - Concluded. Measurements of laminar boundary layer associated with supersonic flow along an insulated flat plate.

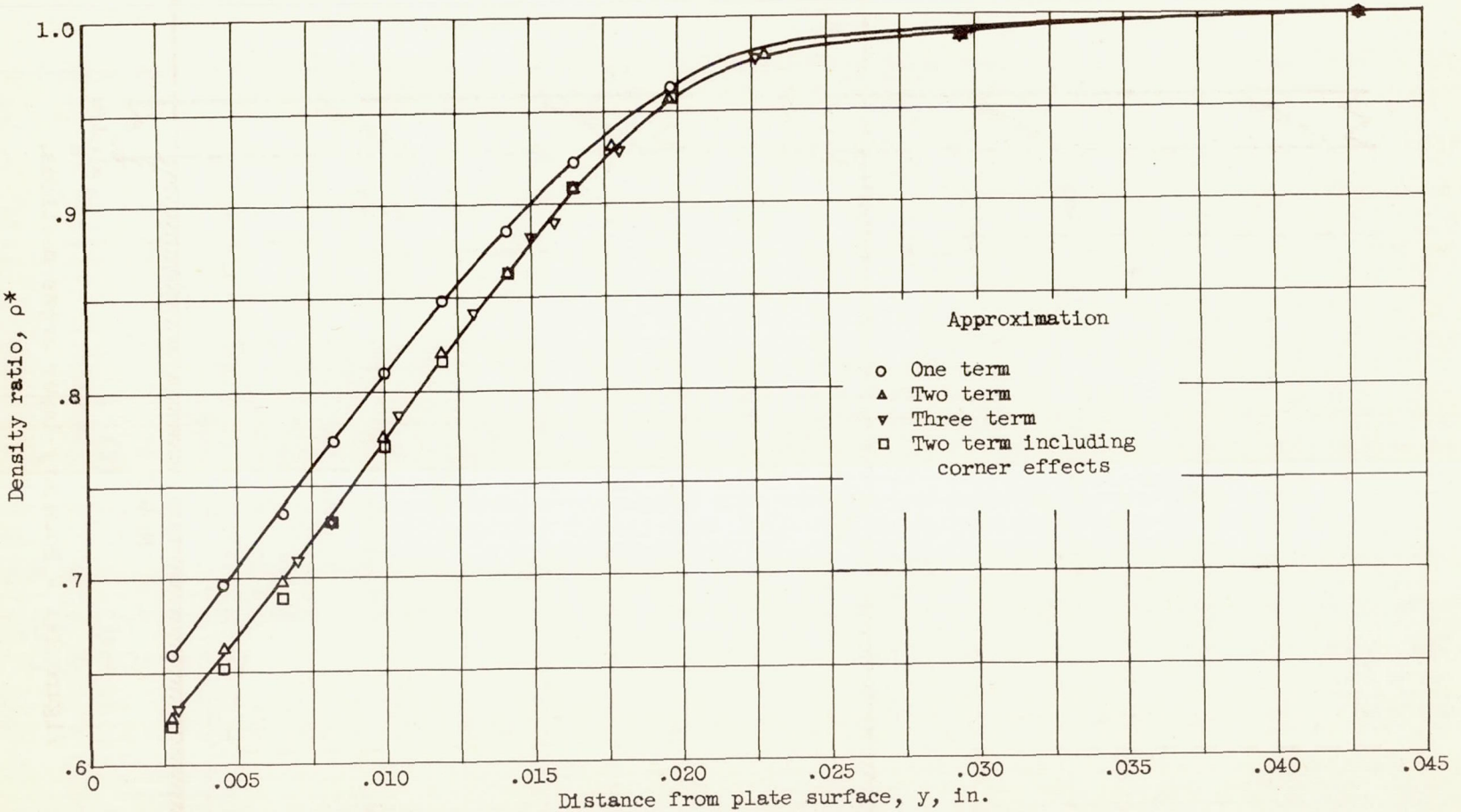

Figure 13. - Comparison of successive approximations of density profile in flat-plate boundary layer (supersonic flow). $Re_x = 0.989 \times 10^6$.

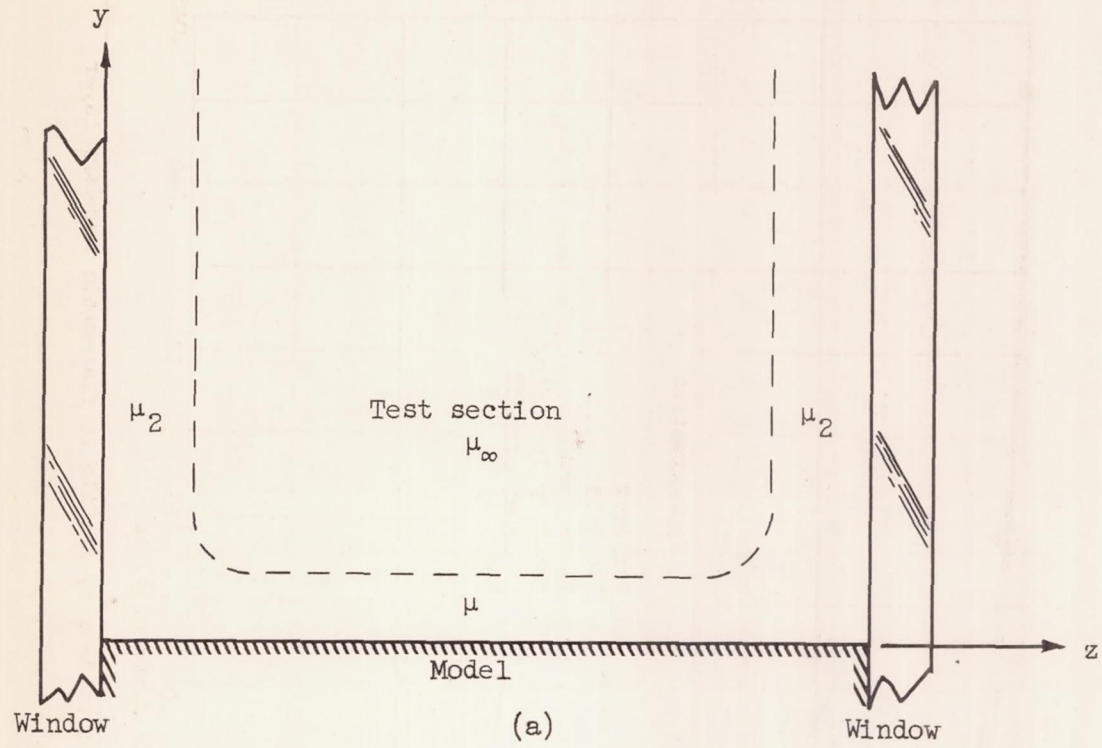

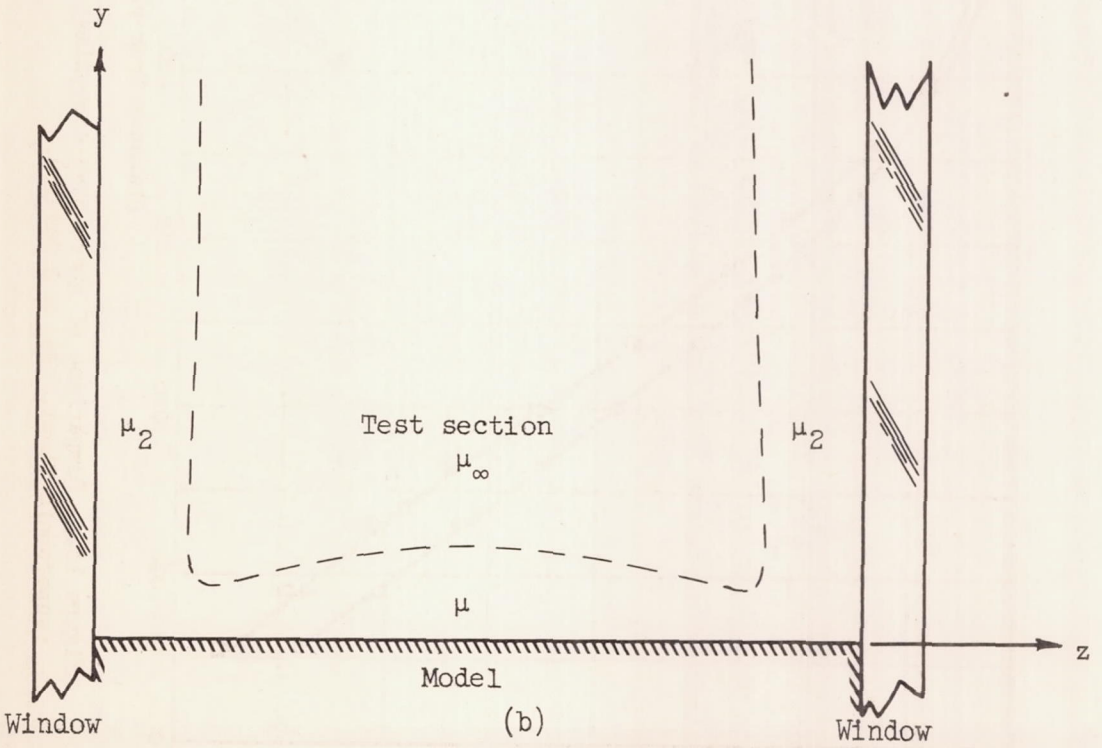

Figure 14. - Boundary-layer cross sections.

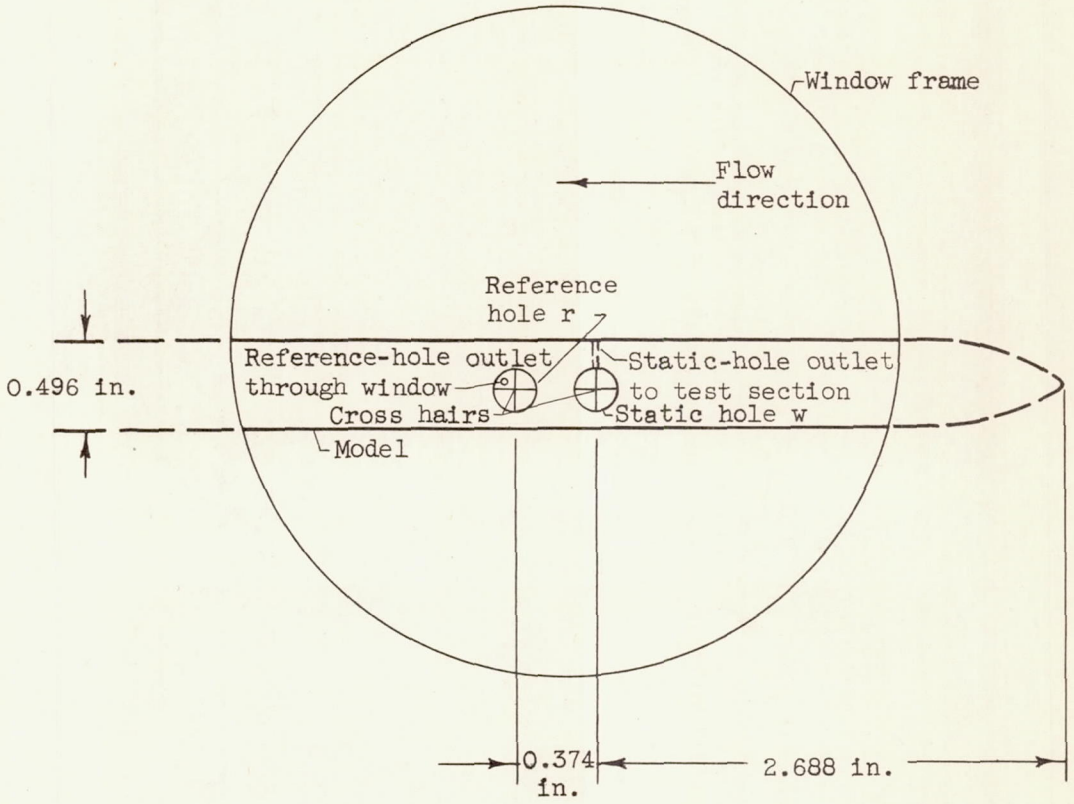

Figure 15. - Details of flat-plate model used in subsonic-flow experiment (ref. 24).

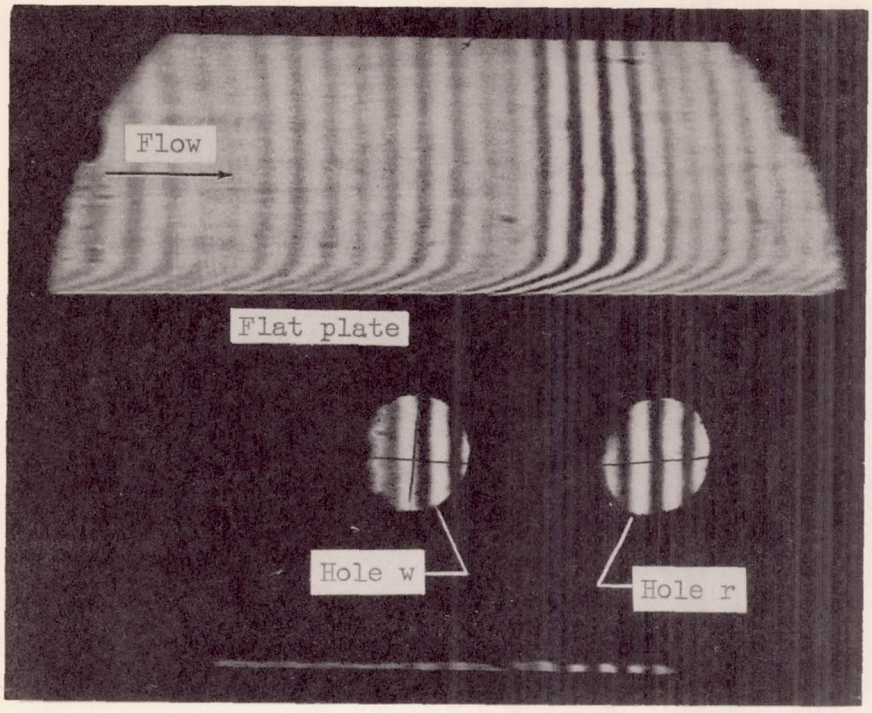

(a) Unfiltered mercury light.

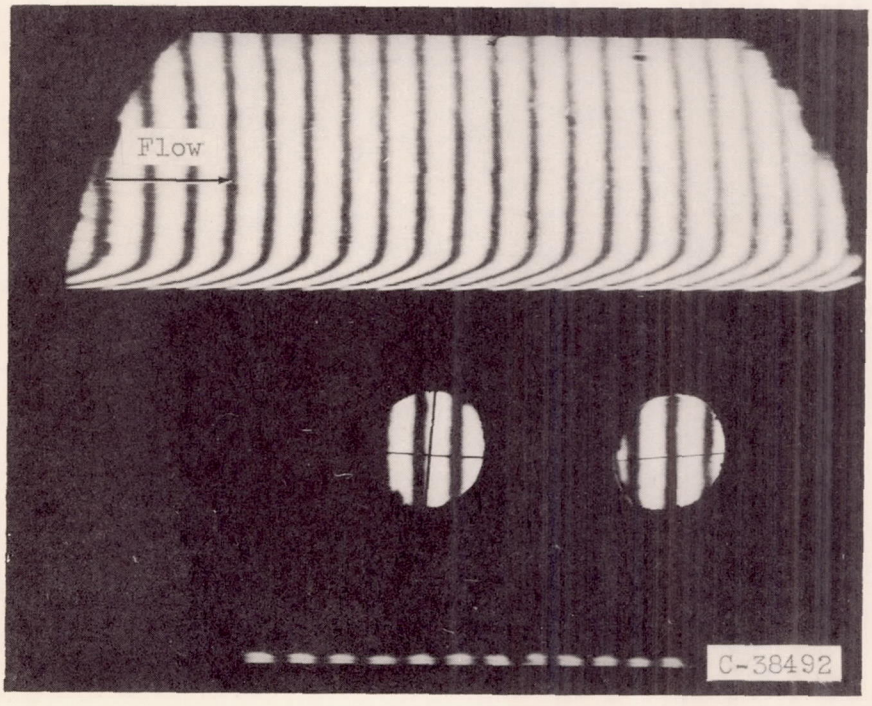

(b) Filtered mercury light (λ = 5461 Å).

Figure 16. - Typical interferograms of boundary layer induced by subsonic flow along flat plate.

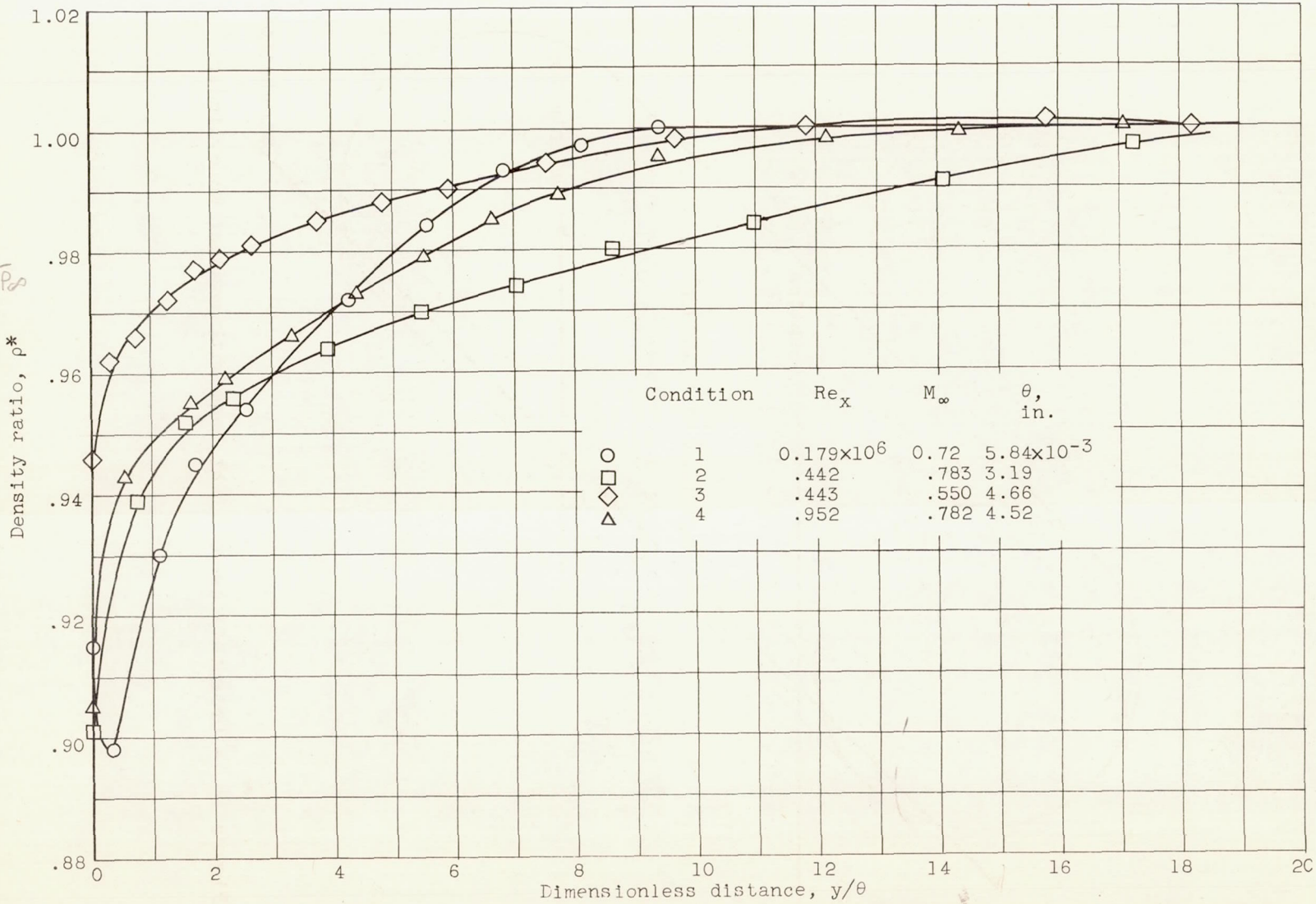

Figure 17. - Subsonic air flow along a flat plate. Composite of measured boundary-layer density profiles.

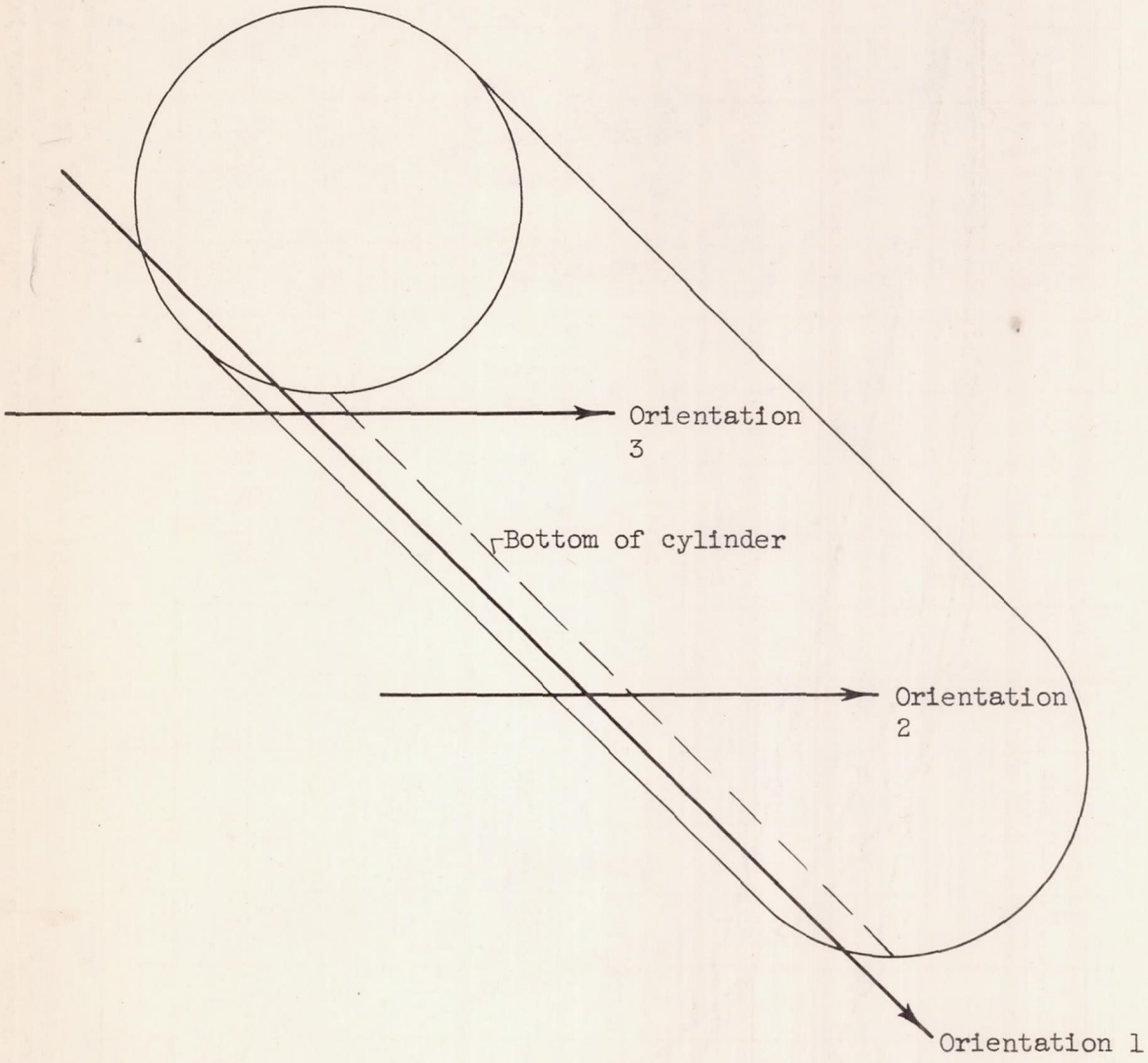

Figure 18. - Orientations of light beam with respect to cylinder.

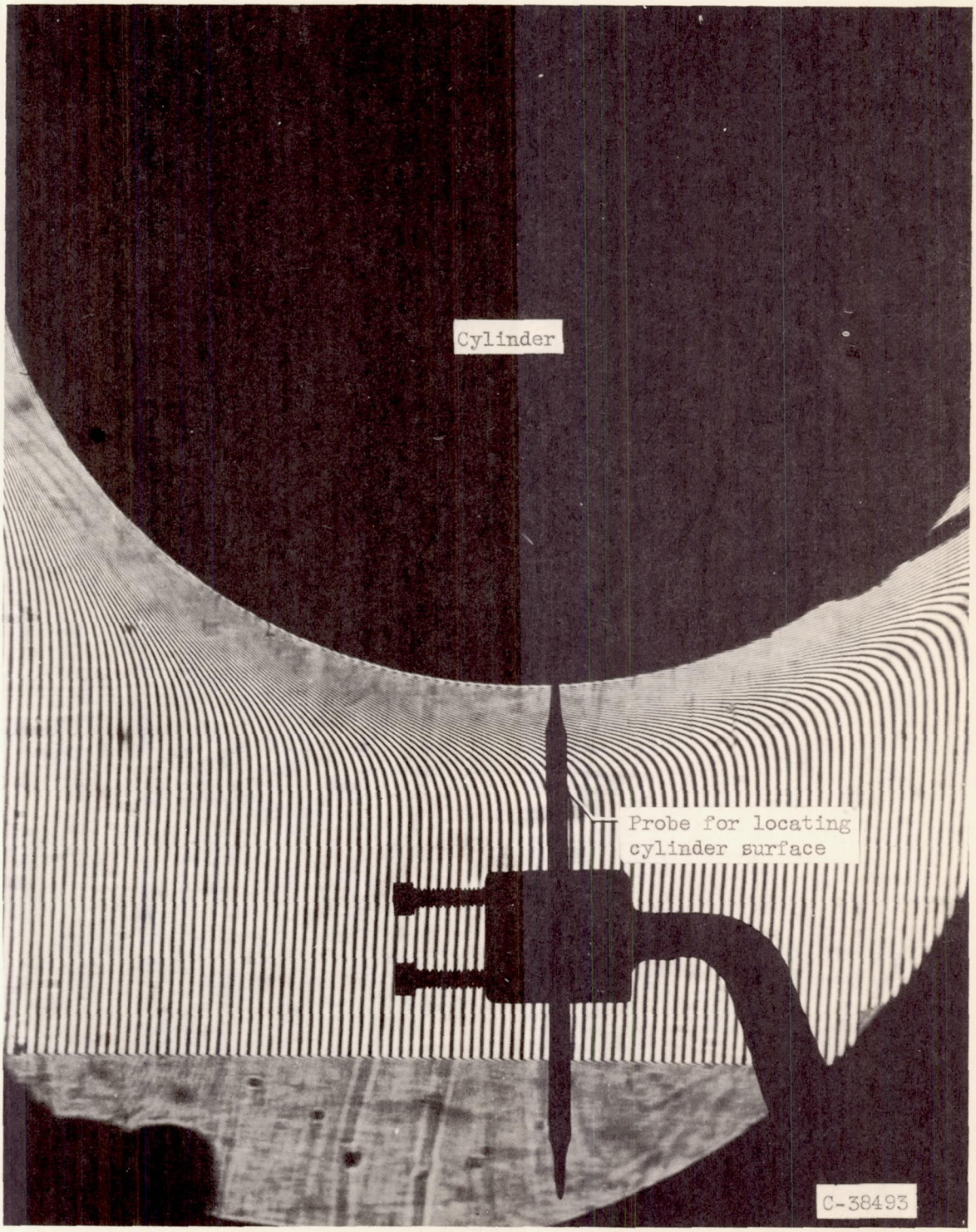

(a) Orientation 1: Light propagation parallel to cylinder axis.

Figure 19. - Typical interferograms of heated horizontal cylinder.

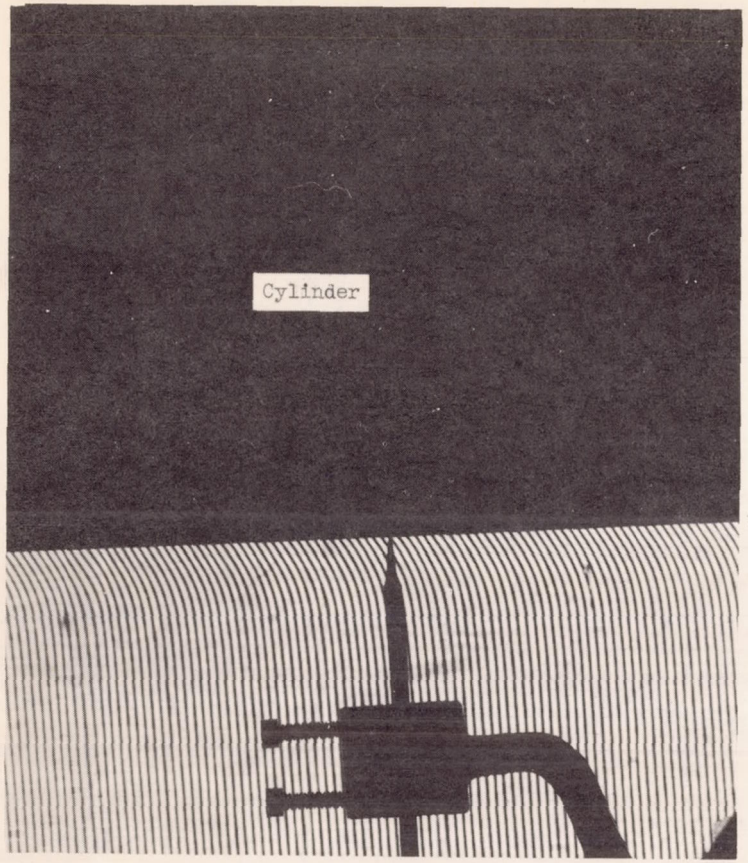

(b) Orientation 2: Light propagation perpendicular to cylinder axis at midlength plane.

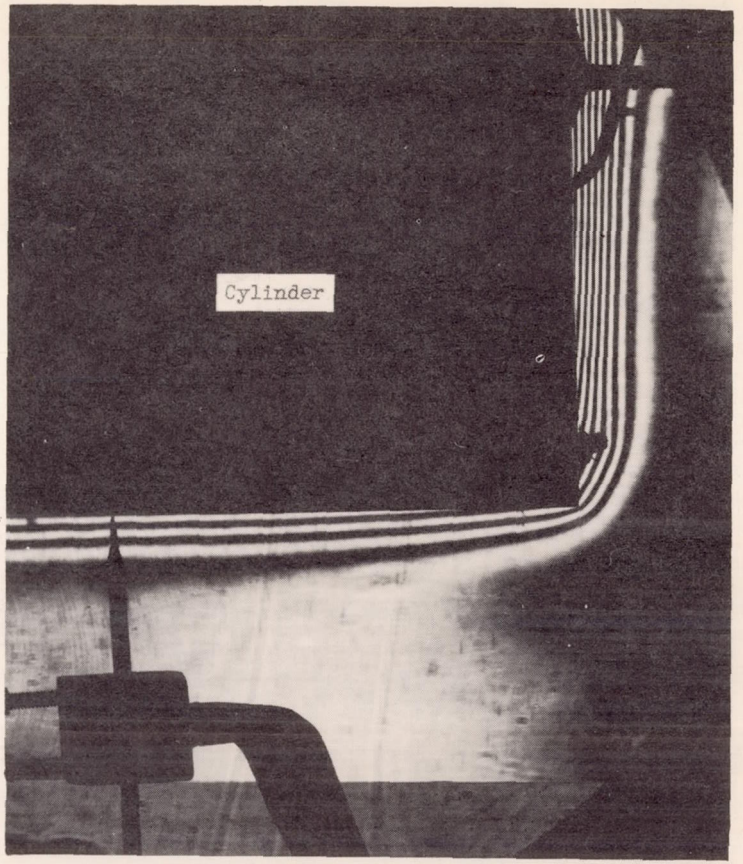

C-38494

(c) Orientation 3: Light propagation perpendicular to cylinder axis at end plane.

Figure 19. - Concluded. Typical interferograms of heated horizontal cylinder.

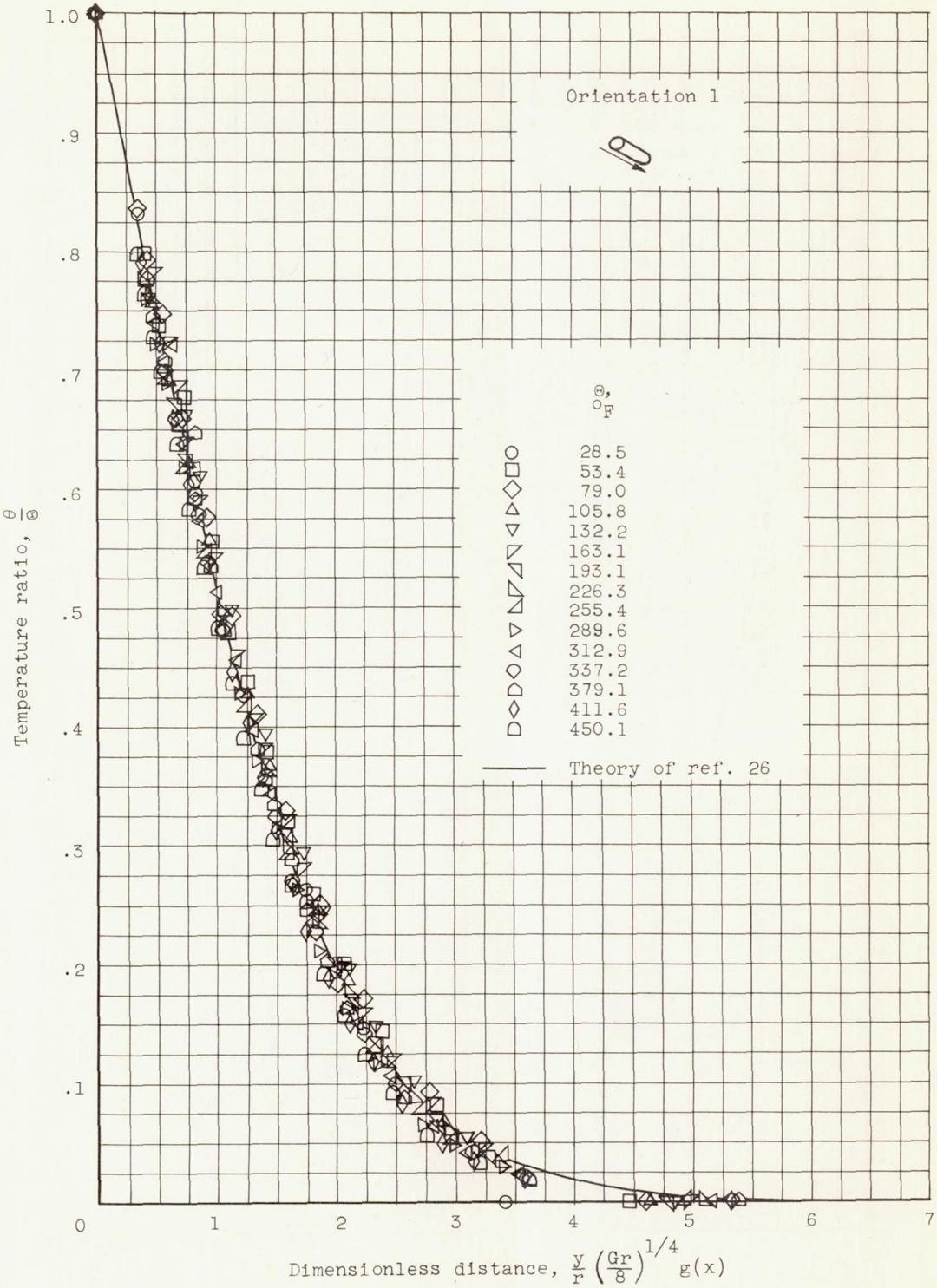

(a) Two-term approximation including corner corrections; K = 1/2; $\overline{T}_\infty$ = 83.3° F; ν based on T_w.

Figure 20. - Dimensionless temperature profiles beneath horizontal circular cylinder.

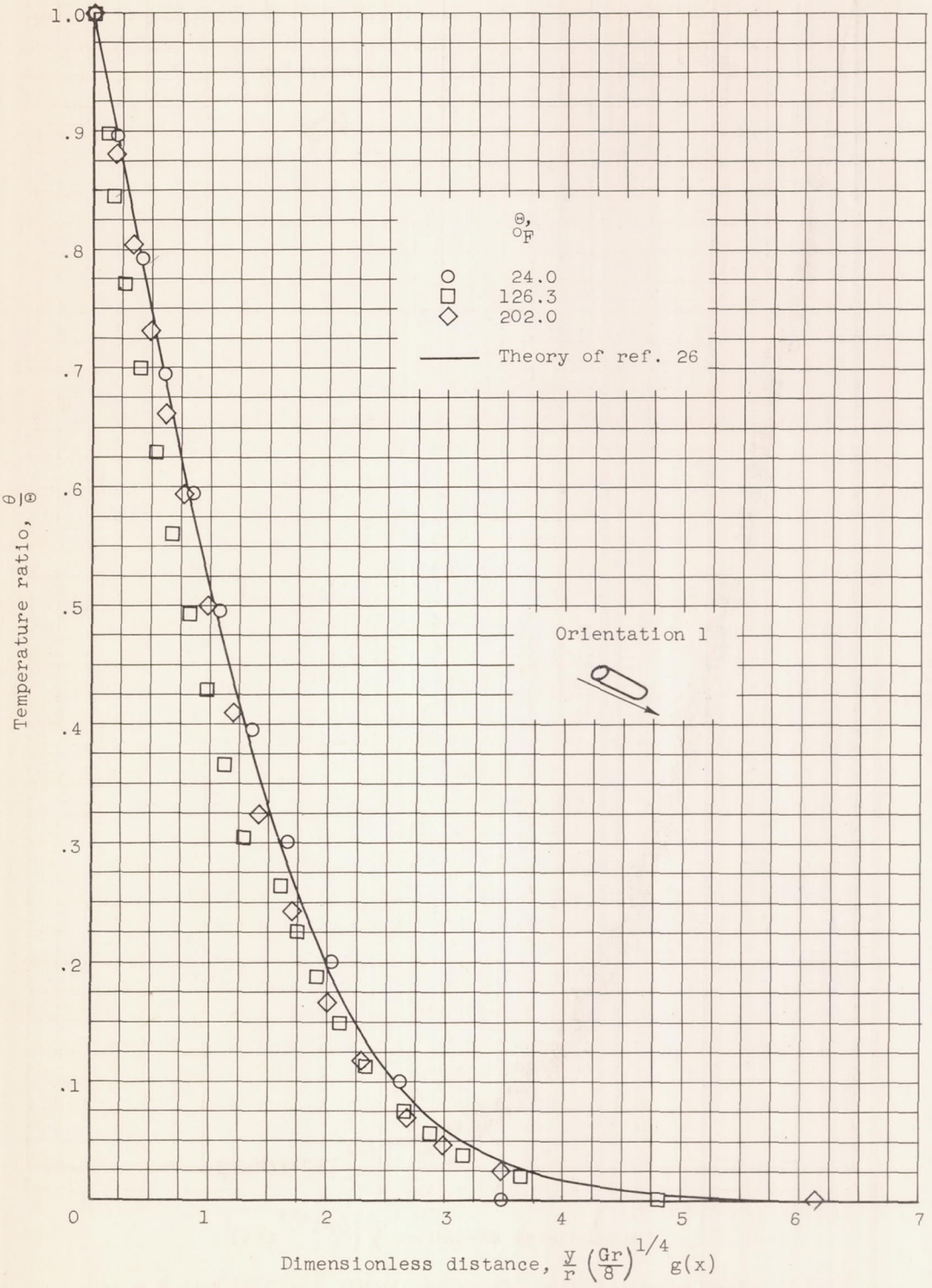

(b) Wachtell-DeFrate method (refs. 2 and 3); $K = 1/3$; $\overline{T}_\infty = 80.2^\circ$ F; ν based on T_w.

Figure 20. - Continued. Dimensionless temperature profiles beneath horizontal circular cylinder.

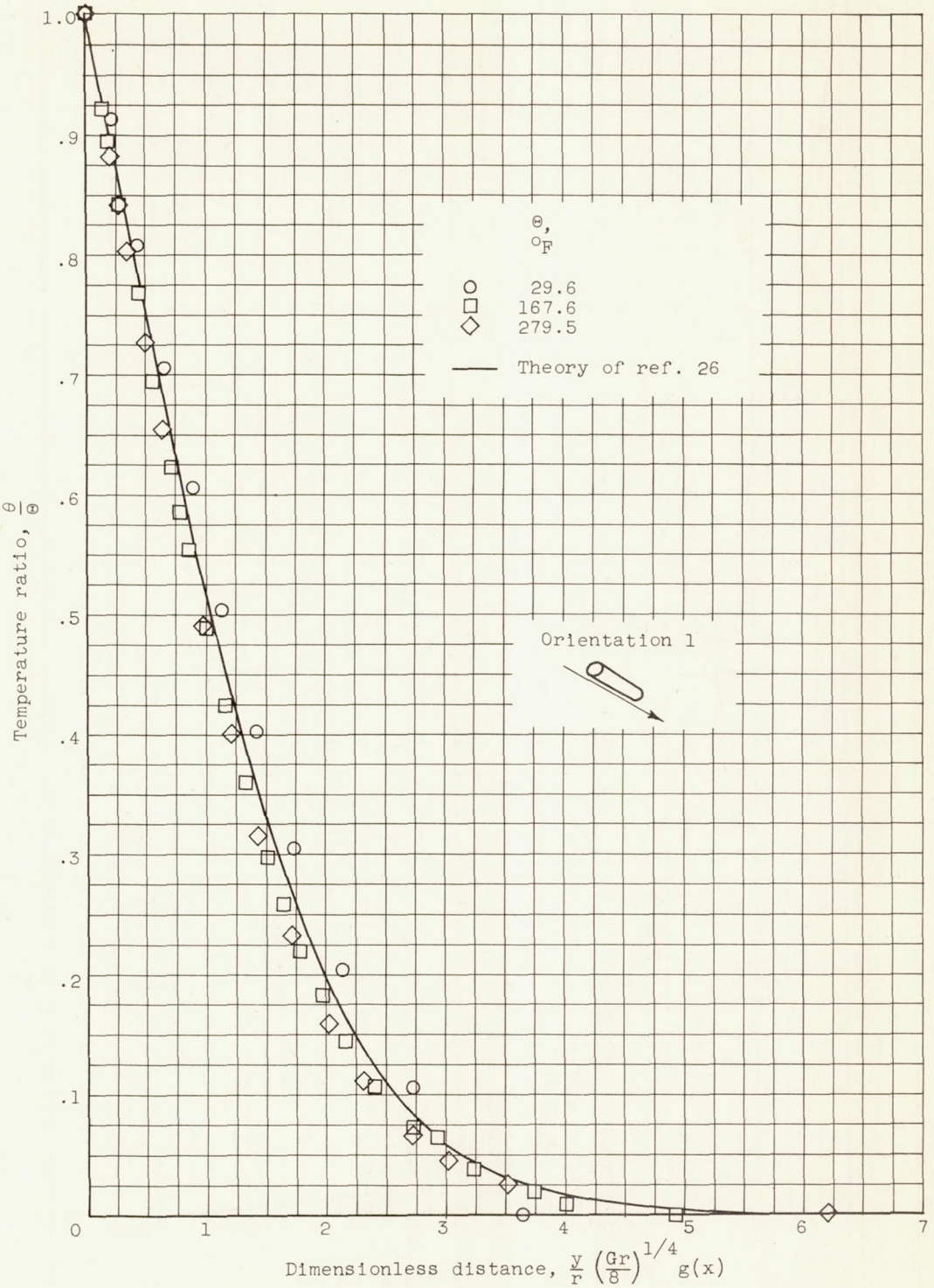

(c) Two-term approximation including corner corrections; K = 1/3; T_∞ = 80.2° F; ν based on T_W.

Figure 20. - Continued. Dimensionless temperature profiles beneath horizontal circular cylinder.

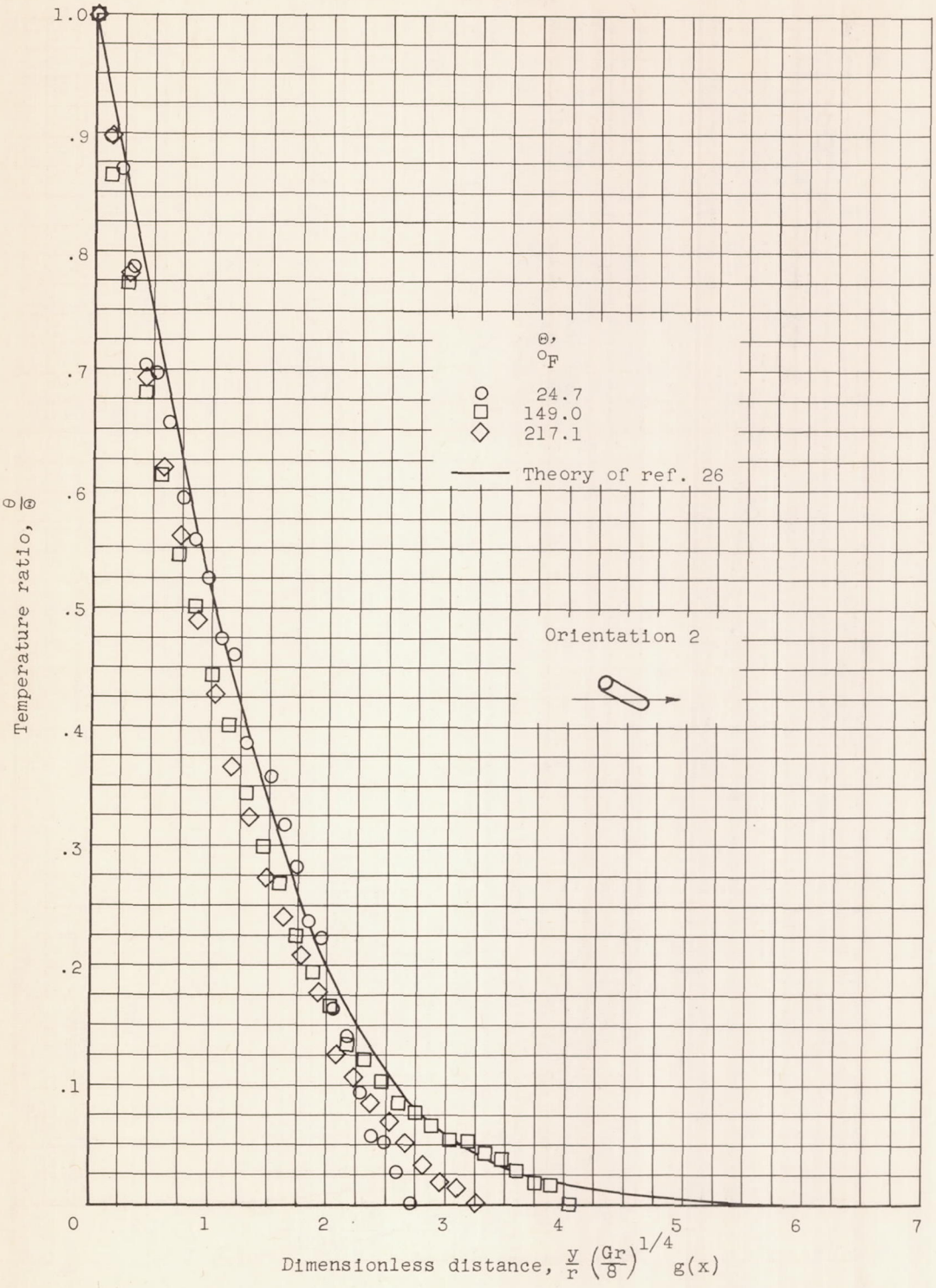

(d) Van Voorhis-Wachtell method (refs. 29 and 2); $\bar{T}_\infty$ = 79.9° F; ν based on T_w.

Figure 20. - Concluded. Dimensionless temperature profiles beneath horizontal circular cylinder.

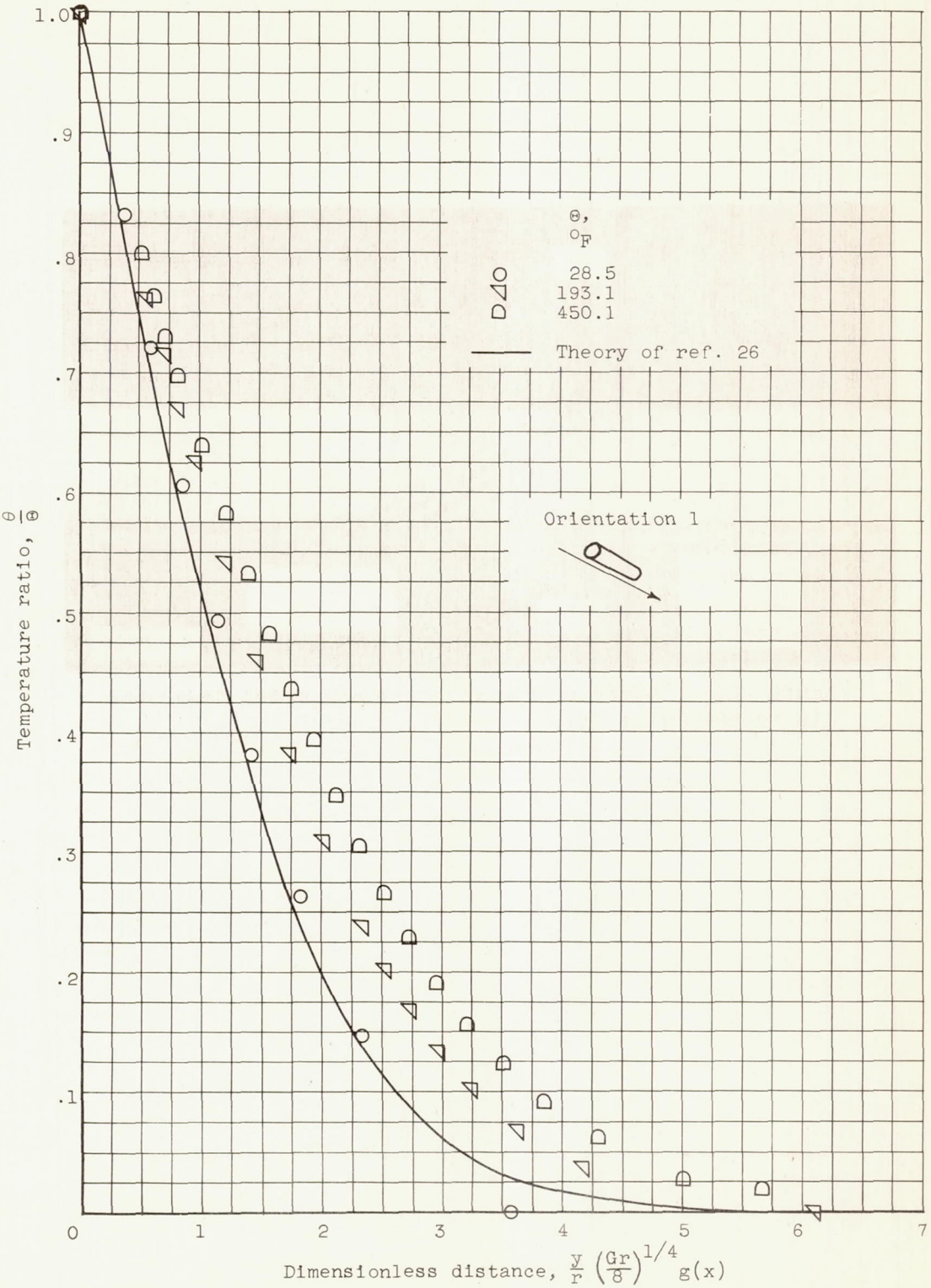

Figure 21. - Dimensionless temperature profiles beneath horizontal circular cylinder. $K = 1/2$; $\bar{T}_\infty = 83.3^\circ$ F; ν based on T_∞.

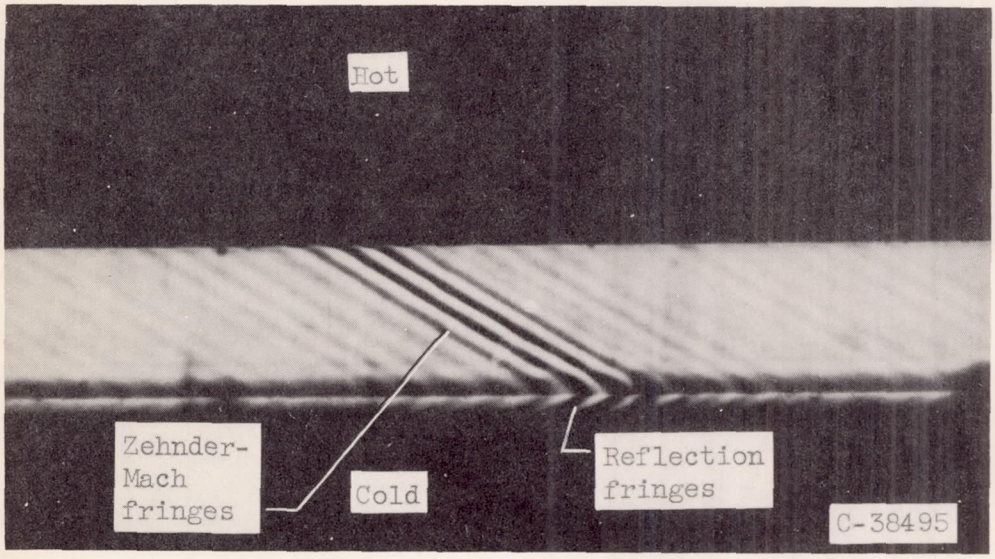

Figure 22. - Interferogram of hot-plate model described in reference 1; K=1.